XFEL.EU TR-2013-005

TECHNICAL DESIGN REPORT

Scientific Instrument Materials Imaging and Dynamics (MID)

October 2013

A. Madsen, J. Hallmann, T. Roth,
and G. Ansaldi
for the Scientific Instrument MID
(WP83) at European XFEL

European X-Ray Free-Electron Laser Facility GmbH
Albert-Einstein-Ring 19
22761 Hamburg
Germany

Contents

1 Introduction 7

2 Science case and technical ramifications 9

2.1 Self-seeded operation 10
2.2 Imaging, coherence, and correlations 11
2.3 Pump–probe science 12
2.4 High-energy option 13

3 General layout 15

3.1 Common SASE2 photon tunnel 17
  3.1.1 X-ray gas monitor detector and beam position monitor 17
  3.1.2 Attenuator 20
  3.1.3 Primary lens stack (CRL-1) 22
  3.1.4 Imager 25
  3.1.5 Beam shutter 26
  3.1.6 Offset mirrors 26
  3.1.7 High-energy Laue monochromator 30
3.2 MID beamline 32
  3.2.1 Slits 32
  3.2.2 Monochromator-1—Si(111) 33
  3.2.3 Secondary lens stack (CRL-2) 38
3.3 Optics hutch 41
  3.3.1 Monochromator-2—Si(220) 42
  3.3.2 Attenuator-3 44
  3.3.3 Split and delay line 45
3.4 Experiment hutch 45
  3.4.1 Mirrors 47
  3.4.2 Differential pumping section 50
  3.4.3 Experiment chamber 52
  3.4.4 Diagnostics end station 53
3.5 Other premises 56
  3.5.1 Control room 56
  3.5.2 Rack room 57
  3.5.3 Optical laser hutches 57
  3.5.4 Assembly and sample preparation room 57

4 Thermal impact and damage ... 59
4.1 Adiabatic heating ... 59
4.2 Thermal conductivity ... 61
4.3 Single-shot ablation ... 62
4.4 Thermal model for Be lenses ... 64
4.5 Thermal model for B_4C ... 69
4.6 Tungsten slit blades ... 71

5 Beryllium lenses ... 73
5.1 Beam size and divergence ... 73
5.2 Lens formula ... 73
5.3 Focusing and collimation schemes ... 74
5.4 Beam sizes at the sample ... 77
5.4.1 Absorption and effective aperture ... 78
5.5 CRL-1 transfocator at 235 m ... 80
5.5.1 Weak lenses ... 80
5.5.2 Total focusing power ... 81
5.5.3 Transmission ... 82
5.5.4 Proposed configuration of CRL-1 ... 83
5.6 CRL-2 transfocator at 931 m ... 85
5.7 Total transmission of the two CRL stacks ... 88
5.8 Stability considerations ... 89
5.9 Beryllium as an optical element ... 90

6 Split and delay line ... 91
6.1 Placement ... 91
6.2 Bragg reflections and beam divergence ... 92
6.3 Stability considerations ... 93
6.4 Geometry ... 95
6.5 Energy acceptance ... 98
6.6 Beam splitter ... 99
6.7 Preliminary design ... 103

7 Experiment hutch ... 107
7.1 Experiment chamber ... 107
7.1.1 Sliding mechanism ... 111
7.2 Scattering geometries ... 112
7.2.1 Horizontal arm—SAXS and WAXS configuration ... 113
7.2.2 Vertical arm ... 118

7.3 Sample environment ... 120
    7.3.1 Goniometer ... 120
    7.3.2 Liquid-jet systems ... 121
    7.3.3 Liquids at high temperatures ... 123
    7.3.4 Cryostat for pulsed magnetic fields ... 125
    7.3.5 Liquid surface/interface sample cell ... 126
    7.3.6 SAXS chamber ... 126
    7.3.7 Furnace for Bragg reflection studies ... 127
    7.3.8 Millifluidic and microfluidic sample delivery ... 128
    7.3.9 Free-standing sample environments ... 128
7.4 Nanofocusing ... 130

8 Ancillary instrumentation and software ... 133
8.1 Detectors ... 133
    8.1.1 Adaptive Gain Integrating Pixel Detector (AGIPD) ... 133
    8.1.2 LBNL CCD—small pixel size X-ray camera ... 136
    8.1.3 Gotthard 1D detector ... 140
8.2 Optical lasers ... 141
    8.2.1 Pump laser system ... 141
    8.2.2 Temporal overlap of optical laser and XFEL beam ... 145
8.3 DAQ system ... 146
    8.3.1 Timing system ... 146
    8.3.2 Karabo software tool ... 147
8.4 Infrastructure ... 151

9 Timeline and risks ... 153
9.1 Planning risks ... 153
9.2 Technological risks ... 154
9.3 Schedule ... 155

10 Acknowledgments ... 157

A Beam sizes ... 159
A.1 Beam size and divergence ... 159
A.2 Intermediate focusing scheme ... 160
A.3 Collimating then focusing scheme ... 161
A.4 Focusing with CRL-1 ... 163
A.5 Focusing the naturally divergent beam only with CRL-2 ... 165

B Split and delay line calculations 167
B.1 Atomic scattering factors 167
B.2 Crystal structure factor 170
B.3 Linear absorption coefficient 170
B.4 Absorption, extinction, and reflectivity 171

C Beryllium 173
C.1 SAXS measurements of Be grades 173
C.2 Wavefront propagation through Be CRLs 175
C.2.1 Impact of Be imperfections 176
C.2.2 Dispersion effects 179

D Bibliography 181

1 Introduction

This technical design report (TDR) for the Materials Imaging and Dynamics (MID) scientific instrument at the European XFEL [28; 3] is based on the previous conceptual design report (CDR) [75].

The scope of the TDR is to present the current status of the technical design of the MID instrument. The report includes a description of the tunnel installations and the environment in the experiment hall, an outline of the MID X-ray hutches and optical laser installations, and the design of the beam transport system and X-ray optics, as well as specifications for the required instrumentation, detectors, X-ray diagnostics, and data acquisition systems.

Our goal is to provide the user community from 2016 onwards with X-ray laser beams of unprecedented intensity and coherence in a scientific instrument optimized for materials science experiments.

Due to the complex nature of the work, the picture presented in this TDR is necessarily incomplete and subject to changes. Nevertheless, the document indicates where we are heading by clearly defining functions and giving technical specifications of all components.

2 Science case and technical ramifications

The science case of the MID instrument has remained largely unchanged since the 2012 CDR [75], in which the issue is thoroughly discussed. Time-resolved scattering and diffractions studies in materials science will be available at MID, particularly a pump–probe mode where the pump can be either X-rays or an optical laser beam. Special emphasis will be on experiments utilizing the coherence properties, the time structure of the beam, or both.

The MID instrument will seek to exploit the full potential of the European XFEL facility and provide its users with the highest peak and average flux in a range from 5 to 25 keV, possibly even higher if the harmonic lasing scheme that was recently proposed proves feasible [105]. The goal is also to host synchrotron radiation–derived techniques like X-ray photon correlation spectroscopy (XPCS) and coherent X-ray diffraction imaging (CXDI). Investigations are in progress to determine how these types of experiments can best be realized in their free-electron laser (FEL) derivatives. Issues related to the stability and repeatability of FELs have been challenging in transferring well-known experimental schemes to these new sources and thereby taking full advantage of the huge gain in brilliance.

A recent development is second-generation X-ray FELs (XFELs) based on seeded lasing, which minimizes the randomness of the self-amplified spontaneous emission (SASE) process. The self-seeding scheme [32; 4] is particularly interesting, and it is expected that the European XFEL will feature self-seeding from the beginning of its operation. This will ensure that challenging experiments can operate under stable conditions (e.g. in terms of coherence, jitter, and energy spectrum) in an optimized fashion. Self-seeding is also expected to maximize the throughput of the X-ray split and delay line that will be operated at the MID instrument.

Area detectors with small pixels and single-photon sensitivity running at MHz speed are required to take full advantage of the beam parameters in scattering experiments. Building such detectors is indeed an endeavour, and even if the Adaptive Gain Integrating Pixel Detector (AGIPD) system under development for the European XFEL fulfils the main requirements, the 200 µm pixel size will put severe limitations on the capability to record speckle patterns with sufficient spatial resolution. As a backup solution, a small-pixel charge-coupled device (CCD) will also be available at the MID instrument from day one. It will not have burst mode performances like AGIPD, but the pixel area will be about a factor of 40 smaller, hence allowing adequate spatial resolution in coherent scattering experiments.

2.1 Self-seeded operation

Unlike other X-ray sources, owing to the laser characteristics of the XFEL light, the coherence properties of hard X-rays at the European XFEL will be very good. The XFEL beam will be diffraction-limited in the vertical and horizontal directions, meaning that, at any location, the beam size will be smaller than the transverse coherence length. In practice, a few modes will contribute to the XFEL intensity, but the mutual degree of coherence will be very high, as demonstrated at the Linac Coherent Light Source (LCLS) at SLAC National Accelerator Laboratory in Menlo Park, California, in single-shot interference experiments [130] and in small-angle scattering speckle analysis [43; 53] for soft and hard X-rays, respectively.

In the longitudinal direction (temporal coherence), the situation is completely different. One XFEL pulse contains many modes of different strengths, and this pattern changes from shot to shot due to the intrinsic noise in the SASE process. The typical full width at half maximum (FWHM) of the SASE envelope is 0.1% ($\Delta E/E$) with the width of individual modes being at least an order of magnitude smaller [139]. The average individual mode pattern depends strongly on machine parameters, like pulse charge and pulse duration [54], but the fine structure of the spectrum is completely random from shot to shot.

This intrinsic randomness is a problem for experiments where the longitudinal coherence properties play a role, for instance in coherent diffraction at large momentum transfer where the contrast will fluctuate strongly from shot to shot. Any phase-sensitive scattering experiment on a sample of non-vanishing thickness will be affected by these coherence fluctuations. Ultimately, these fluctuations will limit the achievable resolution in phase retrieval and reconstruction experiments. Reflecting the beam from a single-crystal monochromator only improves the situation if its bandwidth is very narrow, and this has the unwanted side effect of decreasing the signal and amplifying the SASE intensity fluctuations [68].

Self-seeding by a wake monochromator—as suggested by Geloni, Kocharyan, and Saldin [32]—has the potential of more or less eliminating the spectral SASE noise, even if some intensity fluctuations will still remain. The shot-to-shot fluctuations in longitudinal coherence properties can be reduced to an insignificant level, and the bandwidth of the seeded spectrum will be inversely proportional to the pulse duration (Fourier limit). For many experiments, operation with a monochromator is still required, for instance to suppress harmonic content and the spontaneous background. With a seeded XFEL, monochromator operation is possible without introducing additional intensity fluctuations.

LCLS has demonstrated seeding with $\Delta E/E = 5 \times 10^{-5}$, corresponding to a pulse duration of less than 10 fs [4; 139]. Likewise, at the SPring-8 Angstrom Compact Free Electron Laser (SACLA) in Hyogo, Japan, single-shot energy spectra and simulations indicate that a pulse duration of 30 fs gives rise to distinct spikes in the SASE spectrum of $\Delta E/E = 1 \times 10^{-5}$, which is close to the Fourier limit given by the pulse length [54]. At the MID instrument, it is foreseen to employ Si(220) monochromator crystals with a bandwidth of $\Delta E/E \simeq 6.0 \times 10^{-5}$, as this provides a good match to the seeded pulse width down to about 5–10 fs pulse duration. A Si(111) monochromator ($\Delta E/E \simeq 1.4 \times 10^{-4}$) will also be available at MID in order not to clip the intensity of seeded pulses shorter than ~ 5 fs.

2.2 Imaging, coherence, and correlations

Coherent diffraction with a stable one-mode (seeded) X-ray laser offers very interesting perspectives, particularly for experiments requiring repetitive exposures under stable conditions. This type of experiment includes sequential XPCS [39], time-resolved XPCS [76], 3D CXDI [86], and ptychography [123]. The experiments can be performed under "synchrotron-like" conditions in terms of stability and repeatability and can be "laser-like" when it comes to coherence and pulse duration. This versatility will allow us to transfer these techniques into the XFEL domain and take full advantage of the boost in coherent flux with respect to third-generation storage ring–based X-ray sources. Beam damage will provide the ultimate limit for such experiments, but there is still a large window of opportunity compared to today's most powerful X-ray sources.

Stable operation of an X-ray split and delay line (SDL) [99] will be facilitated by seeding the XFEL. Then the science enabled by the SDL can really develop, e.g. X-ray pump–X-ray probe, two-colour and stereo imaging experiments [50], ultrafast X-ray tomography [104], and speckle visibility spectroscopy on summed images [40]. The two beams from the SDL can also be brought to interfere in advanced schemes, for instance in X-ray quantum optics experiments or in temporally and spatially resolved X-ray holography [35].

Novel higher-order spatial correlation schemes are being developed to explore the local structure and symmetry of condensed matter. The short duration of the XFEL pulse implies that practically any structural dynamics appear arrested in the scattering images. Hence, this property makes the XFEL source ideal for structural X-ray studies without any positional averaging in the scattering images, even for fast and ultrafast atomic and molecular dynamics. Whereas access to structural information by higher-order spatial correlations has been demonstrated in dilute [57; 66] or colloidal systems [133], it proves much harder in the case of dense systems with many local clusters of random orientation, e.g. atomic and molecular liquids and glasses. Theoretical analysis and simulations on two-dimensional (2D) systems indicate that, typically, at least 10^4 images are required to achieve a significant signal-to-noise ratio [65], for instance to reveal the local symmetries that exist as a consequence of preferred bond orientations or due to free-energy minimization on the local scale. Generalization to three-dimensional (3D) systems is challenging, but it is clear that many images will be needed. This leads to high demands on the rate at which pulses need to interact with the sample and the speed at which scattering images can be recorded. Typically, such experiments will be of the single-shot type and samples have to be renewed, for instance by operating an injector or a microfluidic system, or by using a rapidly movable array of solid-sample targets.

2.3 Pump–probe science

Many interesting materials science experiments will belong to the “pump–probe” category, where a system is excited or heated by a pump pulse, after which the system is probed by X-ray scattering to observe the evolution at various lag times. Prominent examples of research include e.g. studies of ultrafast demagnetization [12], non-thermal melting [100], and bond softening in solids [31]. Typical timescales for electronic motion (spin, magnetism, excitations) are in the femtosecond to picosecond range, while structural dynamics occur in the picosecond to microsecond range and slower.

The coupling between electron and phonon dynamics is a matter of great interest and has been studied with femtosecond X-ray diffraction, e.g. in ferroelectrics [63], to obtain the electron density directly. Ultrafast electron transfer driven by a non-resonant optical pulse in ionic materials has been studied by X-ray powder diffraction [116; 137]. Also, non-destructive, reversible atomic displacements on the picosecond timescale due to coherent phonon excitations have been studied in semiconductors using X-ray diffraction [7].

The optical pump at MID will be provided by a tunable (UV–IR) optical laser system with the capability of burst mode operation at 4.5 MHz, i.e. similar to the repetition rate of the European XFEL within a train. Obviously, combinations of the ultrafast pump–probe scheme with coherent scattering (speckle) and with the X-ray split and delay line provide interesting new possibilities. For instance, the sample system can be probed by X-rays before and after the optical pump, which would be interesting in imaging, speckle, and correlation-type experiments. Alternatively, both X-ray pulses could arrive after the optical pump to monitor the dynamics. Because of the coherent illumination and the speckle patterns, both schemes give access to statistical information beyond the averaged quantities that are obtained in regular pump–probe studies.

2.4 High-energy option

The electron energy of the European XFEL can be as high as 17.5 GeV. This allows saturated lasing with the 175 m long SASE2 undulator (magnetic length: 35 segments of 5 m magnetic length each) up to 25 keV on the fundamental harmonic. Higher-order harmonics are also generated on-axis ($n = 3, 5, ...$), but they are less intense (in total power) by at least two orders of magnitude for every jump in order, and the width ($\Delta E/E$) of the peak does not scale like $1/n$ but remains at about 0.1%, like the fundamental.

Recently, an operation mode referred to as “harmonic lasing” was proposed by Schneidmiller and Yurkov [105]. By tuning the phase shifters between undulator segments and using photon beam absorbers in the undulator (enabled by the chicanes to be installed for self-seeding purposes), it is possible to disrupt lasing on the fundamental. Instead, the power is redirected to the third or fifth harmonics and saturation (lasing) occurs. It is believed that photon energies up to 100 keV can be achieved in the harmonic lasing scheme with more than 10^9 photons/pulse.

This development will provide entirely new possibilities for high-energy scattering and imaging experiments. For instance, experiments requiring penetration power, e.g. to investigate the local structure of monoatomic liquids at interfaces or in bulk, could be combined with the unique possibilities of XFEL radiation, where the short pulse duration allows freezing-in of structures on all length scales in diffraction images. A high photon energy gives access to large momentum transfers in a single shot on a 2D detector and provides novel possibilities for imaging of nanostructures [42].

The possibility of developing suitable 2D detectors with increased high-energy sensitivity is currently being investigated at European XFEL and elsewhere. Here, we only note that a major change is required in the detector head, where the X-ray sensor material must be changed from silicon to a high-Z material while maintaining the possibilities of ASIC integration and pixelated readout.

Harmonic lasing is also useful to increase the spectral brightness at lower photon energies. The FWHM of the harmonic lasing spectrum scales like $1/n$, meaning that $\Delta E/E = 2 \times 10^{-4}$ can potentially be reached on the fifth harmonic at 15 keV (first harmonic at 3 keV) without the use of a monochromator. This width is almost equivalent to the Darwin width of a Si(111) Bragg reflection and provides a major step forward, as all the photons are delivered in a narrow bandwidth without the complications of using a monochromator.

A 25 mm horizontal offset of the beam away from the optical axis of the undulator is required for radiation protection purposes (bremsstrahlung). X-ray mirrors allow the required offset to be achieved up to about 60 keV if metal coatings can be applied [109]. A limiting factor of metal coatings is the absorption, which can potentially lead to radiation damage both on the single-shot level and over extended periods of time. It is believed that working below the damage threshold will be possible in most cases for unfocused beams impinging below the critical angle, particularly if the mirrors are protected by a boron carbide (B_4C) coating of several tens of nm thickness. If it turns out that metal mirrors cannot withstand the beam or if energies beyond 60 keV are required, a Laue monochromator could be operated instead of the mirrors and provide the required horizontal offset.

3 General layout

The overall layout of the European XFEL facility has remained almost unchanged since the MID CDR [75] was written in autumn 2011. Also, the descriptions of accelerator and undulator performances in Refs. [75; 109] remain largely valid. Here, we concentrate on new possibilities that have emerged and on the updated component specifications relevant to MID. A general overview of the devices introduced in this chapter can be found in Figure 3.1. The main characteristics of the MID instruments are summarized in Table 3.1 on the next page.

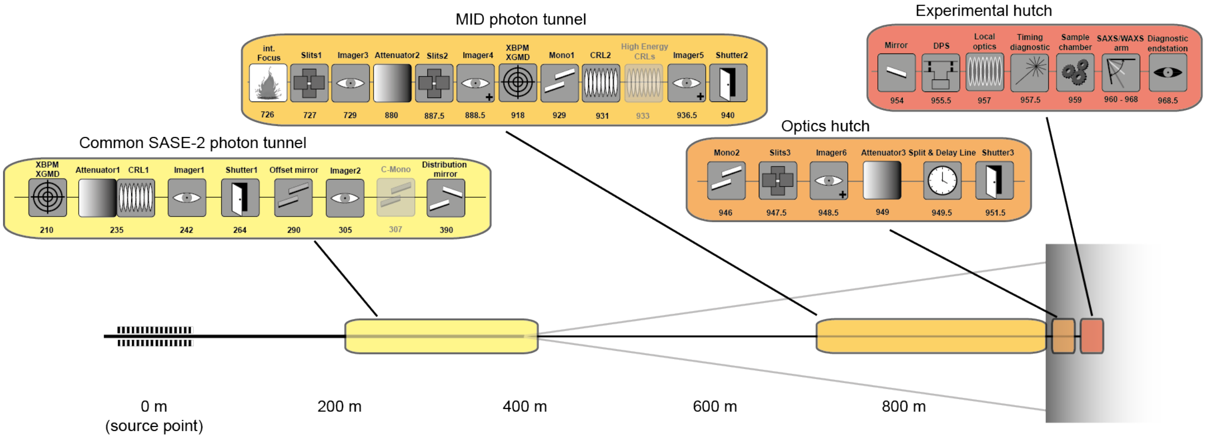

Figure 3.1: Schematic top view on the SASE2 photon tunnels and the MID hutches. Devices relevant for the MID instrument are shown as pictograms. The MID instrument is located at the central beam pipe. The distance to the side branches is about 1.4 m at the end of the tunnel. Four different areas are of particular interest: the common SASE2 tunnel, the MID tunnel, and the optics and experiment hutches of the MID instrument. The distances along the z-axis from the source point to the various devices are indicated. (*Key:* XGMD = X-ray gas monitor detector, XBPM = X-ray beam position monitor, Mono = monochromator, CRL = compound refractive lenses, DPS = differential pumping section, SAXS = small-angle X-ray scattering, WAXS = wide-angle X-ray scattering.)

Most of the beamline components are designed to work in an energy range from ~ 5 to ~ 25 keV. Only the split and delay line operates in a more narrow energy range between 5 and 10 keV. The vacuum requirement for the beam transfer system of the tunnels and the MID optics hutch is about 10^{-9} mbar (ultrahigh vacuum, UHV). At the entrance of the experiment hutch, a differential pumping section (DPS) allows operation of the experiment chamber and successive components up to ~ 10^{-1} mbar. The DPS takes quite some space but is mandatory in order to avoid windows in the beam path. Following European XFEL convention, the beam direction is along the *z*-axis. The photon source point is defined as the middle of the third last undulator segment ($z = 0$). All distances given in the following chapters refer to this location. Perpendicular to the beam, following a right-hand Cartesian coordinate system, the *x*-axis and the *y*-axis are in the horizontal and vertical (positive up) directions, respectively. Due to the geographical orientation of the facility, the *z*- and *x*-axes correspond approximately to the west and south directions, respectively.

Table 3.1: Summary of the MID instrument characteristics

Photon energy range	5–25 keV (coherent) and > 25 keV (high-energy option)
Bunch charge	1–1000 pC
Polarization	Linear (horizontal)
Pulse duration	1–100 fs
Beam size on the sample	1–200 µm, 1 mm, and nanofocus option
Beamline optics	2 monochromators (Si(111) and Si(220)) 2 compound refractive lens (CRL) transfocator units Split and delay line High-energy Laue monochromator (optional)
Equipment	Multipurpose chamber, SAXS/WAXS geometries with long horizontal detector arm, small vertical WAXS setup, single-pulse X-ray diagnostics, different detector systems (AGIPD, FastCCD), optical pump laser source

3.1 Common SASE2 photon tunnel

The area between the electron beam dump and the distribution mirror is called the common SASE2 photon tunnel. This part of the beam path is common to the MID and High Energy Density Physics (HED) instruments, as well as possibly a third instrument (NNN) to be realized later, meaning that components can be shared. Figure 3.2 shows a schematic view of the components in this area with their particular positions.

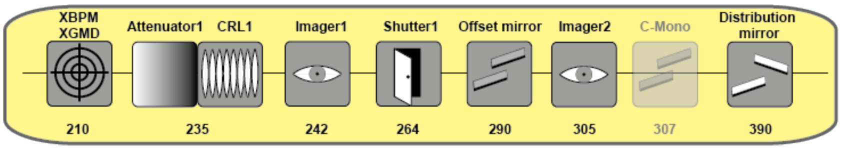

Figure 3.2: Main components in the common photon tunnel of SASE2 with their distances to the source point. The entire set of components is available for all instruments at SASE2. The distribution mirror at the end of this section is not used by MID but is shown for completeness.

3.1.1 X-ray gas monitor detector (XGMD) and beam position monitor (XBPM)

Knowledge about the intensity of the individual XFEL pulses is of general interest during an experiment and often absolutely necessary for quantitative data analysis. Therefore, it is crucial to equip the beamlines with a non-invasive (transparent) diagnostic tool that can capture this information for every X-ray pulse. The requirements of the MID instrument for the intensity acquisition at this point are listed in Table 3.2.

Table 3.2: Performance specifications for an XGMD at the MID beamline

Intensity (photons per pulse)	10^8–10^{12}
Beam sizes	100–4000 µm
Clear aperture	25 mm
Photon energy	5–25 keV

To this end, it was decided to develop X-ray gas monitor detectors (XGMDs) for all beamlines at the European XFEL. In the XGMDs, noble-gas atoms are ionized by incoming X-rays and provide an electrical signal via electrodes or electron multipliers. In this manner, it is possible to obtain an absolutely calibrated intensity value of every pulse at the full repetition rate (4.5 MHz). The choice of gas depends on the photon energy used, and gases ranging from neon at low energy to xenon at higher energies (up to 25 keV) may be employed. As an example, a device based on xenon could provide an intensity measurement with a relative uncertainty of ~ 2% for 10^{10} XFEL photons per pulse at 25 keV [124]. The uncertainty is determined by the statistical nature of the photoionization process and increases for lower intensities. If the intensity is lower by two orders of magnitude, the uncertainty increases to ~ 20%. Operation with lower photon energies is less critical due to the higher photoionization cross section. An overview of the uncertainty dependence on photon energies at gas pressures of 10^{-4} mbar can be found in Figure 3.3 on the facing page. In addition to the intensity determination by the XGMDs, it is also possible to extract spatial information about the beam. At this location, for the MID instrument, it is sufficient to record the beam position at a 10 Hz rate, i.e. averaged over a pulse train, and with an accuracy of 10 µm.

The XGMDs are being conceived in a cooperation between European XFEL and K. Tiedtke's group at Deutsches Elektronen-Synchrotron (DESY). They will be constructed and delivered by DESY, and two of these devices will be used at the MID instrument—one positioned at the beginning of the common tunnel at 210 m and one towards the end of the MID tunnel at 918 m. As the XGMDs operate with a gas pressure of about 10^{-4} mbar, differential pumping systems have to be set up on the entrance and exit side of the devices. Further information about these intensity and position monitors can be found in Ref. [125]. Recent tests of the XGMDs at SACLA proved the performance of the system up to ~ 17 keV and allowed calibration of other types of beam monitors [60].

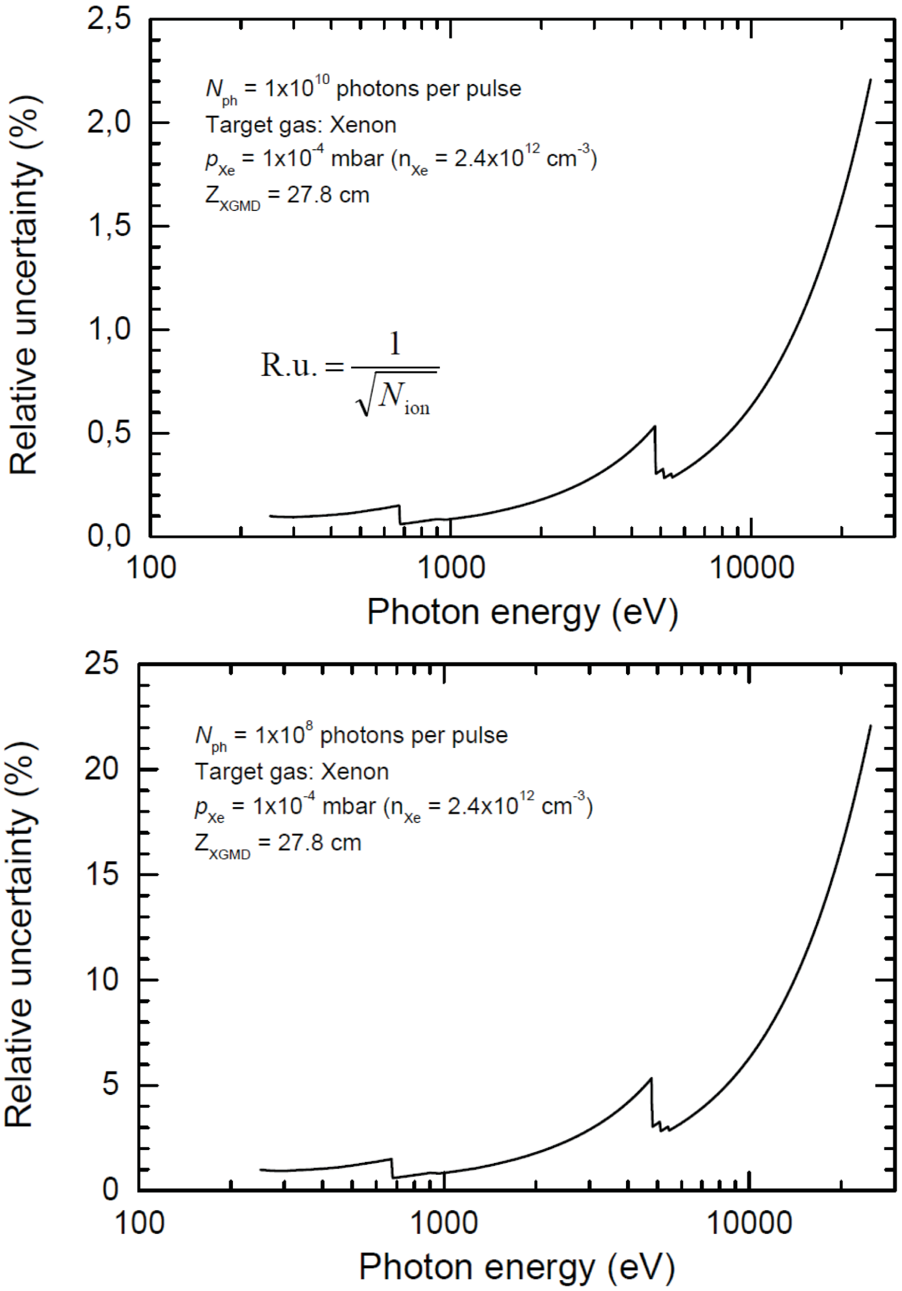

Figure 3.3: Relative uncertainty of the XGMDs planned for the European XFEL. The calculation assumes 10^{-4} mbar partial pressure of xenon and were made by K. Tiedtke (DESY) [124]. The top panel shows the case $N_{\mathrm{ph}} = 10^{10}$ photons per pulse, the bottom $N_{\mathrm{ph}} = 10^{8}$.

3.1.2 Attenuator

Solid-state attenuators are sometimes required to reduce the intensity of the XFEL beam. The motivation can be to lower the risk of damaging the beamline optics or the sample, or avoiding over-exposures of the detector. Especially for initial beam alignment or during experiments where multiple exposures are required, special precautions must be taken. Taking the SASE intensity fluctuations into account, we estimate that an attenuation of the intensity by up to seven orders of magnitude is needed.

A solid-state attenuator is planned as one of the first components in the tunnel, located about 235 m after the source point. Since the device will be used during user operation, it is designed to withstand powerful beams, e.g. 1350 pulses at a bunch charge of 250 pC at 17.5 GeV. As attenuator materials, we consider boron carbide (B_4C), silicon, and diamond to be the best choices. The attenuation factors of B_4C and diamond are of the same order of magnitude. Both have high single-shot ablation thresholds and good heat transport and thermal properties. Diamond is expected to disturb the wavefront of the transmitted beam less than B_4C, as the material quality is better. The best diamond quality (Type IIa, high-pressure high-temperature (HPHT) diamond) is available only in limited sizes and thicknesses, but it may be possible that a lower quality can be tolerated at this position far from the sample. B_4C does not exist as large single crystals but is a sintered material. On the other hand, B_4C is rather cheap and well known for its high hardness and stability during interaction with intense radiation.

Silicon is necessary to attenuate beams of higher energy (above ~12 keV) where diamond and B_4C are rather ineffective. Silicon is inexpensive, and large, perfect single-crystalline pieces are readily available. The proposed collection consists of five B_4C absorbers (with thicknesses of 0.5 mm, 1 mm, 2 mm, 4 mm, and 8 mm) and five diamond absorbers (0.1 mm, 0.2 mm, 0.4 mm, 0.8 mm, and 1.6 mm). This combination allows us to change the attenuation factor in fine steps in the range from 5 to 12 keV. Five Si absorbers are also required and will have thicknesses of 0.5 mm, 1 mm, 2 mm, 4 mm, and 8 mm. Using the full attenuation of one device (15 foils), the transmission at 25 keV will be 10^{-4} (see Table 3.3 on the next page).

Table 3.3: Transmission factors for diamond, B_4C, and silicon at different thicknesses and photon energies. The calculations are based on [122]. Values below 10^{-13} were set to zero.

Thickness [µm]	5 keV	8 keV	12 keV	16 keV	25 keV
Diamond					
100	0.51	0.86	0.96	0.98	0.99
200	0.26	0.74	0.91	0.96	0.98
400	0.07	0.54	0.84	0.92	0.96
800	0.005	0.29	0.70	0.85	0.93
1600	2.27×10^{-5}	0.09	0.49	0.72	0.86
Sum = 3100	1.00×10^{-9}	0.009	0.25	0.53	0.75
B_4C					
500	0.24	0.72	0.90	0.95	0.97
1000	0.06	0.52	0.82	0.90	0.95
2000	0.003	0.27	0.67	0.82	0.90
4000	1.11×10^{-5}	0.07	0.45	0.67	0.81
8000	1.24×10^{-10}	0.005	0.20	0.45	0.65
Sum = 15 500	0	3.84×10^{-5}	0.04	0.21	0.44
Silicon					
500	8.78×10^{-13}	7.94×10^{-4}	0.11	0.39	0.78
1000	0	6.31×10^{-7}	0.01	0.16	0.61
2000	0	3.98×10^{-13}	1.56×10^{-4}	0.02	0.37
4000	0	0	2.42×10^{-8}	5.87×10^{-4}	0.13
8000	0	0	0	3.44×10^{-7}	0.02
Sum = 15 500	0	0	0	3.00×10^{-13}	4.17×10^{-4}
All in	0	0	0	0	1.38×10^{-4}

Several attenuator designs have been developed at synchrotron sources over the years. At the European XFEL, however, the foils need to be cooled, something that was not standard in the past developments. JJ X-Ray [77], Denmark, has developed a design in which the attenuator targets are mounted on 15 independent, water-cooled arms moved by stepper motors (Figure 3.4). In this way, suitable attenuation factors can be achieved over the full energy range (cf. the discussion above). A second attenuator is required further downstream of the beamline at 880 m. Combining the full attenuation of both devices, the XFEL beam intensity can be reduced by eight orders of magnitude. The attenuator devices must be compatible with standard beamline vacuum, i.e. 10^{-8}–10^{-9} mbar, and an ion pump is needed close to the solid-state attenuator. Absolute encoders are required on all movable parts, and, for safety reasons, a temperature measurement close to the impact point is needed. Great care must be taken for all movable devices in the beamlines to ensure that frames, actuators, and other parts that cannot withstand exposure to the beam are well protected during operation. Extensive use of protective B_4C apertures is foreseen in front of all devices.

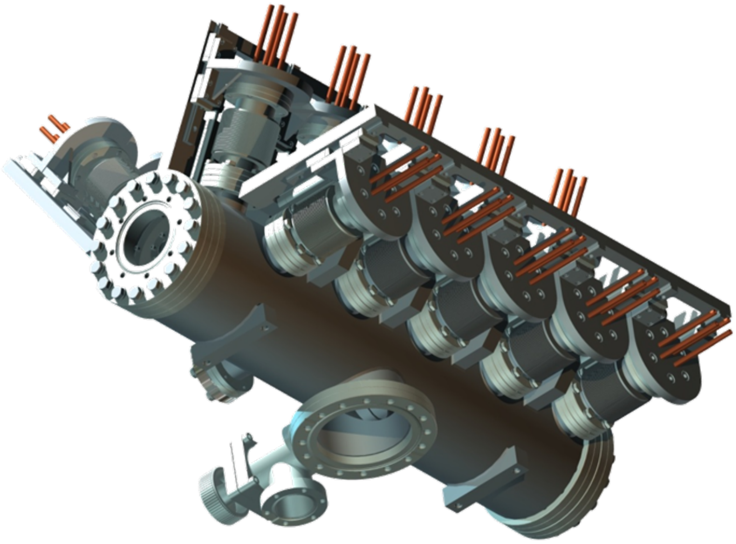

Figure 3.4: Solid-attenuator assembly designed by JJ X-Ray [77]. The 15 individual absorbers are water-cooled and can be moved into the beam with stepper motors. The length of the device is about 620 mm.

3.1.3 Primary lens stack (CRL-1)

According to XFEL simulations, the SASE beam will have a natural divergence of only about 1–5 µrad, depending on photon energy and electron beam parameters [109]. However, due to the long source–sample distance of ~ 960 m, the XFEL beam must be collimated or refocused to match the acceptance of the beamline optics. On the other hand, the photon density cannot increase so much that the damage threshold of optical elements is approached.

A focusing scheme based on beryllium compound refractive lenses (CRLs) is the best choice for the MID instrument. Using eight different lens stacks at $z = 235$ m will be sufficient to collimate the beam over the energy range from 5 to 25 keV. Furthermore, this setup is capable of generating an intermediate focus at 726 m after the source point for energies in the above-mentioned range. The focal size w_0 of a diffraction-limited beam is given by Abbe's formula

$$w_0 = \lambda/(2 \cdot \sin\alpha) \tag{3.1}$$

λ is the wavelength and α the angle between the optical axis and the outer part (FWHM) of the outgoing radiation cone converging towards the focus. The beam size w away from the focus follows the propagation formula

$$w = w_0 \cdot \sqrt{1 + \left(\frac{4z\lambda}{w_0^2}\right)^2} \tag{3.2}$$

with z being the distance to the focus. The results of the focal sizes in the *intermediate focusing* scheme can be found in Figure 3.5 on the next page for different XFEL energies. The beam diameter on the optical components in the beamline is given in Table A.1 on page 160. This focusing scheme leads to the smallest beam sizes in the photon tunnel, but the FWHM never decreases below ~ 100 µm.

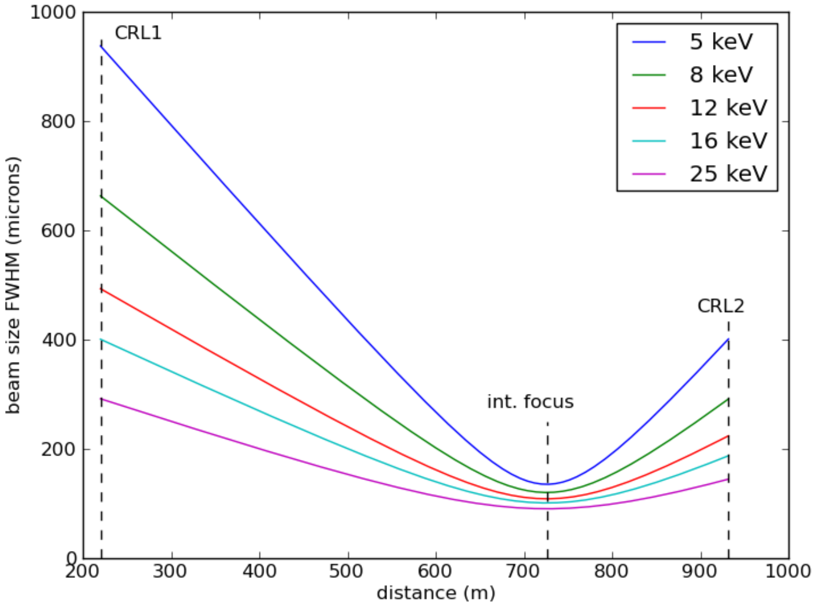

Figure 3.5: Evolution of the beam size after the primary lens stack in the *intermediate focusing* geometry. The graph presents the diameter (FWHM) of the XFEL beam at 5 keV (blue), 8 keV (green), 12 keV (red), 16 keV (cyan), and 25 keV (purple). The dashed lines indicate the positions of the CRL-1 stack, the intermediate focus, and the CRL-2 stack. The calculations are based on Equation 3.1 on the previous page and Equation 3.2 on the preceding page. The minimum beam size in the photon tunnel is about 100 µm.

Setups for moving the CRLs into the beam in various configurations have been developed at synchrotron and FEL sources. A setup designed for Beamline ID10A at the European Synchrotron Radiation Facility (ESRF) in Grenoble, France, operating with water-cooled lenses was licensed to JJ X-Ray, which further developed the concept. LCLS developed their own CRL system, and, in a first proposal for European XFEL [77], six different lens stacks can be moved independently in and out of the beam in a transfocator design by JJ X-Ray. The exact lens combination required depends on the photon energy and the requested focusing geometry. This transfocator can easily be modified into the eight-stack system required by MID (Figure 3.6 on the next page). The device operates under UHV conditions. The arms are individually movable by stepper motors and equipped with absolute encoders. The requirement for positioning precision is 1 µm. A temperature measurement must be performed close to every lens for safety reasons, and proper shielding of the frames and actuators is required. The thermal properties of the Be lenses and their behaviour in the beam are discussed in Section 4.4, “Thermal model for Be lenses”.

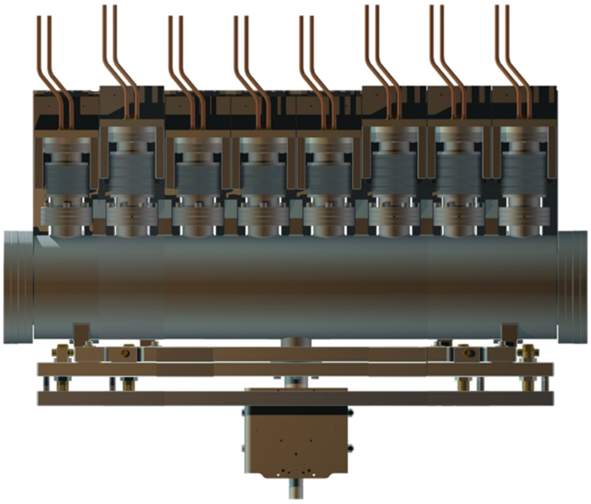

Figure 3.6: Sketch of a Be lens focusing device (transfocator), based on a drawing by JJ X-Ray [77]. The MID instrument requires eight different lenses for proper focusing.

The first lens system (CRL-1) can be operated together with a second device (CRL-2) that is located 931 m after the source point, right before the experiment hall. In this way, different focusing geometries are possible. Detailed information about the Be lenses and the focusing schemes is presented in Chapter 5, “Beryllium lenses”.

3.1.4 Imager

Early in the beam alignment procedure, it is necessary to know the exact position of the beam as well as its shape. Imaging tools at different locations are therefore required to provide images of the beam profile in 2D. The imagers have to be flexible (in/out on request) and large enough to detect possible beam offsets after optical elements like monochromators or offset mirrors. Simple retractable imagers, known as pop-in monitors, will be the most suitable devices. These monitors can surround all optical elements in the beamline, allowing exact alignment of the beam. An optical camera will record the image of the beam on a scintillator material. Yttrium aluminium garnet (YAG) screens as well as doped chemical vapour deposition (CVD) diamond can be utilized, since these materials yield a response that is linearly proportional to the beam intensity, also for high-energy photons. Normally, a pop-in monitor is invasive; hence, it cannot be used during data taking and will probably only withstand the single-bunch operation mode (10 Hz) of the European XFEL. Nevertheless, pop-in monitors will be most useful for initial alignment. Suitable devices are being developed by the X-Ray Photon Diagnostics group at European XFEL. One option under consideration is based on thin diamond screens, which could be compatible with higher repetition rates and could provide a transparent beam position monitor during operation.

3.1.5 Beam shutter

It is mandatory to establish a comprehensive personnel safety system at the European XFEL beamlines. In this context, beam shutters are essential devices, which must be capable of absorbing the beam intensity to keep the downstream part of the beamline absolutely radiation-safe. The planned beam shutters are compatible with up to 1350 pulses/train and 250 pC bunch charge, like the attenuator. We plan to install three beam shutters in the MID beamline: one in the main tunnel at a distance of ~ 264 m from the source point, one at the end of the MID tunnel at ~ 940 m, and one at the exit of the MID optics hutch at ~ 951.5 m.

Shutters at these locations will ensure downstream areas (e.g. the experiment hutch) are accessible while the beam is "on" upstream. The European XFEL X-Ray Optics and Beam Transport group is in charge of developing these devices. The plan is to realize shutter systems by combining a B_4C absorber, a tungsten collimator, and a tungsten shutter. All parts will be separately water-cooled to avoid overheating. Further information about the planned beam shutters can be found in Ref. [110].

3.1.6 Offset mirrors

In addition to the X-ray SASE radiation needed for the experiments, the undulators also emit unwanted high-energy bremsstrahlung. In order to separate the two, an offset mirror system is being developed to deviate the X-rays before a bremsstrahlung beam stop. This offset mirror system consists of two 950 mm long mirrors with an optical useful length of 800 mm [109; 110]. The mirrors reflect the beam sideways, i.e. the beam remains in the horizontal plane. The first mirror is flat, the second one can be bent for horizontal focusing. This feature is important for the HED and NNN branches of SASE2, which require distribution mirrors downstream of the offset mirrors to be able to operate. Focusing by the offset mirror reduces the beam size at the distribution mirror, hence yielding a higher transmission. For the MID instrument, this focusing capability is not required. Instead, MID will employ parabolic CRLs to focus the beam, as these lenses focus simultaneously in the horizontal *and* vertical plane.

In order to transmit as much X-ray intensity as possible, the beam footprint on the mirror surface must be smaller than the length, i.e. the incidence angle cannot be too small. At the same time, the incidence angle must stay below the critical angle of total external reflection of the mirror. The offset mirrors are B_4C-coated Si substrates (with the possibility of a second stripe made from a high-Z material to increase the critical angle). The critical angle for B_4C is $\alpha_c = \sqrt{2\delta_{B_4C}}$, where δ is the correction to the real part of the refractive index ($\delta = 1 - \mathrm{Re}(n)$). The mirror reflectivity is shown in Figure 3.7 as a function of energy.

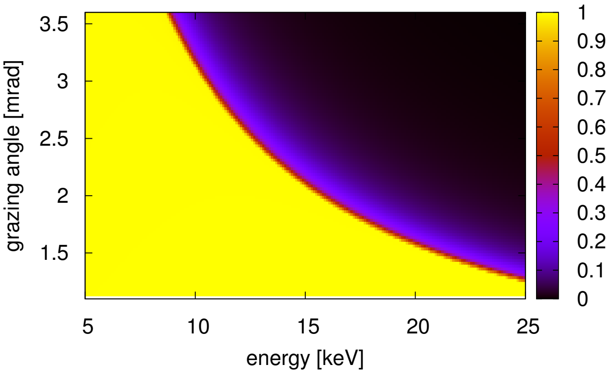

Figure 3.7: Reflectivity of a B_4C-coated Si mirror as a function of angle and energy. For a given energy, the working angle of the mirror will be chosen as large as possible without sliding down the reflectivity curve (dark zone). The critical angle is readily visible as the interface between bright and dark areas. At low energies, the upper limit of the mirror mechanics (3.6 mrad) will be used.

Assuming the incidence angle is the critical angle (but less than 3.6 mrad), the projected size of the high-quality mirror surface (800 mm long) perpendicular to the beam can be calculated and compared to the expected beam size of the X-ray beam. To this end, the maximum divergence of the X-ray beam (20 pC and 17.5 GeV, as found in worst-case simulations [109, page 25]), and a z position of 300 m for the mirror are used. The acceptance of the unfocused beam is compared to a situation where a collimating CRL is used at 235 m after the source, i.e. upstream of the offset mirrors (see Chapter 5, "Beryllium lenses"). The results are shown in Figure 3.8 on the next page. The projected mirror size is almost always above the 6σ limit and even above the 7σ goal in the range from ~ 7 to 15 keV for the unfocused beam. The offset mirrors will always transmit 7σ in the entire energy range if the first CRL stack is used as a collimator.

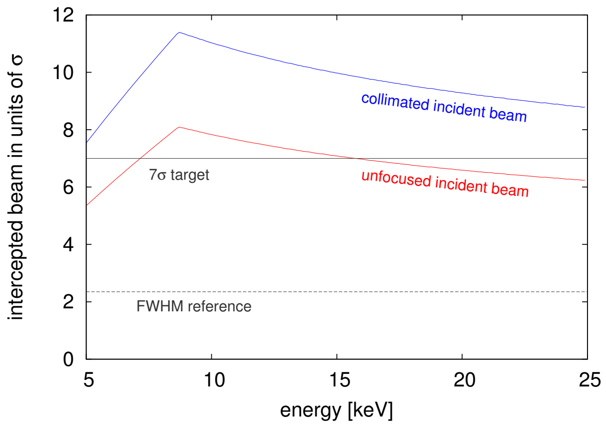

Figure 3.8: Acceptance of the offset mirror as a function of energy for the unfocused and the collimated beam. See Chapter 5, "Beryllium lenses", for the different focusing schemes.

The B_4C coating thickness still remains to be specified. The possible range of thickness is between 30 and 100 nm [108]. The influence of the thickness on the reflectivity close to the critical angle is shown in Figure 3.9. A thickness of 100 nm would be beneficial for protection purposes and in order to keep the reflectivity closer to 1 below the critical angle. This is caused by the reduced X-ray absorption of B_4C compared to Si. There are no additional features emerging in the reflectivity profile since B_4C and Si have approximately the same electron density (0.7 $e^-/Å^3$).

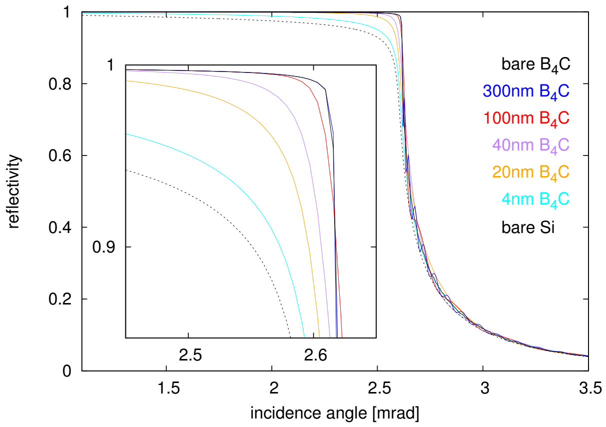

Figure 3.9: Influence of the B_4C coating thickness on the reflectivity at 12 keV

The offset mirror system does not provide a fixed horizontal exit, as none of the mirrors can be translated along the beam direction. The horizontal position at the second mirror is shifted from 25 to 82 mm with respect to the white beam at 25 and 5 keV, respectively. This setup is illustrated in Figure 3.10 on the next page. The horizontal sample position will be maintained at an offset of 25 mm from the white beam, regardless of energy. A small angular adjustment (maximum 0.086 mrad) is needed in this case to guide the beam to the same sample spot for all energies. This adjustment is much smaller than the working angle between 1.1 and 3.6 mrad.

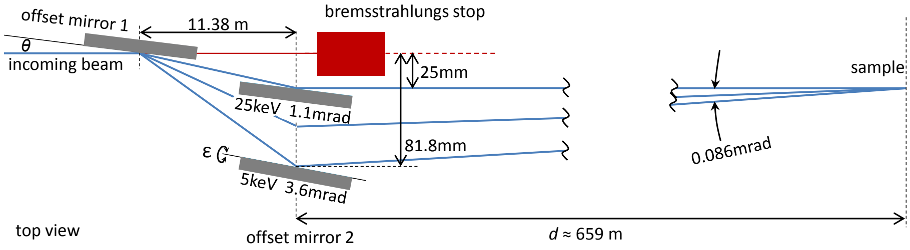

Figure 3.10: Top view of the energy-dependent beam path after the offset mirror

To account for this energy-dependent horizontal offset, all optical elements positioned after the offset mirror need to have an aperture larger than 0.086 mrad times the remaining distance to the sample, or they need to be motorized in the horizontal position. For instance, there are pop-in imaging units at various positions after the offset mirror, which feature a sensitive area of 110 × 40 mm^2 (hor. × vert.) [89]. Other optical elements are: slits (727 m), attenuators (880 m), slits (887 m), monochromator (929 m), and CRL lenses (931 m). To reach the required 25 mm offset at the sample position, the horizontal beam offset varies from 20.3 mm (at 727 m) to 7.1 mm (at 880 m) and 2.5 mm (at 931 m). This has to be taken into account for the mechanical design of the slit systems, attenuators, monochromators, XGMD/XBPM, and CRL lenses.

The vertical beam position is, in principle, unchanged by the offset mirrors. However, by tilting the second mirror, the outgoing beam can be steered upwards or downwards. The vertical displacement Δy as a function of distance to the mirror d is given as $\Delta y = d \sin\epsilon \sin(2\theta)$, where θ is the grazing angle and ϵ the perpendicular tilt angle. This possibility of vertical steering is important to counter the offset introduced by the monochromators downstream. The monochromators introduce a vertical beam offset of 15.4 mm at most (for the Si(220) reflection at 25 keV, see Section 3.3.1, "Monochromator-2—Si(220)"). At the sample position, about 659 m downstream from the second offset mirror, the required tilt is $\sin\epsilon = \frac{15.4\text{ mm}}{659\text{ m}\cdot\sin 2\theta}$, taking a maximum value for the smallest angle θ, namely 1.1 mrad. Hence, $\epsilon_{\text{max}} = 0.59°$. This is within the mechanical limits of the mirror tilt movement [108], meaning that the functionality requested for the MID instrument is available. Further information about the mirror quality, the cooling scheme, the mirror vacuum vessel, and the bending mechanism is in the CDR and TDR of the X-Ray Optics and Beam Transport group [109; 110].

3.1.7 High-energy Laue monochromator

The SASE2 undulator will not only provide SASE radiation in the range of 5–25 keV but also spontaneous radiation above 25 keV. The possibility of lasing in the range above 25 keV was recently discussed [105] and, if high-harmonic lasing proves feasible, the need for a high-energy Laue monochromator will become urgent. The offset mirrors that will deviate the beam around the bremsstrahlung collimator and beam stop will have a limited operation range in energy. Instead, a specialized monochromator for high photon energies is required that can be used instead of the mirrors.

A cryogenically cooled double-crystal monochromator (Laue, diamond) seems to be the most suitable device for this purpose, as shown in a pre-study [109] where operation up to 200 keV photon energy was considered. Synthetic high-pressure high-temperature (HPHT)–grown diamonds of monochromator quality (high purity, Type IIa) are available on the market for this purpose [19; 107]. We note that an operation range of 20–150 keV is desired to overlap with the cutoff of the mirrors and to safely reach the 125 keV that harmonic lasing (fifth harmonic) could provide when the accelerator operates at 17.5 GeV electron beam energy.

In the lowest-energy case (20 keV), the 7σ beam size on the diamond (300 m from the source) will be about 1.3 mm. The Bragg angle θ_B varies between ~ 1° and 9° for the (111) reflection in the specified energy range. This leads to a very large beam footprint on the crystal in symmetric Bragg geometry, which is incompatible with typical sizes of Type IIa diamonds. Hence, a symmetric Laue geometry is favoured and the beam will be at almost normal incidence on the crystals. This will facilitate working with small crystals where an accessible area of 5×5 mm^2 can be tolerated. The Darwin width of the (111) reflection is about $\Delta\lambda/\lambda = 6.6 \times 10^{-5}$, which results in an angular acceptance ($\frac{\Delta\lambda}{\lambda} \tan\theta_B$) comparable with the natural beam divergence at high energies (~ 1–2 µrad). This means that bending of the crystals is not required.

Substituting the offset mirrors, the monochromator must provide the required horizontal offset (25 mm) of the beam, which implies that the second crystal must be movable. At 20 keV, the distance between the crystals is 80 mm, while 620 mm is required at 150 keV. Hence, the second crystal must be on a linear stage with more than 500 mm stroke in the z direction. The stroke can be reduced if a higher-order reflection, e.g. (220) or (400), is used, but this will decrease the Darwin width and lead to less transmission. The Si(111) reflection has about two times the Darwin width of C(111) and would match the SASE bandwidth better, but it probably will be excluded for two main reasons: beam absorption would seriously limit its performance at this position rather close to the source, and almost 1 m of stroke would be needed for the second crystal.

Monochromators of this kind have been built before and are operating at e.g. the Advanced Photon Source (APS) in Argonne, Illinois, and ESRF. Keeping the bent crystal shape stable and eventually combining with cryocooling have been the biggest challenges in most cases. Since crystal bending is not required here, the design of the crystal holders can probably be rather simple and cryocooling implemented in an efficient way.

The mechanical design could follow rather closely that of the HARWI monochromator, which was used at the Helmholtz-Zentrum Geesthacht (HZG) beamline at DESY's DORIS III synchrotron. Here, the first crystal position was fixed but with the option to adjust the incidence angle and tilt to select the desired energy and send the beam towards the second crystal. The second crystal would have the same degrees of freedom as the first crystal but in addition be movable along z and x to maintain the requested fixed offset. Placed on a girder in a UHV vessel with the necessary alignment tools, we estimate that the entire high-energy monochromator would require about 1.5 m length along the beam. This space will be reserved at about 307 m from the source (Figure 3.1 on page 15).

3.2 MID beamline

The MID beamline is the central beamline of SASE2, meaning that the beam continues straight towards the MID instrument when the distribution mirrors are not in use. The distribution mirrors are only required to operate the HED instrument and possibly a future third instrument (NNN). All components described in the following sections belong only to the MID instrument and are hence located on the central branch. An overview of these device can be found in Figure 3.11.

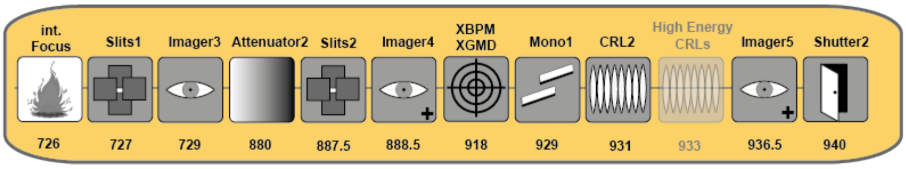

Figure 3.11: Main components in the MID photon tunnel with distances after the source point as indicated

3.2.1 Slits

The interaction of the XFEL beam with optics components or diagnostic devices can cause intense scattering signals. This unwanted background must be removed using a slit system. Since the scattered intensity can be strong, the slit blades have to withstand intense photon beams and high heat loads. A considerable safety margin must also be incorporated to account for accidental exposures of the slits to the flanks of the direct beam. Hence, the slits should not be thought of as classical beam-defining apertures (which will only work for the lowest bunch charge operation modes) but rather as devices that remove stray scattering and clean the tails of the beam. One particularly useful position for such a tail-cleaning slit system is at the intermediate focus, when operating the instrument in this focusing geometry (see (c) in Figure 5.2 on page 75).

A slit blade made as a sandwich of B_4C and tungsten seems to be the best solution to fulfil the heat load requirements. Damage threshold calculations of B_4C and tungsten can be found in Section 4.5, “Thermal model for B_4C”, and Section 4.6, “Tungsten slit blades”. The slit blades must be individually movable with 1 µm precision and the temperature of each blade logged at 10 Hz. Possibly, a photoelectron or ion detection system can be installed at a few critical slit locations, e.g. close to the slit at the intermediate focus position. Such a system would allow a fast reaction to a possible onset of ablation. We propose to install slit systems at three different locations: at 726 m (close to the intermediate focus), at 887.5 m, and at 947.5 m (after Monochromator-2).

3.2.2 Monochromator-1—Si(111)

The energy bandwidth of the incoming radiation will be different for SASE operation and for self-seeded operation. For SASE operation, the energy width of the incoming radiation depends on the electron and photon energy as well as the bunch charge, and is expected to be around 1×10^{-3} [3, p. 183]. For self-seeded operation, the beam is expected to be nearly Fourier transform–limited, and thus energy width and pulse duration are related via the Heisenberg time–energy uncertainty principle with $\frac{\Delta E}{E} = \frac{\hbar}{2\Delta tE}$. For example, at LCLS, a relative bandwidth of $\frac{\Delta E}{E} = 5 \times 10^{-5}$ was demonstrated [4] in seeded mode at 9 keV.

If the key criterium is not energy resolution but rather transmitted flux, a Si(111) monochromator is the natural choice for SASE operation. Furthermore, for photon pulses with $\Delta t = 10$ fs duration and an energy of $E = 5$ keV, the corresponding energy resolution needs to be worse than $\frac{\Delta E}{E} \geq \frac{\hbar}{2\Delta tE} = 4.1 \times 10^{-4}$ if the pulse length is to be maintained after the monochromator. Si(111) has the largest bandwidth of any Si reflection, with an intrinsic energy resolution of $\frac{\Delta E}{E} = 1.4 \times 10^{-4}$. In the case of self-seeded operation, the expected relative energy width of the dominant peak in the spectrum can be on the order of 10^{-5} (see above). While this is a sufficient degree of monochromaticity for many experiments, there are still large tails of spontaneous radiation extending over a much larger energy range. A Si(220) monochromator will provide a bandwidth comparable to the width of the dominant peak in the seeded spectrum, but can eliminate the extended tails. The bandwidth of the Si(220) reflection is about 5.9×10^{-5}. Furthermore, since the split and delay line downstream will most probably use Si(220) reflections, a Si(220) pre-monochromator will be the ideal fit. Therefore, the plan is to install both a Si(111) and a Si(220) monochromator at MID. If an even smaller bandwidth is required, it will be possible to use the first monochromator with the Si(333) or Si(444) reflections, though for a reduced energy range due to limitations in accessible angles.

The two positions foreseen for monochromators are at 929 m (end of tunnel) and at 946 m (optics hutch). In all focusing geometries (see Chapter 5, “Beryllium lenses”), the expected beam size at 929 m is larger than at 946 m. Accordingly, the power density is smaller for the first monochromator. For the Si(111) crystal, the Bragg angles will be smaller than for Si(220). Thus, the footprint on the crystal will in general be larger and one might tolerate a higher heat load. Furthermore, the angular acceptance is larger for the Si(111) case, and thus the generation of a slight heat bump can probably be better tolerated for the Si(111) case. This would suggest to position the Si(111) monochromator at 946 m and the Si(220) monochromator at 929 m. On the other hand, this order would preclude a stepwise monochromatization with Si(111) coming first followed by Si(220). Concerning operation of the split and delay line (SDL) with Si(220) crystals, a Si(220) monochromator at 946 m close to the SDL is the more stable solution. Therefore, we conclude that the Si(111) monochromator should be installed at 929 m and the Si(220) monochromator at 946 m. This is also the smallest-risk solution, as it places the least sensitive device at the position with the lowest power density.

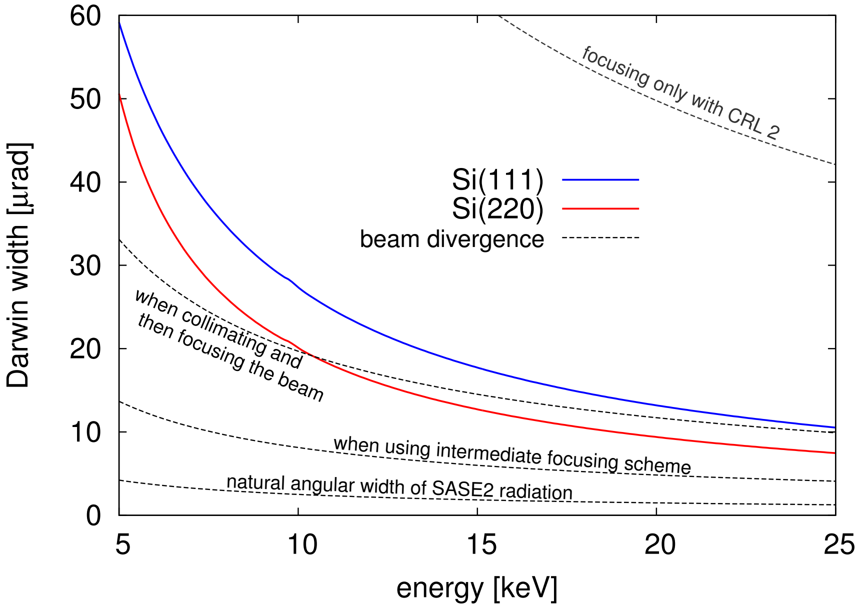

Figure 3.12: Angular acceptance (Darwin width) of the Si(111) and Si(220) reflection compared to the expected beam divergences in FWHM. Different cases are considered: the natural divergence of the SASE radiation according to Equation A.1 on page 159; the increased divergence using the *collimation then focusing* scheme (labelled (a) in Figure 5.2 on page 75); the divergence using an *intermediate focusing* scheme (labelled (b) and (c) in Figure 5.2 on page 75); and finally the divergence using only the second CRL transfocator (CRL-2) for focusing (labelled (d) in Figure 5.2 on page 75). To have a good transmission in the latter case, it is necessary to place the monochromator upstream of CRL-2.

The angular acceptance (Darwin width) of the Si(111) and the Si(220) reflection are shown in Figure 3.12. The natural divergence of the XFEL beam is also shown and is clearly below the angular acceptance for all energies. The throughput of the monochromators will also be almost ideal for the *collimation then focusing* and the *intermediate focusing* schemes. The choice of having the Si(111) monochromator upstream of CRL-2 originates from the last focusing geometry considered. Here, CRL-1 is not used, and the beam is left with its natural divergence to propagate down to CRL-2, where it is focused onto the sample (see (e) in Figure 5.2 on page 75). In this case, the divergence is too large to be compatible with a monochromator, so CRL-2 is placed downstream of the Si(111) crystals. This focusing geometry is not compatible with the use of Monochromator-2, Si(220), or the split and delay line.

The mechanical design is based on an artificial channel-cut monochromator (ACCM) concept operating in UHV and with cooling of the crystals. If unwanted vibrations are present in the environment, a channel-cut design will limit the beam instabilities to a minimum. In an artificial channel-cut design, the crystals can be polished individually before being mounted in the crystal cage, leading to better surface finish than for monolithic channel cuts. However, the drawback of any channel-cut realization is a variable beam offset that depends on the photon energy. The rotational motion (Bragg angle) required will be realized in vacuum using a linear stage acting on a sine bar assembly that houses the monochromator crystals (Figure 3.13 on the next page). This design limits the total stroke of the Bragg rotation to 35°. A weak link between the two crystals allows us to align the Bragg planes of the two crystals to a parallel orientation, or to achieve a de-tuning and suppress higher-order reflections.

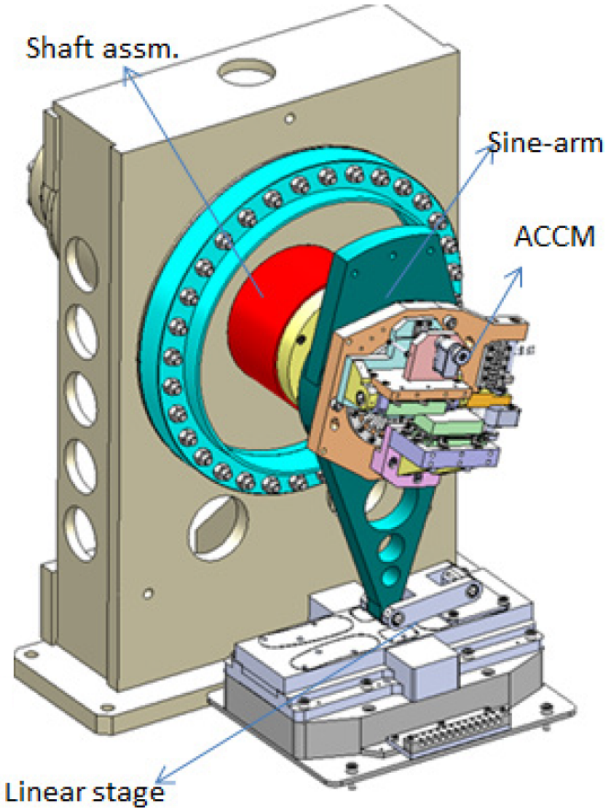

Figure 3.13: Mechanical design of the monochromator [110]. The artificial channel-cut monochromator (ACCM) crystals are mounted on a sine arm for precise Bragg angle control and stability. The linear stage shown at the bottom pushes on the sine arm. The rotation is around the horizontal shaft axis.

The MID beamline is designed for energies between 5 and 25 keV. Furthermore, all optical components should, if possible, transmit a vertical beam size of 7σ. This defines the size of the two crystals and determines the energy-dependent vertical offset of the monochromatic beam. Details of the calculation can be found elsewhere [109, p. 73]. The mechanical parameters of Monochromator-1 are shown in Table 3.4 on the facing page.

Table 3.4: Mechanical parameters of Monochromator-1 operating with Si(111) reflections

Channel-cut gap	5.5 mm	
Crystal length	60 mm	
Required angle stroke	18.75°	
	5 keV	25 keV
Bragg angle θ_B	23.29°	4.54°
Beam offset $o(E)$	10.10 mm	10.96 mm

Figure 3.14 on the next page shows the situation at 5 and 25 keV, as well as the energy dependence of the beam offset. In order to achieve a compact design of the monochromator and to limit the beam offset generated by the monochromator, the gap and the crystal length of the two crystals is kept as small as possible, while still allowing to let at least 6σ of the unfocused beam pass, preferably even 7σ. For this reason, a gap of 5.5 mm and crystal lengths of 60 mm have been chosen. With a gap of 5.5 mm, the beam offset varies by less than 1 mm between 5 and 25 keV. As can be seen in the inset of Figure 3.14 on the following page, 7σ of the unfocused beam is transmitted for energies between 7 and 23 keV, decreasing to 6σ at 5 and 25 keV. The center of rotation is chosen on the surface of the first crystal, close to its downstream edge. This limits the necessary monochromator height adjustments when changing the energy.

Cooling the crystals down to 100 K will improve the throughput of the monochromator by a factor of two in typical operating conditions [109, pp. 66]. As liquid nitrogen is not foreseen in the tunnel, a pulse tube cooler will provide this cooling. Further information about the monochromator design and its performance can be found in the CDR and TDR of the X-Ray Optics and Beam Transport group [109; 110].

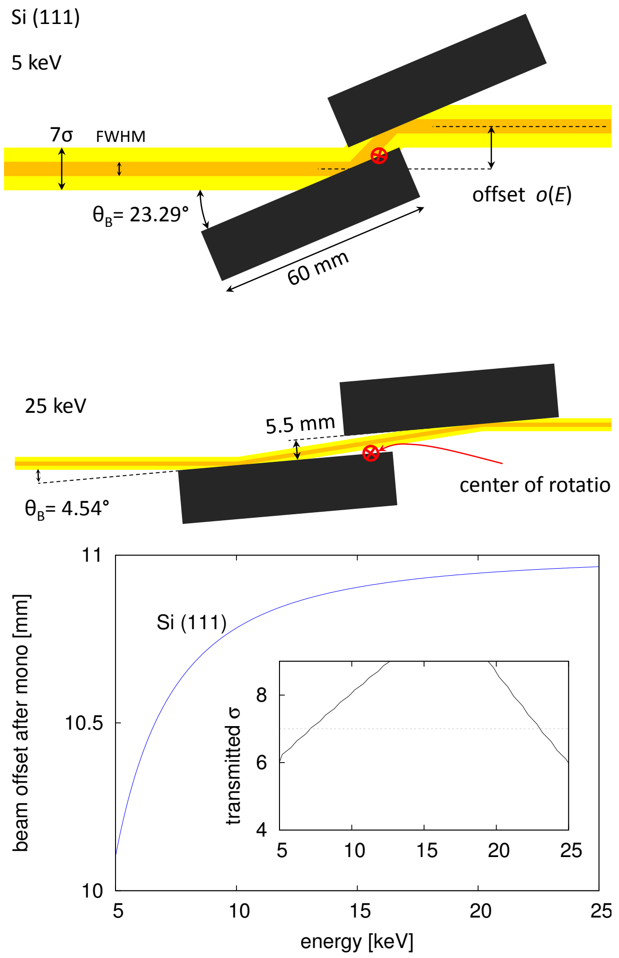

Figure 3.14: The two crystals of the Si(111) monochromator. The Bragg rotation is on the surface of the first crystal. Using a gap of 5.5 mm leads to an energy dependent beam offset ranging from 10.10 to 10.96 mm. Between 7 and 23 keV, 7σ of the unfocused beam is transmitted by this arrangement. At lower energies, the inner edges of the crystals reduce the transmitted beam to 6σ at 5 keV. Likewise, at higher energies the outer edges of the crystals reduce the transmitted beam to 6σ at 25 keV, see inset

3.2.3 Secondary lens stack (CRL-2)

Imaging experiments aiming at high spatial resolution via small beams, or other methods where a small scattering volume is required, will require focused beams impinging on the sample. Typically, the beam size must be in the range from 1 to 10 µm. Nanofocusing is a separate challenge that is treated in Section 7.4, “Nanofocusing”. Sub-10 µm beams are also required for speckle measurements (XPCS, CXDI) where a small beam size will help to resolve the speckles on a

2D detector with coarse pixel resolution. The CRL-1 lens stack at 235 m is not capable of focusing the full beam to a size below 100 µm on the sample position as shown in Table A.4 on page 163 and Figure A.2 on page 164. Therefore, to enable sub-10 µm foci, it is mandatory to install a second CRL stack (CRL-2) closer to the sample.

By placing this device at the end of the tunnel (931 m after the source point and ~ 28 m upstream of the sample), different beam sizes on the sample are possible, depending on the configuration of CRL-1 (*collimation then focusing* scheme or *refocused* scheme; see Figure 5.2 on page 75). Figure 3.15 shows the beam size after CRL-2, as a function of energy and position for the focusing schemes (c) and (d) in Figure 5.2 on page 75, namely focusing with CRL-1 and with CRL-2.

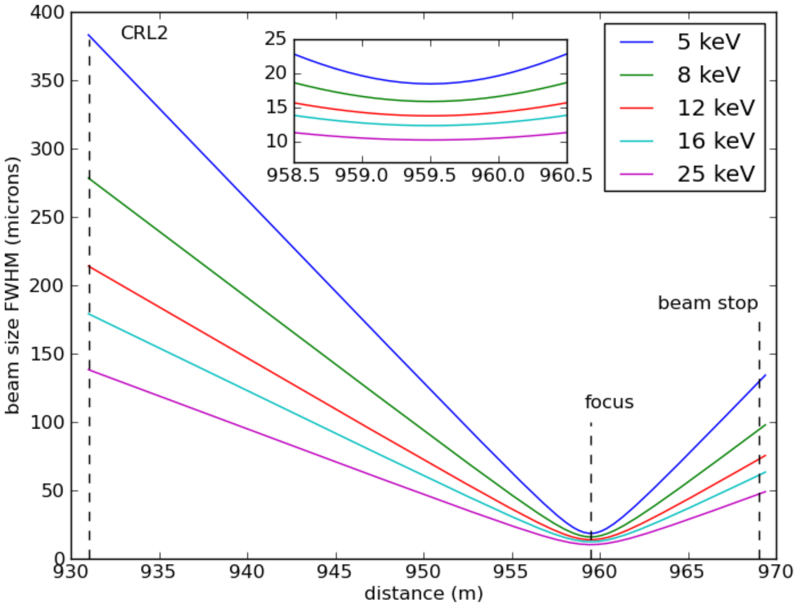

Figure 3.15: Evolution of beam size after CRL-2 in the *intermediate focus* geometry. The graphs show the diameter (FWHM) of the beam at 5 keV (blue), 8 keV (green), 12 keV (red), 16 keV (cyan), and 25 keV (purple). The dashed lines indicate the position of the CRL-2 stack, the focus at the sample position, and the position of the beam stop (beamline ends). The calculations are based on Equation 3.1 on page 23 and Equation 3.2 on page 23. Further information about the different focusing geometries is given in Chapter 5, "Beryllium lenses".

Figure 3.16 on the following page shows the beam size after CRL-2 as a function of energy and position for the focusing scheme (a) in Figure 5.2 on page 75, namely collimating with CRL-1 and then focusing with CRL-2. These results are also shown in Table A.1 on page 160 and Table A.3 on page 162.

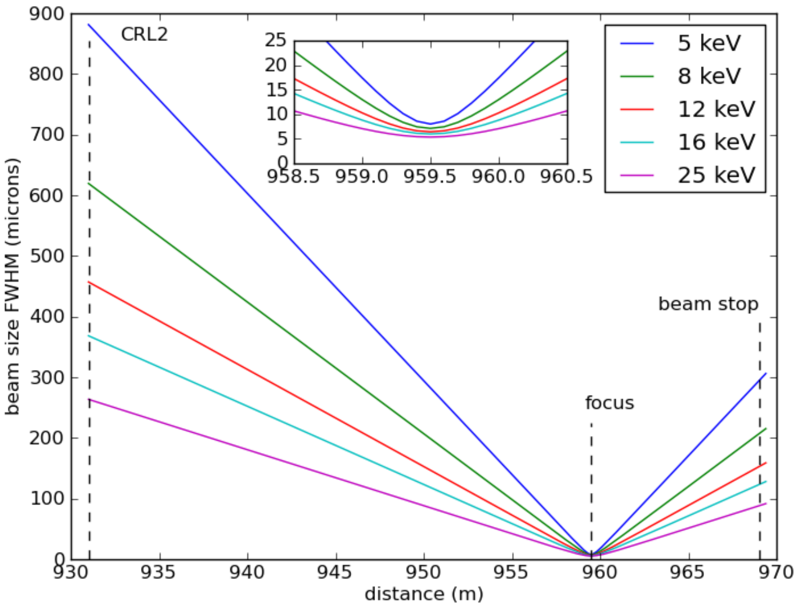

Figure 3.16: Evolution of beam size after CRL-2 in the *collimation then focusing* geometry. The graphs show the diameter (FWHM) beam at 5 keV (blue), 8 keV (green), 12 keV (red), 16 keV (cyan), and 25 keV (purple). The dashed lines indicate the position of the CRL-2 stack, the focus at the sample position, and the position of the beam stop. The inset shows a magnification of the area around the sample position at 965.5 m. The calculations are based on Equation 3.1 on page 23 and Equation 3.2 on page 23. Detailed information about this focusing geometry can be found in Chapter 5, "Beryllium lenses".

Furthermore, it is possible to use only CRL-2 for focusing, without pre-focusing or collimation by CRL-1. The Si(111) monochromator at 929 m is designed to transmit the full unfocused beam. Using only CRL-2 will allow the beam sizes at the sample position to approach ~1 µm. However, as a significant number of Be lenses will be required and because the beam at CRL-2 is relatively large, the effective aperture of the lens stack will be comparable to or even smaller than the beam FWHM at the lens position. In this case, the beam size at the focal spot depends on the specific choice of the lenses in CRL-2, and the transmission is reduced with respect to the other focusing geometries. More details can be found in Chapter 5, "Beryllium lenses". Figure A.3 on page 166 and Table A.5 on page 165 show the variation in beam size from CRL-2 to the sample position. The design of the CRL-2 housing and mechanics can be a copy of CRL-1 (see Section 3.1.3, "Primary lens stack (CRL-1)"), as eight actuators also are required for CRL-2 (see Chapter 5, "Beryllium lenses").

A third CRL unit is required adjacent to CRL-2, at 932 m, in order to focus beams with photon energies higher than 25 keV. This option will become interesting if the proposed high-harmonic lasing scheme proves feasible. Potentially, the European XFEL can then be brought to lase at photon energies up to 100 keV, and a substantial amount of lenses is needed to focus such beams. This will not be part of the baseline instrumentation at MID, but a placeholder is reserved for a future high-energy transfocator (CRL-3).

3.3 Optics hutch

The MID optics hutch is located in the experiment hall starting at about 944 m downstream of the source point. As shown in Figure 3.17, the hutch contains a slit system and a pop-in imaging unit, as described earlier (see Section 3.2.1, “Slits”, and Section 3.1.4, “Imager”). Furthermore, a second monochromator (Mono-2) and a split and delay line (SDL) are located here. The optics hutch will also host a transfer pipe to allow operation of the HED instrument downstream. At this location, the separation between the MID and HED photon beamlines is approximately 1.4 m. On the other side, 90 cm is available between the MID beamline and the wall of the optics hutch. This value is a compromise between various space requirements, for instance of the split and delay line, which will be rather wide, and the wish to leave some free space for a possible future third instrument (NNN) at SASE2. The optics hutch will be temperature-stabilized to 0.5 K through air conditioning. Direct cooling of sensitive devices, e.g. the monochromator and the split and delay line, and local areas with higher stability (0.1 K) will be implemented. The optics hutch is a radiation safety hutch, and the requirements for the shielding have been estimated earlier [6]. A suggested rough layout of the optics hutch is shown in Figure 3.18 on the next page.

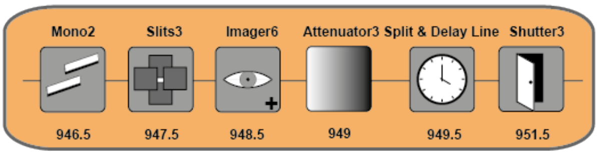

Figure 3.17: Schematic representation of the components in the MID optics hutch

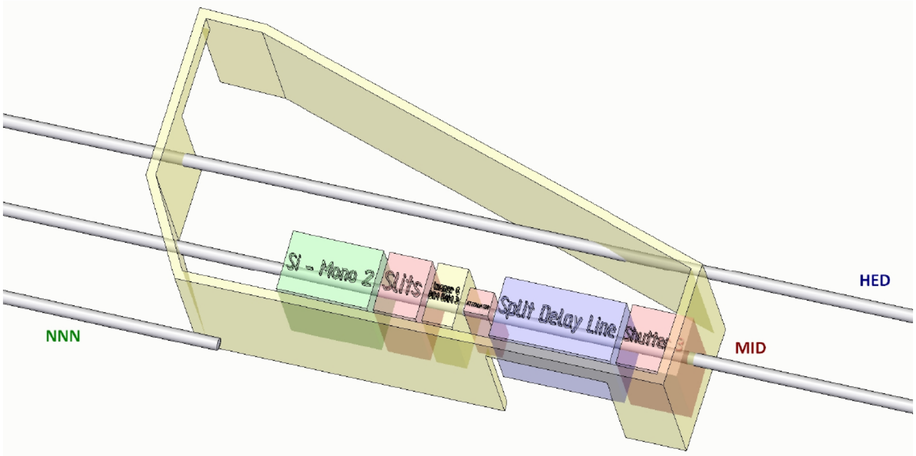

Figure 3.18: 3D model of the MID optics hutch. Two access doors are required as well as a roof hatch for manipulating equipment with the experiment hall crane (up to 20 t). A smaller local crane will also be installed under the roof in the optics hutch. Supplies of cooling liquids, gases, and electricity will access the hutch through custom-made chicanes still to be defined. The air conditioning system will probably be integrated in the roof adding to the total height of the hutch.

3.3.1 Monochromator-2—Si(220)

The design of the hard X-ray monochromator in the optics hutch is similar to the design described earlier (see Chapter 3.2.2, “Monochromator-1—Si(111)”) for the monochromator at the end of the tunnel. The main difference is the crystal reflection used here, Si(220), with a Darwin width of about $\Delta E/E = 5.9 \times 10^{-5}$. The position of this monochromator is at 946 m after the source. The design energy range is again 5 to 25 keV. Following Ref. [109, p. 73] and similar to Section 3.2.2, “Monochromator-1—Si(111)”, we obtain the mechanical parameters for the monochromator as listed in Table 3.5.

Table 3.5: Mechanical parameters of Monochromator-2 operating with Si(220) reflections

Channel cut gap	7.8 mm	
Crystal length	48.3 mm	
Required angle stroke	32.80°	
	5 keV	25 keV
Bragg angle θ_B	40.22°	7.42°
Beam offset $o(E)$	11.88 mm	15.43 mm

The required stroke of 32.80° is close but still within the specifications of the monochromator design (35°). The vertical beam offset after the monochromator varies more than in the case of Si(111). This is caused by the higher Bragg angles and the larger gap between the channel-cut crystals. Figure 3.19 shows the situation at 5 and 25 keV, as well as the energy dependence of the beam offset. With the gap and crystal lengths shown here, it is possible to transmit 7σ of the unfocused beam at 946 m for all energies between 5 and 15 keV.

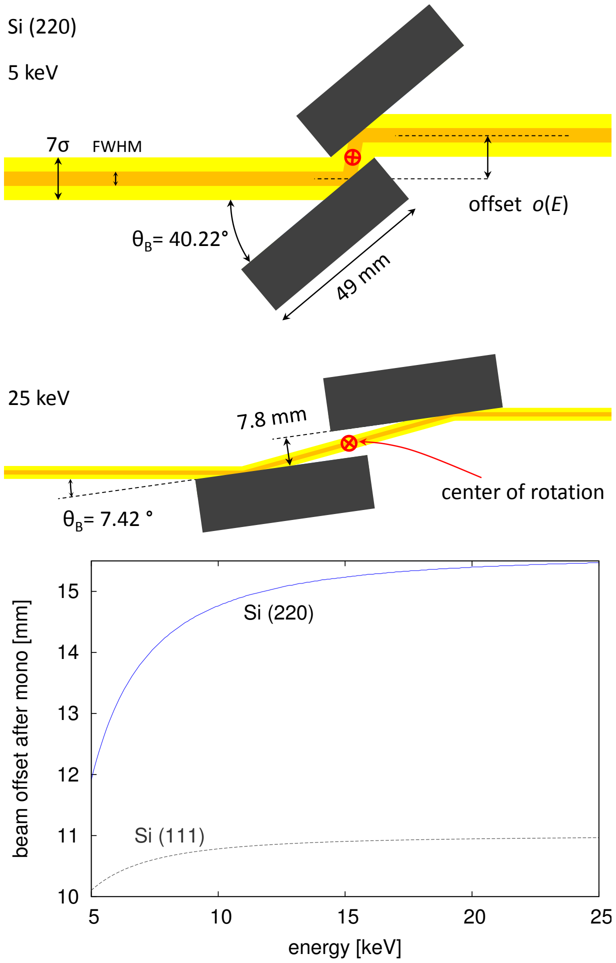

Figure 3.19: The artificial channel-cut crystals of the Si (220) monochromator. The Bragg rotation axis is in the centre of the two crystals. The minimum gap needed to transmit the unfocused 7σ beam size at 946 m is 7.8 mm, and the minimum crystal length is 48.3 mm. The outgoing beam is shifted by an offset $o(E)$.

3.3.2 Attenuator-3

In contrast to the previous attenuation devices (see Section 3.1.2, “Attenuator”), Attenuator-3 will be used only to optimize the beam intensity on the sample. This means that the heat load on upstream optical elements (monochromators and mirrors) can remain constant (for optimum stability) and that gas diagnostics can operate with constant high intensity (for the best resolution), while only the intensity incident on the sample is varied. Attenuator-3 is also located upstream of the split and delay line, since this device will be particularly sensitive, and fine tuning of the intensity incident on the beam splitter crystal may be required. Due to space constraints in the experiment hall and hutches, a more compact design of the attenuator is desired at this location. Attenuator-3 will consist of four individual attenuator stacks with six different attenuator targets each. It will require cooling, temperature monitoring, and encoded stepper motor motions like the upstream attenuators. The position precision required for attenuators is only about 10–100 µm, but the change from one attenuator state to another has to be swift.

Like the previous attenuation devices, Attenuator-3 will be equipped with three different targets—silicon, B_4C, and diamond foils. The materials are chosen to have the best compromise between absorbing power and high damage thresholds. Table 3.6 shows the selected attenuation thicknesses and positions. In this way, the beam can be attenuated down to a factor of 3×10^{-7}.

Table 3.6: Distribution of the different absorber foils at Attenuator-3. Each of the four arms contains two diamond, two B_4C, and two silicon absorbers. The maximum attenuation at 25 keV will be about 3×10^{-7}.

Position	Material	Arm 1	Arm 2	Arm 3	Arm 4
1	Diamond	0.1 mm	0.2 mm	0.4 mm	0.8 mm
2	Diamond	0.4 mm	0.8 mm	1.6 mm	3.2 mm
3	B_4C	0.2 mm	0.4 mm	0.8 mm	1.6 mm
4	B_4C	0.8 mm	1.6 mm	3.2 mm	6.4 mm
5	Silicon	0.5 mm	1.0 mm	2.0 mm	4.0 mm
6	Silicon	2.0 mm	4.0 mm	8.0 mm	16.0 mm

3.3.3 Split and delay line

The short pulses coming from the SASE2 undulator within a pulse train have a time separation of 220 ns. It seems possible to use special XFEL operation modes, where this time can be reduced to 800 ps (RF) for a few pulses per train. Shorter time separation between individual pulses cannot be provided by the accelerator, however. For X-ray pump and X-ray probe experiments, as well as for XPCS experiments aiming at ultrafast dynamics, it is therefore necessary to apply specific optics to generate X-ray pulses with shorter time delays.

For this purpose, a split and delay line (SDL) unit is foreseen at the end of the optics hutch (Figure 3.20). Here, an X-ray pulse is split into two parts that can be offset in time against each other by controlling the path length difference. In this way, X-ray pulse pairs with a temporal separation down to a few femtoseconds can be generated. Further information about the split and delay line can be found in Chapter 6, “Split and delay line”.

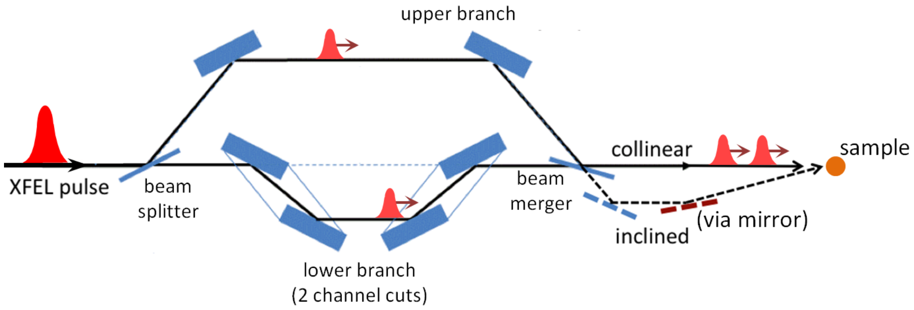

Figure 3.20: Concept of a split and delay line (SDL). The incident XFEL pulse is split into two parts by a thin crystal (beam splitter): half the intensity is transmitted through the crystal, half the intensity is Bragg-diffracted into the upper branch. This half pulse travels a longer distance than the pulse passing through the lower branch by two channel-cut crystals. The two pulses arrive with a time delay of Δt. The two parts merge again at the thin crystal beam merger (collinear option), or travel on two different paths towards the sample. The latter option requires the use of a mirror after the SDL to have the beams overlapping at the sample.

3.4 Experiment hutch

The experiment hutch is the main hutch of the MID instrument. It will host the experiment chambers, the detectors used for the experiments, and other main instrument parts (Figure 3.21 on the following page). Requirements for air conditioning and supplies will be similar to the optics hutch specifications described above. The form factor of the hutch is determined by the HED beam pipe, which passes right on the other side of the southern hutch wall (Figure 3.22). Again, due to space constraints coming in particular from the size of the AGIPD system and the need to operate it in forward scattering geometry (SAXS), the minimum distance from the MID beamline to the wall is set to 90 cm. Close to the experiment chamber, 20 cm extra space is required to accommodate the vertical scattering arm. This requirement determines the location and shape of the southern hutch wall. On the other side, there is much more space, with ~ 8.5 m distance to the walkway between the SASE2 and U2 areas. In this direction, the large detector arm that carries the AGIPD system can swing out from the SAXS to the WAXS regime and cover scattering angles 2θ from 0° to 60° with up to 8 m sample–detector distance. The length of the hutch is limited by the HED hutch downstream and the total length of the SASE2 area, which is about 42 m. We believe that the planned hutch length of about 16 m is sufficient to host all the equipment foreseen.

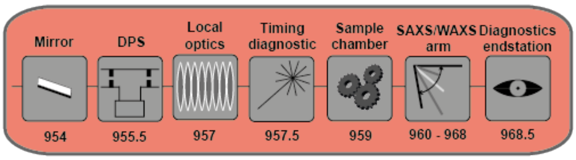

Figure 3.21: Pictograms of the devices in the MID experiment hutch

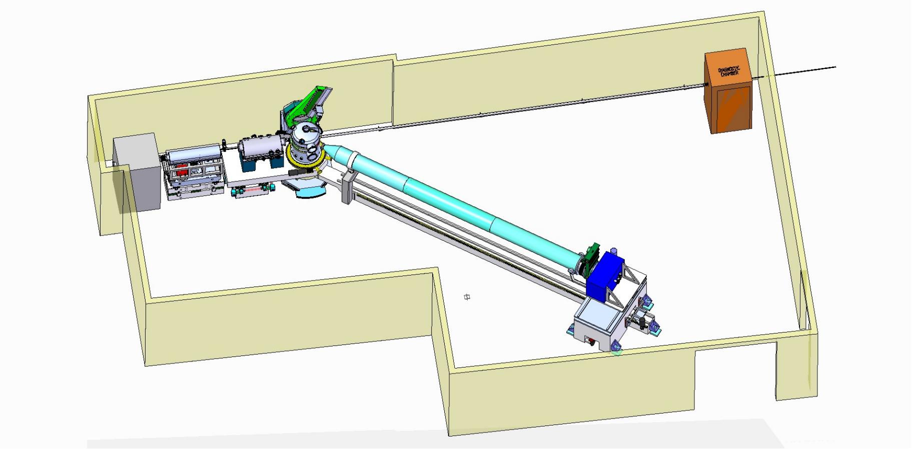

Figure 3.22: 3D model of the MID experiment hutch. One wide double door and separate access to the MID control hutch are required, as well as two roof hatches for manipulating equipment with the large crane in the experiment hall. A smaller local crane is foreseen to be installed under the roof. As for the optics hutch, supplies of cooling liquids, gases, and electricity will access the hutch through custom-made chicanes still to be defined. The air conditioning system will probably be integrated in the roof, hence adding to the total height of the hutch (4 m to the ceiling inside).

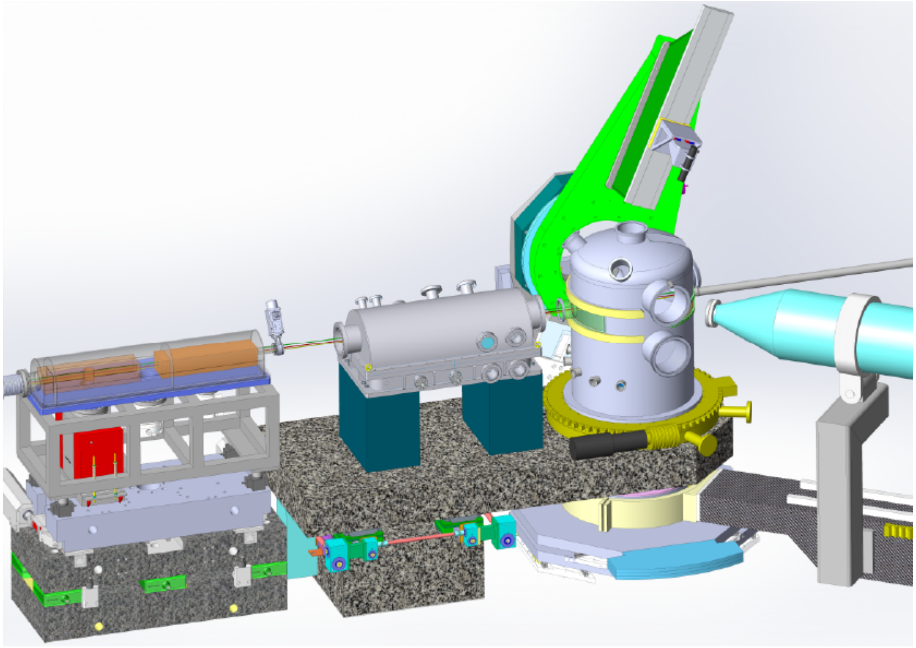

Figure 3.23: Zoom on the differential pumping section, the vessel for the local optics and timing diagnostic, and the sample chamber

3.4.1 Mirrors

Two mirrors, one reflecting upwards, one downwards, will be installed in the experiment hutch as close as possible to the sample but upstream (on the UHV side) of the differential pumping section (Figure 3.24 on the following page). This is mandatory to avoid contamination of the mirrors. The upwards reflecting mirror will be used together with the SDL in the mode where two beams emerging from the SDL travel in parallel but with a vertical offset of about 20 mm between them (inclined mode of Figure 3.20 on page 45). The beam of the upper SDL branch will be intercepted by the last SDL crystal at a position below the beam arriving from the lower branch. The delayed beam coming from the upper branch will then be directed upwards by the mirror in order to recombine at the sample position with the beam coming from the lower channel-cut branch. The sample will be hit by two beams that arrive at different times and at different angles so that a spatial separation is possible at the level of the detector.

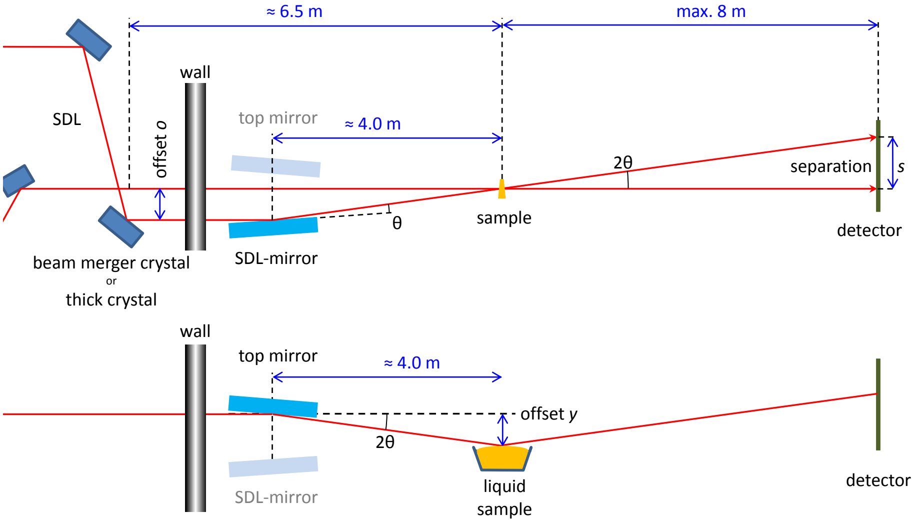

Figure 3.24: *Top*: Use of the upwards reflecting SDL mirror to direct the delayed pulse coming from the upper branch of the delay line back to the sample. *Bottom:* Use of the downwards reflecting top mirror to investigate liquid samples.

The downwards deflecting mirror will be employed to direct the beam onto a liquid surface for grazing-incidence scattering studies. The surface sensitivity can be tuned by changing the incidence angle around the critical angle of total external reflection of the sample. The mirrors should be retractable from the beam when they are not in use.

The mirror substrates will be made of Si. The SDL mirror will have a B_4C coating. The top mirror (liquids) should have two stripes, one coated with B_4C for photon energies up to about 10 keV, the other with a high-Z material, e.g. Pt or Pd, to increase the operation range to higher angles at 25 keV (Figure 3.25 on the facing page). When the mirrors are operated with the split beam coming from the delay line, radiation damage should not be an issue. For the top mirror used for the study of liquids, attenuation might be necessary when using the high-Z stripe. Cooling needs to be implemented for this mirror. For the upwards reflecting mirror used with the SDL, the intensity is much lower and an uncooled mirror might be fine.

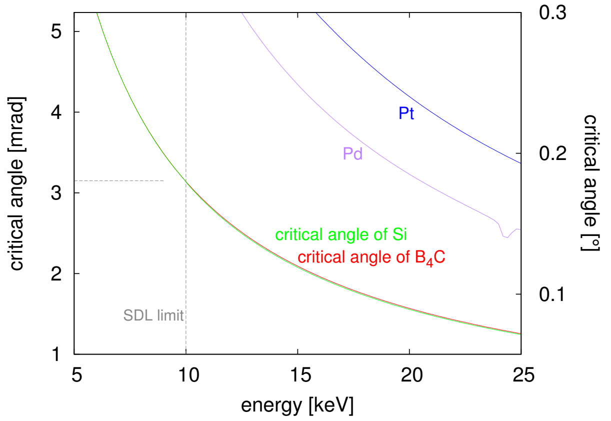

Figure 3.25: Critical angle for B_4C, Si, Pt, and Pd

Both mirrors will be housed in a common mirror chamber at about 4.0 m upstream of the sample (~ 954 m from the source). This is the closest position to the sample possible, as the differential pumping section, the local optics, and the timing diagnostic unit require space in between. This position and the critical angle of the mirror coatings (Figure 3.25) impose the working angles and the required mirror lengths. Beam sizes at the mirror as given in Table A.3 on page 162 and Table A.5 on page 165 are used in the calculations for the mirror length. The results for the upwards reflecting mirror (used with SDL) are given in Table 3.7.

Table 3.7: Parameters of the mechanical concept for the mirror chamber

Working angle	**B_4C @ 2.5 mrad**	**B_4C @ 3.15 mrad**
Necessary offset of lower SDL beam	−20 mm	−25.2 mm
Required mirror length for $7\sigma = 1.75$ mm incident beam (only CRL-2 focusing at 5 keV)	700 mm	556 mm
Required mirror length for FWHM = 0.94 mm incident beam (collimated beam at 5 keV)	376 mm	298 mm
Required mirror length for $7\sigma = 0.41$ mm incident beam (collimated then focused beam at 5 keV)	164 mm	130 mm
Max. separation at detector (8 m)	40 mm	50.4 mm

When investigating liquid samples, the incident beam needs to be below the critical angle of the sample. Often, the choice is to work at 80% of the sample's critical angle. The critical angle of water is 0.25° at 5 keV, 0.128° at 10 keV, and 0.05° at 25 keV. Other organic liquids have critical angles of the same order of magnitude. The top-mirror incident angle θ needs only to be half of this value. The B_4C coating can be used nicely in these cases. The critical angle for Hg is 0.75° at 5 keV and 0.153° at 25 keV; in fact, half the critical angle of Hg is very similar, but slightly higher, than the critical angle for B_4C. A high-Z stripe, such as Pt on the top mirror, might be beneficial here, but Pd, Ru, or Rh stripes could be used as well.

Mirrors that are as long as the offset mirrors will not be affordable here and are difficult to implement with respect to space. We will consider operating with a *collimated then focused* beam. As seen in Table 3.7 on the previous page and Figure 3.26, a 400 mm long mirror is sufficient for this at all energies, when working close to the critical angle and down to 1 mrad at 5 keV. The slope errors should be below 0.1 µrad and the roughness as small as possible.

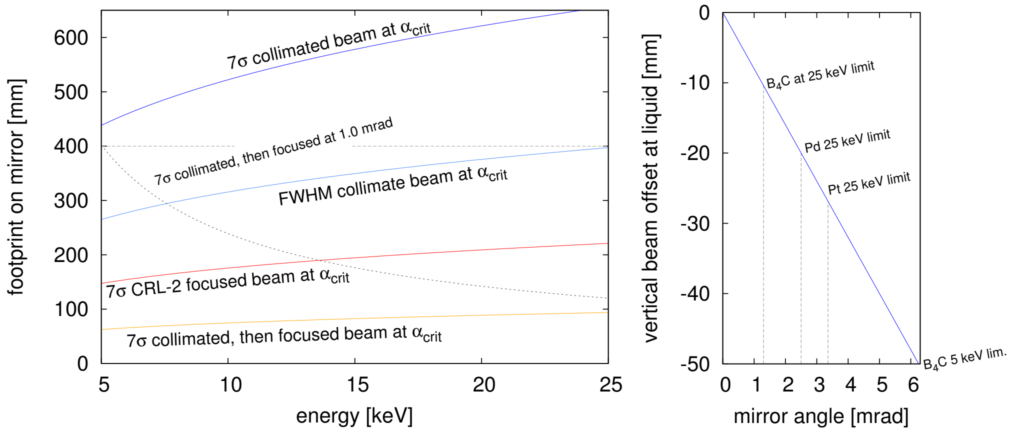

Figure 3.26: *Left:* Footprint on the mirror when operating it at the critical angle of B_4C. *Right:* Vertical beam offset at the sample position.

3.4.2 Differential pumping section

Up to 955.5 m after the source, the beam transport system and the installed components will operate under UHV conditions with a pressure of about 10^{-9} mbar. The experiment chamber does not always allow such good vacuum conditions, especially during experiments with exhalable materials exposed in the chamber. This is for instance the case when a liquid injector is operated. The estimated vacuum in this section will be about 10^{-4} mbar, but can in the worst case approach 10^{-1} mbar. An X-ray transparent window could be used at the entrance of the chamber, but, except in special cases, we discard this option due to the lack of suitable window materials. We note that such a window would be close to the sample and hence parasitic scattering could contaminate the signal from the sample that in many cases is very weak. The best choice would probably be high-quality diamond (Type IIa), but this will be difficult to obtain in the required size. The risk is that scattering from even quasi-perfect diamond windows would overshadow the signal, e.g. from water, and this is obviously not tolerable. Therefore, a windowless solution is preferred with a differential pumping section (DPS) that connects the UHV and the poor-vacuum parts of the beamline.

The DPS consists of three different chambers: one equipped with an ion pump and two with turbomolecular pumps (for specifications, see Table 3.8). The individual sections are separated by 40×4 mm^2 (vert. × hor.) differential pumping apertures made of B_4C. These large apertures allow transmission of all the different beam configurations given by the split and delay line, the mirrors, and the monochromators without adjusting the DPS. Calculations show that with three chambers and a total length of ~ 1.5 m from the first to the last aperture, the required specifications can be reached. This setup will be installed 955.5 m from the source and is inspired by previous designs in use [36; 118; 33]. The current concept of the DPS is shown in Figure 3.27 on the following page.

Table 3.8: Parameters of the differential pumping section. The chambers are numbered in the beam direction.

DPS	**1**	**2**	**3**
Pump type	Ion pump	Turbo pump (Pfeiffer HiPace 300)	Turbo pump (Pfeiffer HiPace 80)
Pumping power	300 l/s	260 l/s	71 l/s
Avg. pressure in the section	4×10^{-8} mbar	10^{-5} mbar	10^{-3} mbar
Pump port size	60 mm	100 mm	60 mm

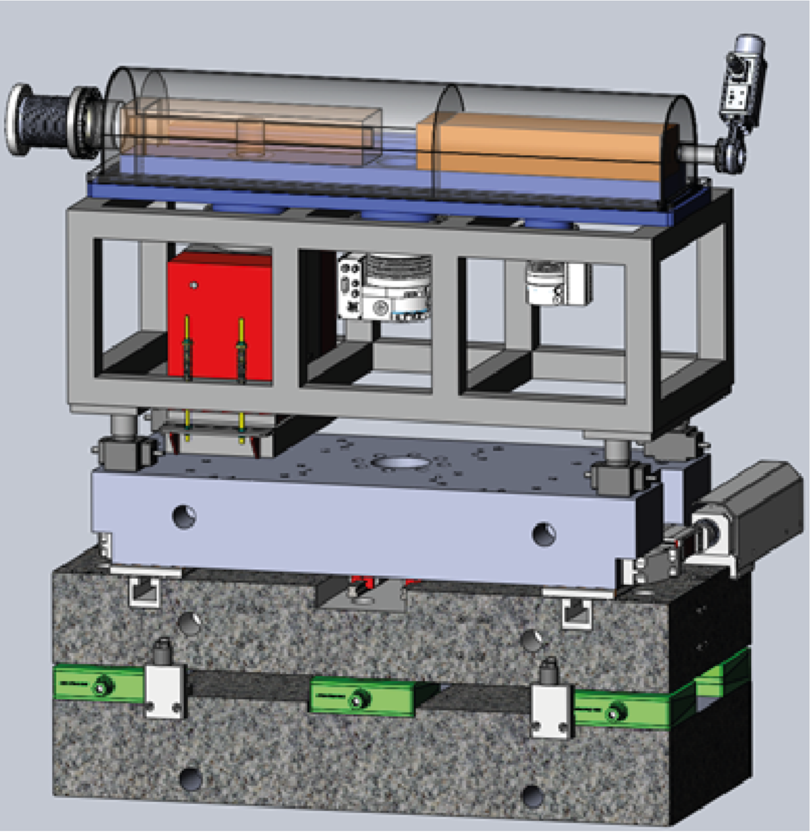

Figure 3.27: Differential pumping section of the MID instrument. The device, consisting of three connected chambers with two turbo pumps and an ion pump, is capable of connecting the multipurpose chamber with a pressure up to 10^{-1} mbar to the UHV part of the beamline (10^{-8} mbar or better). The device is compatible with all possible beam configurations without adjustments. The individual chambers are separated by 40×4 mm^2 (vert. × hor.) B_4C differential pumping apertures allowing the beam to pass.

3.4.3 Experiment chamber

The experiment chamber is the heart of the instrument and will enable a multitude of different scattering experiments. The chamber is conceived as an experiment platform that can host samples and sample environments. It also features tools for alignment of the X-ray beam, the sample, and the optical laser that can be coupled into the chamber and provide a pump pulse. Samples of interest comprise single-crystalline and powder samples, liquid and amorphous structures, and surfaces and interfaces. The chamber will allow operation of sample environments like furnaces, cryostats, and liquid injectors, and provide the possibility of operating ancillary focusing optics with short focal length. The chamber will be optimized in terms of vibrational stability and allow both SAXS and WAXS experiments in transmission or reflection geometry. Section 7.1, “Experiment chamber”, provides detailed information about the MID sample chamber. The samples in the chamber are located ~ 959.5 m after the source point.

3.4.4 Diagnostics end station

Detailed information about the photon beam parameters of every pulse is essential for proper data analysis. Most of the beam characterization methods are invasive (that is, they block or disturb the beam) and are not suitable for installation upstream of the sample. Therefore, the idea is to set up an in-vacuum diagnostics end station after the experiment chamber. Crucial information for experiments at the MID instrument is the beam intensity and position as well as spectral information with high energy resolution. During WAXS experiments when the detector is out of the way, the diagnostics end station will be connected via a small-diameter tube (CF63) to the sample chamber. When the AGIPD system is in SAXS geometry, the direct beam will be guided through a central hole in the detector via a pipe to reach the diagnostics end station. The same concept with a central hole applies to the CCD detector developed by Lawrence Berkeley National Laboratory (LBNL) in Berkeley, California, which will also be used at the MID instrument.

A beam intensity monitor using a PIN photodiode was developed for the SACLA facility in Japan. A high dynamic range and high precision were obtained by observing scattering from thin diamond films [64].

A position-sensitive intensity monitor for the diagnostics end station can possibly be realized using a thin diamond target surrounded by photodiodes [127]. Depending on the intensity of the beam, the scattered intensity reaching the different diodes can change, and their sum reflects the overall beam intensity. Likewise, the difference in diode readings can be related to horizontal and vertical shifts of the beam. Experience from ESRF in France and also recently from LCLS in California indicate that the calibration of such a device is challenging. Certainly, the existing four-diode beam position monitors need to be further optimized for the European XFEL.

Another idea is to use CVD diamond–based position-sensitive detectors with a diamond-like carbon layer deposited as electrodes [92]. First investigations have been performed aiming at assessing the applicability of such devices to the intense XFEL beam with pulses arriving every 220 ns [30]. Damage to the electrodes is a critical issue, and work will continue with further tests at LCLS.

Different techniques have been proposed to determine the spectral information of single pulses. Bragg reflections from thin bent silicon crystals can provide excellent energy resolution of about 0.2 eV at 8.3 keV, as shown recently at LCLS [139]. At SACLA, a focusing mirror and a flat perfect crystal are employed [136]. A third method is based on the use of a non-invasive grating spectrometer, developed at Paul Scherrer Institut (PSI) in Villigen, Switzerland [59]. All three devices are under discussion, particularly concerning their compatibility with the 4.5 MHz mode of the European XFEL. Recently, another setup using CRLs and a perfect crystal operating in Laue diffraction geometry was proposed [62].

If an analyser crystal is to be employed at MID, the only option is diamond, due to heat load issues. Type IIa diamonds are available on the market in sizes up to about 8×8 mm^2 [107], and they can be braced into larger pieces of CVD diamond to facilitate handling and bending. The crystals will need to be bent in order to match the desired operation range (spectral width) with the specified requirements towards resolution and detector size. An example of the resolutions that can be obtained is shown in Figure 3.28 on the next page. A bending radius of $R = 0.3$ m should be feasible without breaking the crystal if the thickness is about 100 µm [77].

The final beam stop of the beamline needs to be placed in the diagnostics chamber. The design of the beam stop is similar to that of the shutter described earlier in Section 3.1.5, “Beam shutter”. It consists of a combination of a B_4C absorber, a tungsten collimator, and a tungsten shutter. Great care has to be taken not to focus the beam on the beam stop, as even B_4C is subject to ablation under extreme conditions. Possibly, an inclined beam stop should be considered here to spread the beam over a larger surface area. Furthermore, an evacuated metal container can be installed behind this beam stop as a safety device. In case the beam were to burn through, the resulting leak would be detected by a pressure gauge that would trigger an alarm and switch off the beam. It is planned to install this device at the end of the experiment hutch at a distance of ~ 968.5 m from the source, hence marking the end of the MID instrument.

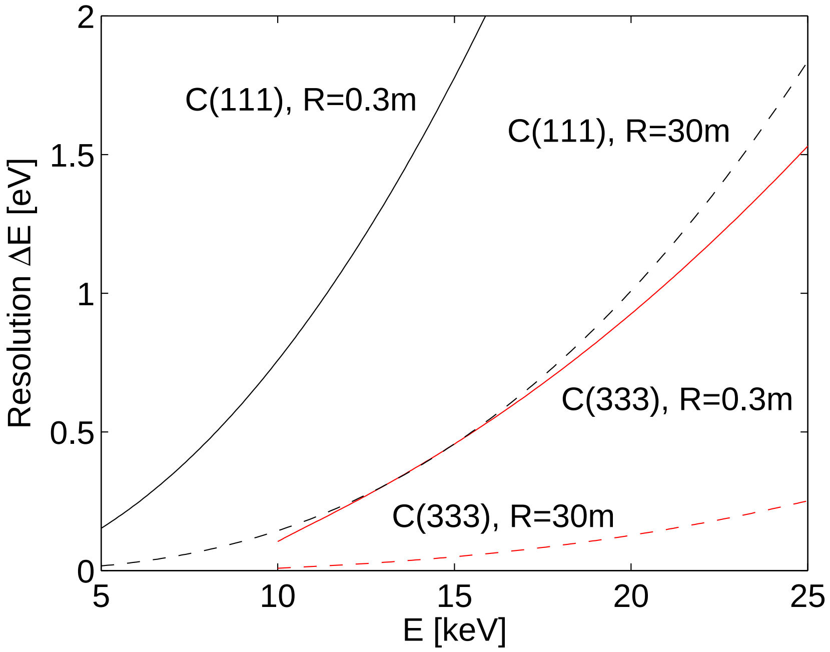

Figure 3.28: Energy resolution of a pixel of the Gotthard detector (50 µm pixels; see Section 8.1.3, “Gotthard 1D detector”) placed 1 m from the crystal. Different crystal reflections and bending radii are shown. The ultimate resolution that can be achieved with a bent-crystal spectrometer is determined by the beam size. Typically, it will be 0.2 eV or smaller and is neglected in this calculation.

3.5 Other premises

In addition to the optics and experiment hutches, the MID instrument comprises a control room, a rack room, and an instrument laser room (Figure 3.29).

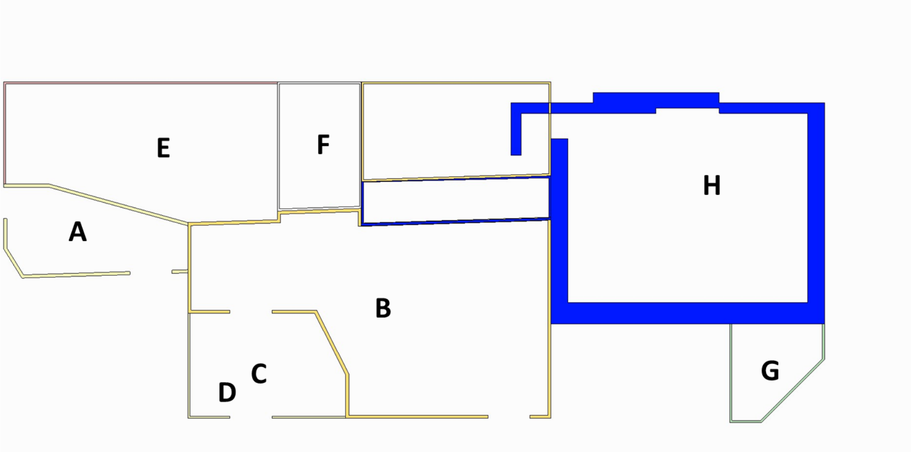

Figure 3.29: Sketch of hutches in the SASE2 area. The MID optics hutch (A) and experiment hutch (B) contain the main X-ray components of the instrument. The experiment hutch is connected to the control cabin (C) via a safety door. The rack room (D) is placed on top of the control cabin and contains the bulk part of motor drives, power supplies, and controllers. The optical laser pulses are generated in the main laser hutch (E) and modified according to the experimental requirements in the instrument laser hutch (F). The optical laser beam is sent directly into the experiment hutch (B) from the instrument laser hutch. A small assembly lab (G) is available to prepare samples and experiments. The experiment hutch of the HED instrument (H) is also shown. The total length of the SASE2 area is about 42 m.

3.5.1 Control room

The control room includes all necessary computing resources to control all motors and devices in the experiment hutch, optics hutch, and tunnel. The control program Karabo, which is being developed by the DAQ and Control Systems group, will enable experiments to be run and data pre-processing to be defined. Pre-selection of acquired frames via a veto system will be available. Furthermore, the control room is furnished with several working places for instrument operators and for users to perform online data analysis. The location of the control room, a proposal for which is shown in Figure 3.29, is still under consideration.

3.5.2 Rack room

The rack room hosts the controllers of the motors and diagnostic tools in the experiment hutch and optics hutch. It contains nine racks with a height of 2.4 m and widths and depths of about 1 m. Since most of the power will be dissipated here, the thermal stability of sensitive areas, like the experiment and optics hutches, will not be disturbed further. The air conditioning will be located on the hutch roof and will cool this room with a constant air flow from the bottom to the top. The cable routing from this room to the instruments in the tunnel, the optics hutch, and the experiment hutch remains to be defined. Alternatively, the rack room can be placed on top of the experiment hutch or on the control hutch.

3.5.3 Optical laser hutches

All beamlines at the European XFEL will have an optical laser that is capable of matching the pulse schemes of the European XFEL. The laser radiation, generated in the hutch of the Optical Lasers group, will have a pulse length between 100 fs and sub-15 fs, a wavelength of 800 nm, and power up to 3 mJ per pulse. To enable optical laser radiation tailored to different requirements, the laser beam will be guided into an instrument laser hutch. Here, various optical parameters, e.g. intensity, energy, beam size, and pulse length, can be modified depending on the experimental needs. The laser hutch is located next to the MID instrument, hence providing the shortest delivery pathway to the benefit of stability and dispersion. In case of extremely dispersion-sensitive beam parameters, the optical laser beam can also be optimized directly in front of the experiment chamber. Here, the timing diagnostics is located to determine the temporal jitter between the arrival of the optical laser and the XFEL beam. Further information about the optical laser system, the modification options, and the available timing techniques can be found in Section 8.2, “Optical lasers”.

3.5.4 Assembly and sample preparation room

In the SASE2 area, a small room is available for assembly of equipment and simple sample preparation and tests. Here, users will have the possibility to carry out preparations and smaller modifications or repair their setups. Workbench and tools will be available. Furthermore, the room can be used as an intermediate storage for equipment during change of experiments. Standard components for operation (vacuum parts, tubes, pipes, and cables) will also be stored here.

4 Thermal impact and damage

To achieve a more detailed technical design of beamline and instruments, it is important to consider whether materials can withstand the XFEL beam and, if so, under which conditions. For this reason, a specialized chapter on thermal impact and damage is included in this report.

4.1 Adiabatic heating

It is instructive to consider a scenario in which all the absorbed photon energy per pulse is transferred into heating of the illuminated volume. Hence, the heat capacity per atom (c_A) of the material and the total absorption cross section per atom (σ_{abs}) determine the heat rise ΔT through the relation

$$\Delta T = \frac{NE\sigma_{abs}}{Ac_A} \tag{4.1}$$

where N is the number of photons per pulse, E is their energy, and A the illuminated area. For a pure material, σ_{abs} is proportional to the linear absorption coefficient μ by

$$\sigma_{abs} = \frac{\mu M}{\rho N_A} \tag{4.2}$$

where ρ is the mass density, N_A is Avogadro's number, and M is the molar mass. Assuming $c_A = 3k_B$ (Dulong–Petit law), ΔT can be calculated. Figure 4.1 on the following page illustrates as solid lines the case $N = 10^{10}$ photons, $A = 1$ mm^2 for beryllium (Be), boron carbide (B_4C), silicon (Si), and tungsten (W). Alternatively, a worst-case scenario can be calculated as shown by the dashed lines in the figure. Here, the fraction of photons absorbed in a slab of material with thickness t (1 µm) is calculated and transferred into a temperature rise by using the specific heat capacities of Be, B_4C, Si, and W in Table 4.1 on the next page. At the MID instrument, we expect on the order of 10^8–10^{12} photons per pulse depending on operation parameters and photon beam energy [75].

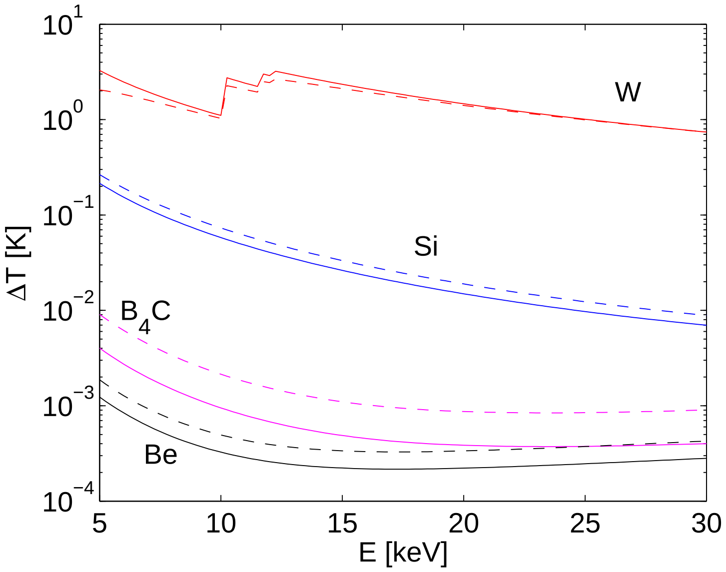

Figure 4.1: Adiabatic heat rise per pulse for Be, B_4C, Si, and W using two different estimations (solid/dashed lines) as described in the text. For simplicity, the calculation assumes 10^{10} photons in a beam area of 1×1 mm^2. A material thickness of $t = 1$ µm is assumed in the worst-case scenario (dashed lines) for comparison. The melting temperatures can be found in Table 4.1.

Table 4.1: Thermal properties of the materials used in the calculations. Values at 300 K are given for the thermal conductivity κ, the thermal diffusivity α, the specific heat capacity c_p, and the mass density ρ. T_m denotes the melting temperature.

Material	**κ [W/(m·K)]**	**α [mm^2/s]**	**c_p [J/(kg·K)]**	**ρ [kg/m^2]**	**T_m [K]**
Be	216	64	1825	1850	1560
B_4C	35	14	1000	2520	2720
Si	149	91	700	2330	1690
W	173	68	133	19 250	3680

From Table 4.1, it appears that Be, B_4C, and Si would all be able to take a full train (2700 pulses) under these conditions without melting (this, however, will not be allowed as the electron beam dump will not allow 2700 pulses/train at a beamline). Increasing the intensity to 10^{12} photons/pulse and 0.1×0.1 mm^2 beam—conditions that mimic the worst case for absorber foils at MID—there is a real risk of melting even B_4C with the pulse train. This emphasizes that beam attenuation by absorber foils should preferably take place where the beam cross section is as large as possible. Silicon is a good absorber material due to its single-crystalline properties, but Table 4.1 on the preceding page shows that great care should be taken. An interesting option might be to incline the Si attenuator slabs in order to increase the beam footprint. We note the excellent thermal properties of Be, and that anything heavier than Si is not desirable as absorber material in the primary beam.

4.2 Thermal conductivity

The ability of materials to conduct heat (thermal conductivity κ) and the speed at which the heat transfer happens (thermal diffusivity $\alpha = \kappa/(\rho c_{\mathrm{p}})$) determines whether considerable cooling of the material can take place between the European XFEL pulses (220 ns), within a train (600 µs), or only in between pulse trains (100 ms). By the flash method, where a sample is given an instantaneous thermal excitation, and the temperature response is measured on a grid established on the sample, the temperature rise time (half time $t_{1/2}$) can be determined. If simple 1D heat transport from the front to the back of the material is dominating, the relation between $t_{1/2}$, α, and the thickness d of the material is

$$t_{1/2} = \frac{5d^2}{36\alpha} \tag{4.3}$$

Hence, from tabulated values of α, one can estimate the thickness of the slab so that half the energy reaches the other side within either 220 ns, 600 µs, or only in between pulse trains (100 ms). This is also an estimate of how far away the heat moves laterally within the time scales characteristic for the European XFEL. The results are shown in Table 4.2 on the following page. The characteristic lengths should be compared with typical beam sizes on the optics. From the table, we conclude that heat transport should be considered only at intra- and inter-train timescales; within 220 ns, the heat simply stays within the size of an illuminated region (larger than 100 µm). While an increase of the peak temperature will happen within a train, Table 4.2 on the next page indicates that the 100 ms lag time between trains is sufficient to ensure efficient heat exchange to an external reservoir (cooling). One take-home message is that, if the material survives one train without melting, it will probably withstand many trains. The approximate temperature rise due to N pulses from a train can then be found from Figure 4.1 on the facing page by adding the corresponding ΔT. Of course, the specific geometry of the material in question needs to be taken into consideration for a more precise thermal modeling. This is attempted in Section 4.4, “Thermal model for Be lenses”.

Table 4.2: Characteristic heat transport distances in µm at the relevant timescales

	Be [µm]	**B_4C [µm]**	**Si [µm]**	**W [µm]**
Bunch [220 ns]	10	5	12	10
Intra train [600 µs]	526	245	628	540
Inter train [100 ms]	6787	3162	8110	6975

4.3 Single-shot ablation

Ablation depends on η, the energy deposited per atom, and 1 eV/atom is often given as the ablation limit [109]. We can estimate η by

$$\eta = \sigma_{\text{abs}} NE/A \tag{4.4}$$

where N is the number of photons per pulse, E is the photon energy, and A is the beam cross section. η is shown in Figure 4.2 on the next page as an example for the four materials considered here. We conclude that, in the case of unfocused beams (1 × 1 mm^2), one is far from the ablation limit for Be, B_4C, and Si, even up to 10^{12} photons/pulse. For tungsten, great care has to be taken and direct exposure to the beam avoided unless it happens under glancing incidence or at moderate flux levels (low bunch charge mode or attenuated beam). The situation changes dramatically if one considers a beam size of 10 × 10 μm^2 and 10^{12} photons/pulse (ordinate of Figure 4.2 on the facing page multiplied by 10^6). Single-shot ablation of W and Si will now take place, while B_4C is also hitting the limit, particularly for photon energies below ~ 10 keV. Only Be seems to be quite ablation-safe also under such challenging conditions. In the case of extreme focusing (1 × 1 μm^2) and extreme flux (10^{12} photons/pulse), all materials will undergo single-shot ablation.

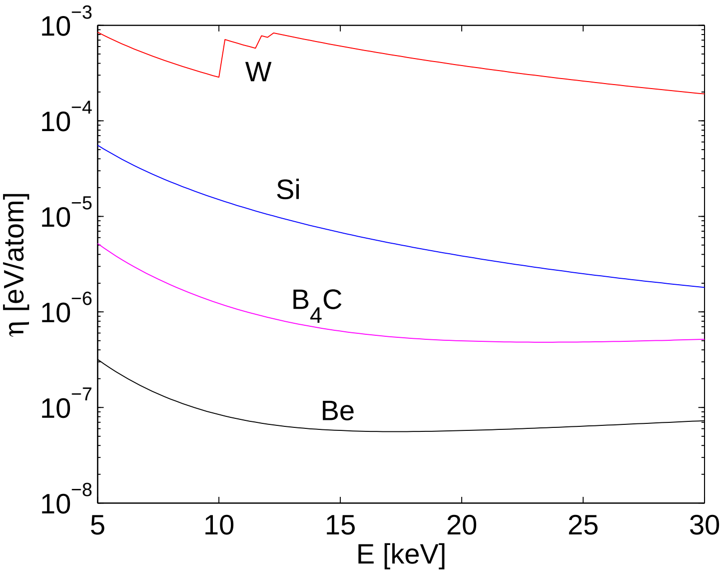

Figure 4.2: Energy deposited per atom in a single shot. For simplicity, the calculation assumes 10^{10} photons in a beam area of $A = 1 \times 1$ mm^2. When scaling to 10^{12} photons in a 10×10 µm^2 beam, the ordinate must be multiplied by 10^6. The single-shot ablation limit is about 1 eV per atom.

Due to its high hardness and stability against ionizing radiation, B_4C is a particularly interesting ceramic material for apertures and coating purposes. In a recent study by Hau-Riege and co-workers [45], the ablation limit of B_4C was experimentally investigated at LCLS with 830 eV photons and found to be close to the melting fluence of 2.7 J/cm^2. The damage mechanism and threshold depends on the photon energy and pulse duration. If a simple scaling according to the photon energy dependence of σ_{abs} is assumed, however, this limit corresponds to $\sim 10^{12}$ photons/pulse at 10 keV in a 10×10 µm^2 beam and is hence very close to an energy of 1 eV deposited per atom for B_4C (Figure 4.2). This observation fits well with earlier UV laser ablation studies, and we conclude that 1 eV is a good estimate of the damage threshold. In some cases, Hau-Riege et al. observed that the multi-exposure damage threshold was a factor of 30 lower than the single-exposure limit. The effect was observed only after 10 000 exposures, and hard X-ray experiments should be undertaken to confirm this result. Nevertheless, it underlines that considerable safety factors need to be included to estimate steady-state operation conditions.

4.4 Thermal model for Be lenses

Consider a 2D parabolic lens made of Be, where the Be thickness follows $h(x,y) = (x^2 + y^2)/R + d$. Here, R is the vertex radius of the lens, and d is the thickness at the vertex point. The maximum thickness of the lens is denoted z and attained at a distance R_0 from the centre, which indicates the boundaries of the Be lens (Figure 5.1 on page 74).

The incident XFEL beam is modeled as a Gaussian envelope with a total integrated number of photons N each of energy E and is assumed to be perfectly aligned with the symmetry axis of the lens. The beam size is modeled according to [109]

$$\mathrm{FWHM}\ [\mathrm{nm}] = 1.2 \times 10^{-5} \cdot (\lambda\ [\mathrm{nm}])^{0.75} \cdot D\ [\mathrm{nm}] \tag{4.5}$$

where D is the distance from the source. Every XFEL pulse that hits the lens is so short in duration that it results in adiabatic heating, but between successive exposures the heat is dissipated and flows according to the heat equation

$$\frac{\partial u}{\partial t} - \alpha \nabla^2 u = 0 \tag{4.6}$$

where α is the thermal diffusivity as introduced earlier and listed in Table 4.1 on page 60. The simulations assume 2D conduction (in the (x,y) plane) and a uniform temperature along the z-direction (lens thickness direction). The simulations assume discrete time steps, and the temperature distribution was found by numerically solving Equation 4.6 for every step. Temperature-induced changes of the thermal conductivity and the specific heat capacity were taken into account by using the dependencies shown in Figure 4.3 on the next page. This may not be entirely correct for the sintered or rolled Be slabs of which the lenses are made, but currently there are no better values in the literature.

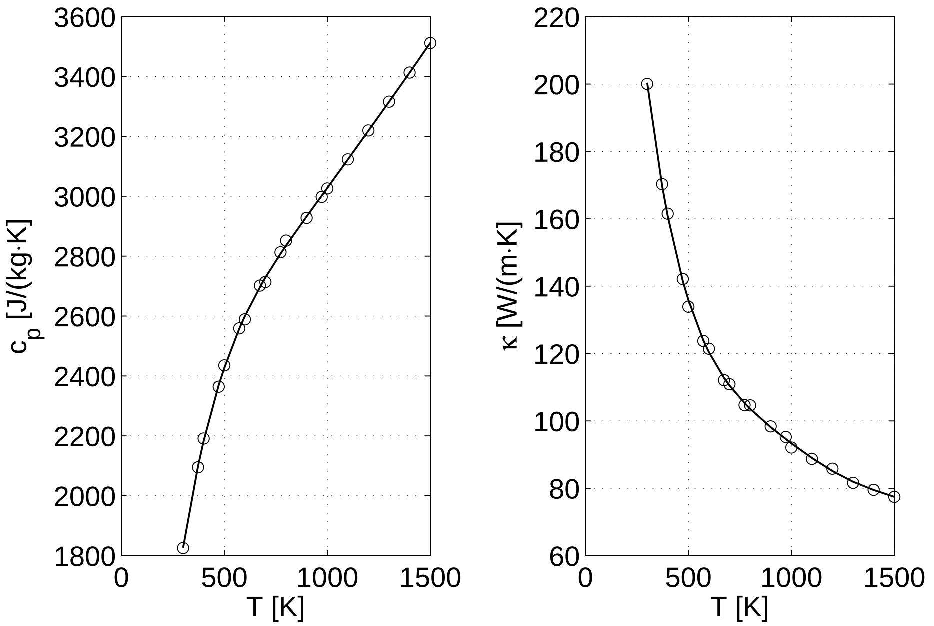

Figure 4.3: Specific heat c_p and thermal conductivity κ of Be as a function of temperature [21; 128]

Figure 4.4 on the following page shows the maximum temperature (T_max) of the lens. 100 pulses per train are used, after which there is a break of about 100 ms before the next pulses arrive. The figure compares two models, one where heat flow during the 100 pulses is taken into account (top), and one simplified version where the 100 pulses heat the Be lens adiabatically (bottom). Very little difference is seen in the behaviour of T_max; the same is true for the overall temperature profile. We conclude that, for 100 pulses/train, thermal conductivity can be neglected during the train. This holds up to about 1000 pulses/train, after which the correction becomes noticeable but is still small. Such a behaviour is expected from Table 4.2 on page 62, as discussed earlier. Both models predict that the 100 ms break between trains is sufficient for the lens to thermalize (300 K assumed to be maintained at the boundaries). The temperature variation over the lens is shown in Figure 4.5 on the following page and Figure 4.6 on page 67 for two cases (marked by arrows in Figure 4.4 on the following page): right after the 100^{th} pulse has arrived and after the intra-train cooling has happened.

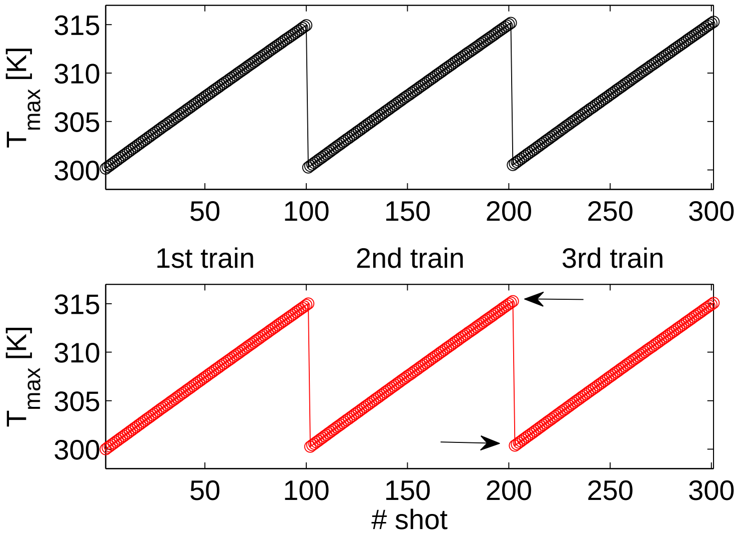

Figure 4.4: Maximum temperature of the Be lens with 100 pulses/train incident beam (10 keV, 10^{12} photons/pulse, z = 1 mm Be thickness, d = 30 µm vertex thickness, R = 5.6 mm). Lens placed at D = 220 m from the source. *Top:* With heat flow between pulses. *Bottom:* Adiabatic heating during the pulse train.

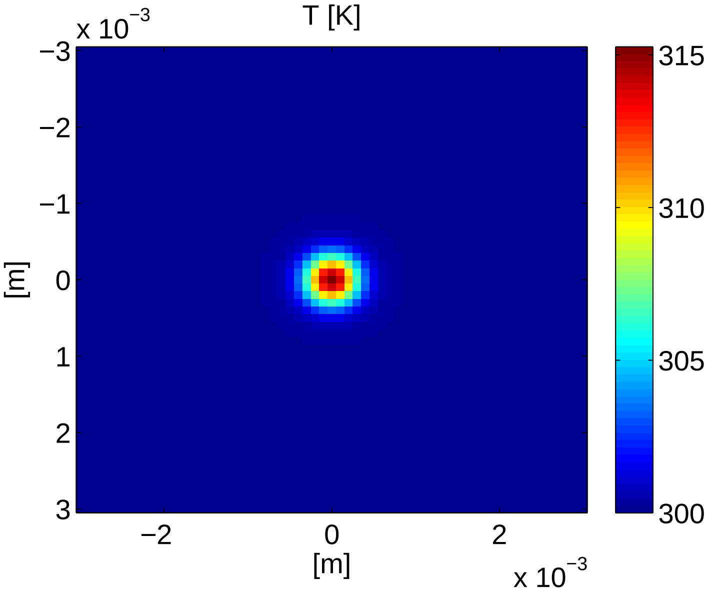

Figure 4.5: Temperature distribution right after Pulse No. 100 of the second train

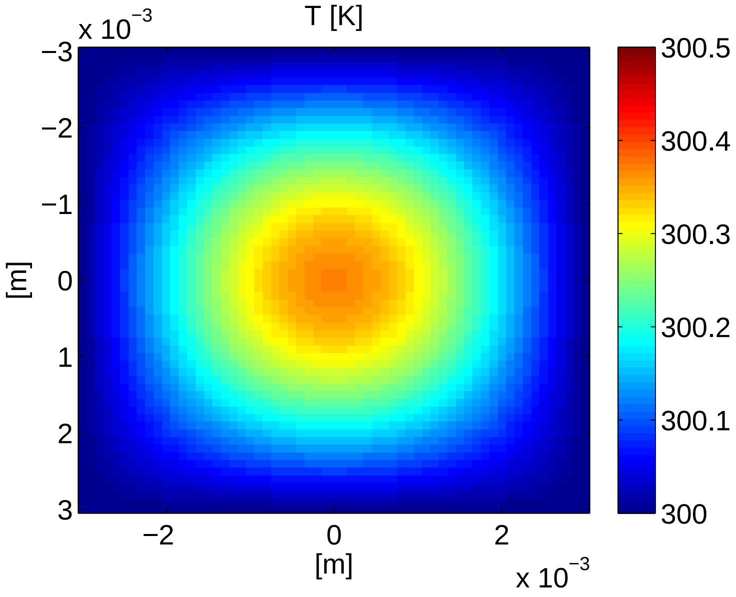

Figure 4.6: Temperature distribution right before Pulse No. 1 of the third train

The temperature behaviour during the cooling phase can be studied further. It appears that, after about 20 ms, a very uniform temperature distribution is reached, and the hot spot has lost 90% of its adiabatic rise during the train (Figure 4.7 on the next page). This time constant is mostly determined by the transport properties of Be and is only weakly dependent on lens shape, thickness, and photon beam parameters (energy, photons/bunch, etc.).

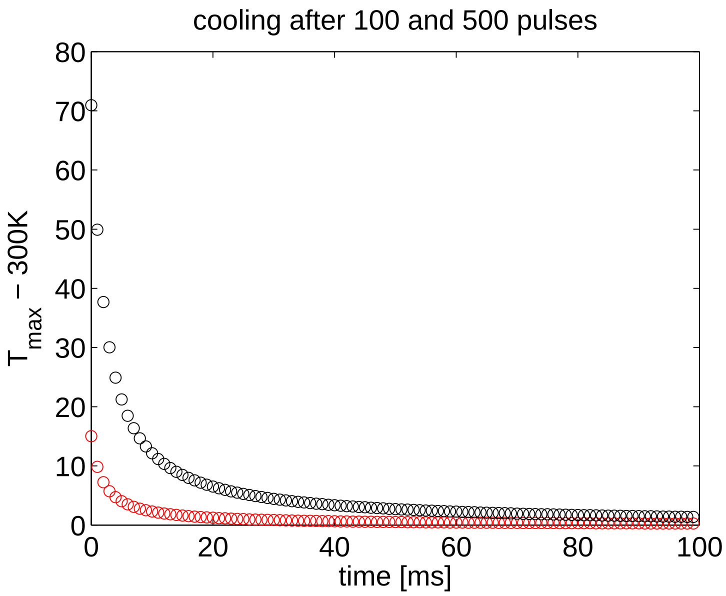

Figure 4.7: Cooling of the lens (*R* = 5.6 mm, *d* = 30 µm) during the 100 ms between pulse trains for 100 (red) and 500 (black) pulses (10^{12} photons/pulse, 10 keV, beam size according to Equation 4.5 on page 64 at *D* = 220 m). After 20 ms, 90% of the initial temperature rise of the hot spot (vertex point) has dissipated.

In the simulations, we find that generally the overall heat load of a lens is reduced as the photon energy is increased. However, above ~ 15 keV, the localized hot spot at the vertex of the parabola increases in temperature. This is caused by the natural divergence of the beam with a FWHM that decreases as the photon energy is increased according to Equation 4.5 on page 64. Some uncertainty, however, remains concerning the beam divergence at high photon energies, so the observed temperature increase might not be relevant at all. The hot spot effect can be reduced by choosing Be lenses with a larger thickness at the vertex point (e.g. 50 µm instead of the 30 µm used in the simulations here) without really affecting the performance of the lenses at high energies. Hence, this could be a viable option for lenses that are meant to focus or collimate the hardest X-rays.

From the simulations, it appears that the temperature of the lenses will vary a lot in the central illuminated region. This area will heat up rapidly during the train (100 pulses take ~ 20 µs) and then cool down again on a time scale of about 20 ms. The temperature rises can be high, maybe more than 70 K in the case of 500 pulses/train (Figure 4.7). While the lens will certainly not be immediately damaged by this, such a repeated temperature cycle may present a problem in the long run. Unfortunately, materials science on pressed, sintered, or rolled

Be foils is not so well developed, and it is difficult, for instance, to find fatigue or temperature cycle studies in the literature. Ultimately, an experiment that reproduces the aforementioned conditions should be undertaken to investigate the long-term behaviour of Be under continuous temperature cycles.

4.5 Thermal model for B_4C

The ceramic material boron carbide is a weakly degenerate semiconductor with transport properties different from those of a metal like Be, as illustrated in Table 4.1 on page 60. The temperature dependence of c_p, α, and κ was studied by Wood et al. [134], and we use their results in the following. Using the same strategy as applied for the thermal modeling of Be lenses outlined above, the temperature rise in a B_4C sheet exposed to the beam 220 m from the source can hence be simulated. This is illustrated in Figure 4.8 on the next page, where 20 trains, each containing 100 pulses (5 or 10 keV, 10^{12} photons/pulse), are impinging on a 1 mm thick B_4C slab. At 10 keV, the attenuation length of B_4C is about 3 mm, so the slab absorbs only 30% of the intensity. At 5 keV, absorption increases to 95% for the same thickness. Due to the poorer conduction properties compared to Be, the 100 ms lag time between trains is not sufficient to remove all the heat deposited by the 100 pulses. However, as Figure 4.8 on the following page illustrates, an equilibrium is reached after a few tens of trains (a few seconds), and the temperature rise is not worrying.

In order to model long-time equilibrium properties, it is important to have a realistic model for the thermal contact between the reservoir and the object that is heated by the beam. The simulations presented here are too simplistic to scrutinize this issue further, but the important message is that the temperature stabilizes fast under idealized conditions. Due to thermal contact resistances and other factors not taken into consideration, the equilibration will be slower in real life, but nothing indicates that there will be a runaway in temperature for unfocused beams.

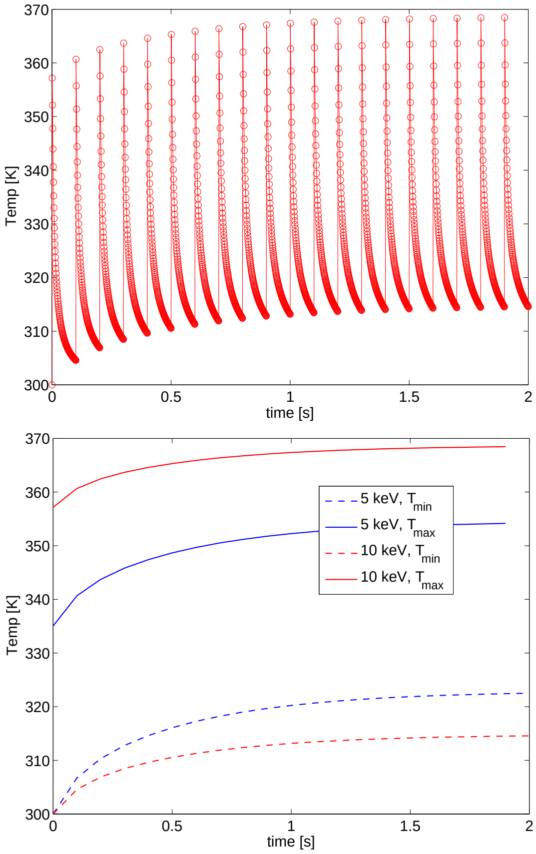

Figure 4.8: *Top:* Temperature of B_4C in the centre of the beam (10 keV, 100 pulses/train, 10^{12} photons/pulse) over 20 trains. *Bottom:* Minimum and maximum temperature obtained in the beam centre over 20 trains.

An important function of B_4C is its usage as protective aperture in front of more sensitive optical components, in particular to protect high-*Z* elements like W slit blades. Tungsten is ideal as aperture material due to its absorption properties, but the single-shot ablation threshold needs to be considered carefully, as illustrated in Figure 4.2 on page 63. Typically, the W blade will intersect the beam in the region of the tail where the flux is lower, but, based on the figure, we still estimate that a safety factor of 10–100 attenuation by B_4C is required before the W slit. Taking 25 keV as the worst-case scenario (20 mm absorption length), 80 mm B_4C before every W blade would give about a factor 50 of attenuation.

4.6 Tungsten slit blades

It is necessary to consider the temperature rise of W when exposed to multibunch trains. Again, the 2D thermal diffusion model described above is used, and the simulations are performed with the usual parameters with temperature-dependent transport coefficients from Lassner and Schubert [67]. Typically, the W slit will be machined as a knife edge to ensure a precise definition of the beam, and be mounted to avoid reflections. In order to mimic this situation, the simulations are performed assuming a very thin W piece (1 µm). With 10^{12} photons/pulse, the edge of the blades would melt with 100 pulses/train for all photon energies, as evident from Figure 4.1 on page 60. The ablation threshold would also be reached as discussed above. Hence, working with high-*Z* materials like W, one is forced to attenuate the beam, and 80 mm B_4C brings us on the safe side up to 25 keV. This is illustrated by the simulations in Figure 4.9, which also highlight the fact that slit blades should never be exposed to the central part of the full beam.

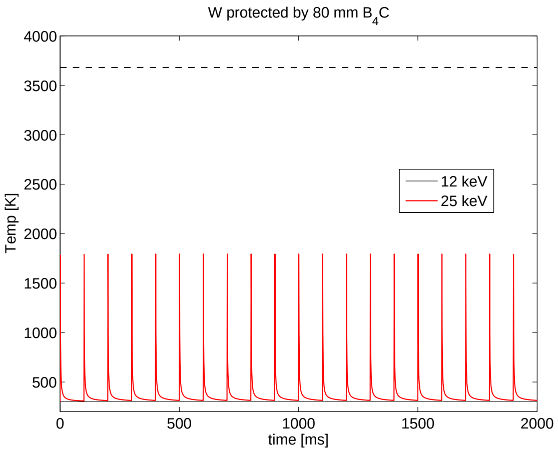

Figure 4.9: Temperature response of a 1 µm thick W edge inserted in a beam of 12 or 25 keV (10^{12} photons/pulse, 100 pulses/train) with the beam sizes expected at 220 m from the source (collimated case). To stay below the melting temperature (dashed line), the beam is attenuated by 80 mm of B_4C, which gives attenuation factors of 1.4×10^{-2} and 1×10^{-7} for 25 keV and 12 keV, respectively.

The slits in the MID beamline will rarely be used to define the beam. This follows from the preceding discussion but also from the wish to avoid fringes propagating with the beam. Nevertheless, protection by B_4C is a safety measure that is definitely needed for all movable parts in high-Z materials that can potentially get close to the beam. A schematic drawing of a slit blade assembly is shown in Figure 4.10.

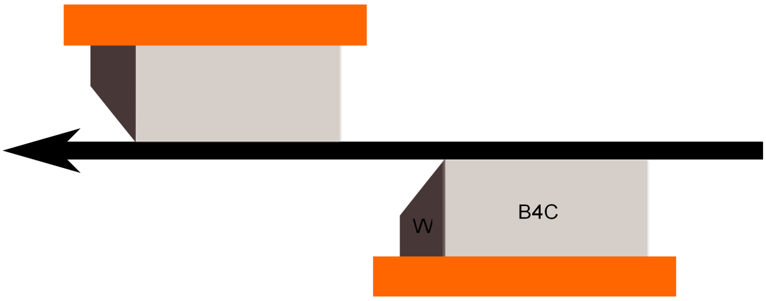

Figure 4.10: Schematic representation of a slit assembly with W–B_4C sandwiches

◦°

5 Beryllium lenses

5.1 Beam size and divergence

The MID experiment hutch is situated about 1 km (sample position: 959 m) after the XFEL source at SASE2. Although the divergence of XFEL radiation is small compared to third-generation synchrotrons, due to the large distances involved, it is desirable to collimate or focus the beam. There are two main motivations behind this wish: to use beamline optics with a reasonably small acceptance and to increase the flux on the sample.

Optics that can be used to change the divergence of an X-ray beam are, for instance, bent mirrors or multilayers, bent or asymmetric cut crystals, zone plates, gratings, and compound refractive lenses (CRLs). The implementation of CRLs needs little space, keeps the optical axis in place (generates no beam offset), and works well in the energy range of the MID instrument, i.e. 5 to 25 keV. Furthermore, CRLs are affordable and easy to align.

Without focusing, an upper limit for the beam size at any location along the MID beamline can be calculated using a conservative approximation for the beam divergence [109, page 26]. This calculation is shown in Section A.1, “Beam size and divergence”. The result is a 7σ beam size ranging from 4 mm (25 keV) to 12 mm (5 keV) close to the sample position.

5.2 Lens formula

In the X-ray regime, the index of refraction n of a material can be written as $n = 1 - \delta - i\beta$, where the correction to the real part of the refractive index, δ, is very small and positive [2]. This makes n slightly smaller than one. Thus, focusing is achieved by a concave lens. Due to the small value of δ, it is often necessary to stack several lenses into a linear array, which explains the name “compound refractive lenses”. The focal distance of a set comprising N lens elements is given by [112]

$$f \approx \frac{R}{2N\delta} \tag{5.1}$$

where R is the lens radius. The correction δ depends strongly on the photon energy. For the energy range covered here, δ is shown in the left panel of Figure 5.1.

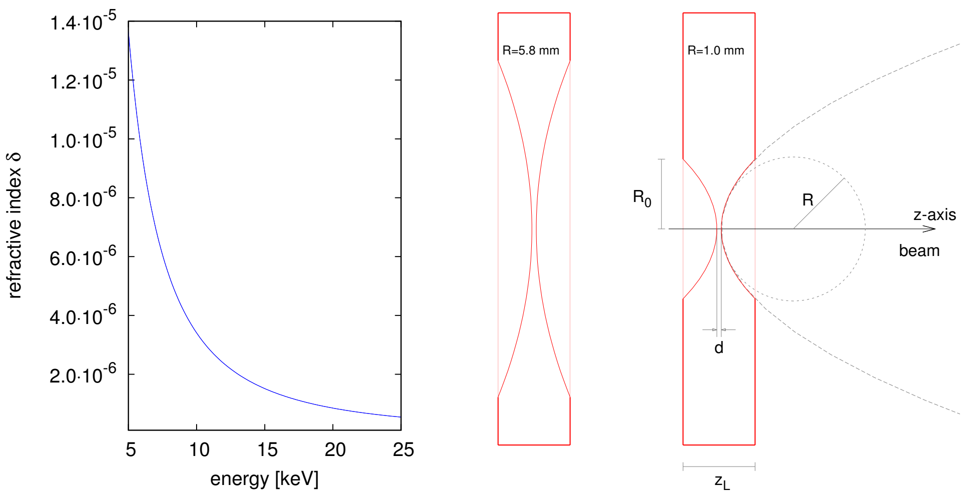

Figure 5.1: *Left:* Correction to the real part of the refractive index, δ, of beryllium. *Right:* Cut through two parabolic 2D lenses with $z_{\mathrm{L}} = 1$ mm and $R = 5.8$ mm or $R = 1$ mm. d is exaggerated for clarity. In reality, d is around 30 µm.

The geometry for a parabolic lens is shown in the right panel of Figure 5.1. The thickness of one lens is given by z_{L}. d is the thickness of the lens at its thinnest point, the vertex. The lens radius R describes the radius of the inscribed circle at the lens vertex. $2R_0$ is the real aperture of the lens, with $R_0 = \sqrt{2R \cdot \frac{1}{2}(z_{\mathrm{L}} - d)}$. If the stack is built up of different individual lens elements of the same material, the focal distance is given by

$$\frac{1}{f} \approx 2\delta \sum_i \frac{N_i}{R_i} \tag{5.2}$$

5.3 Focusing and collimation schemes

Several focusing schemes will be implemented at the MID instrument. They require two CRL transfocator units, which contain mechanical actuators allowing the positioning of any combination of the available lenses into the beam. When inserted, the CRLs must be aligned with respect to the beam axis. The CRL configurations considered in the following are shown in Figure 5.2 on the facing page.

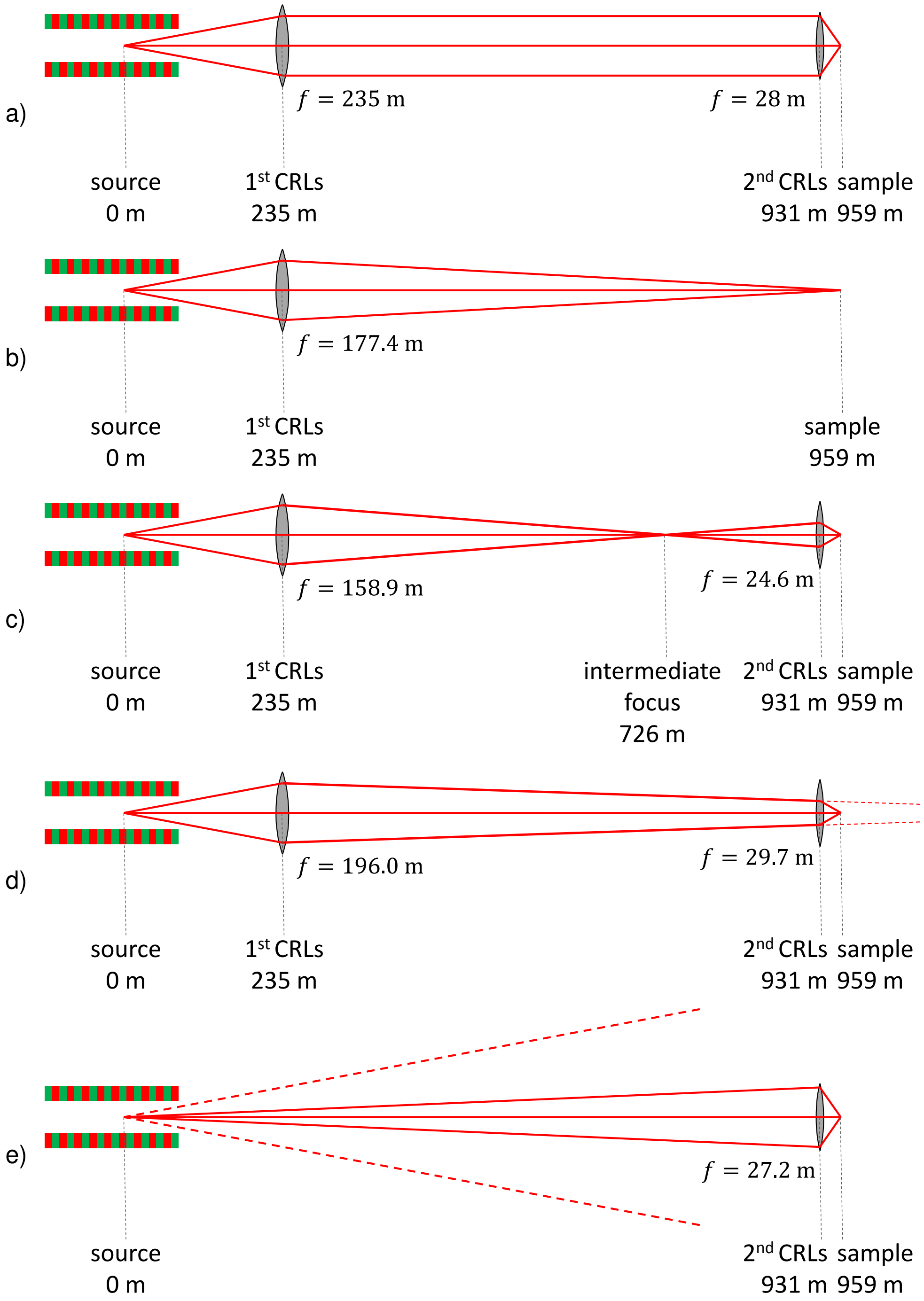

Figure 5.2: Focusing schemes for the MID beamline: (a) *Collimating then focusing* scheme. (b) *Direct focusing* with the first CRL transfocator (CRL-1). (c) Use of an *intermediate focus*. (d) *Combined focusing* scheme. (e) *Brute focusing* using only the second CRL transfocator (CRL-2).

The first CRL transfocator (CRL-1) at 235 m is positioned before the offset mirrors. Using a CRL in that position reduces the beam size on the offset mirror by roughly a factor of 2/3 for the shown schemes. This allows the offset mirrors to transmit 7σ of the beam for all energies between 5 and 25 keV (see Section 3.1.6, "Offset mirrors"). Furthermore, at 235 m, the power density incident onto the CRLs seems to be manageable (see Chapter 4.4, "Thermal model for Be lenses"). The second CRL transfocator (CRL-2) is positioned 931 m after the source, i.e. ~ 28 m upstream of the sample.

Using the collimated beam from CRL-1 without CRL-2 inserted (a configuration not shown in Figure 5.2 on the previous page) already allows us to work with reasonably sized beams. In this configuration, the 7σ beam size is below 2 mm, except for the lowest energy, and even below 1 mm for the higher energies (see Figure A.1 on page 162). Simple collimation using CRL-1 will create the second lowest power densities on the optical elements along the beamline (configuration (e) with the natural divergence is of course lower). It is therefore a relatively low-risk option, yielding beam sizes on the sample that are suitable for some experiments.

When refocusing the collimated beam (the *collimate then focusing* configuration (a) in Figure 5.2 on the previous page), the power densities on all optical elements upstream but also downstream of the CRL-2 stack are small compared to the *direct focusing* (b) or the *intermediate focal spot* (c) options. The main concern with configuration (a) is the effective aperture D_{eff} of CRL-2. CRL-2 typically requires many lenses, which reduces the effective diameter of the lens stack, but the beam size in configuration (a) is larger than in the cases (b)–(d).

In the *direct focusing* scheme (b) where CRL-2 is not employed, the focal spot size on the sample will be bigger than in case (a) and (c). In addition, the power density on major optical elements in the MID optics and experiment hutches will be very high. This configuration can probably only be used with small bunch charges or with the pink beam only (i.e. no monochromators or the split delay line inserted).

Using scheme (c) with an *intermediate focal point* at 726 m allows us to achieve small focal spots while reducing the beam size on CRL-2. This is good for the transmission of CRL-2 but can be critical for the heat load. Still, the power density on monochromators and the split delay line will be less critical than in case (b).

Scheme (d) uses the *combined focusing* effects of the CRL-1 and CRL-2 stacks. CRL-1 is brought to focus the beam, so that the footprint on CRL-2 is identical to case (c).

Finally, we consider the case when only CRL-2 is used, configuration (e). This *brute focusing* scheme is a backup if ablation thresholds or heat load become limiting factors. This scheme delivers the smallest foci on the sample (1–2 µm), but there will be intensity losses due to the large beam size incident on CRL-2.

5.4 Beam sizes at the sample

When focusing a fully coherent beam, the diffraction-limited beam approximately takes the shape of an Airy disc in the focus. According to Abbe, its size b_{foc} is given by

$$b_{\text{foc}} = \frac{\lambda}{2n\sin\alpha} \tag{5.3}$$

where 2α is the angle subtended by the illuminated part of the lens or by its effective aperture (whichever is smaller) as seen from the focal spot.

The effective aperture D_{eff} of the lens stacks is larger than the beam FWHM in most of the cases considered here. The beam FWHM at the CRL-1 stack position is calculated using Equation A.2 on page 159. In cases (b) and (c) in Figure 5.2 on page 75, simple geometrical optics will be used to estimate the beam FWHM at CRL-2. The calculation of focus sizes on the sample is shown in Figure 5.3 on the following page.

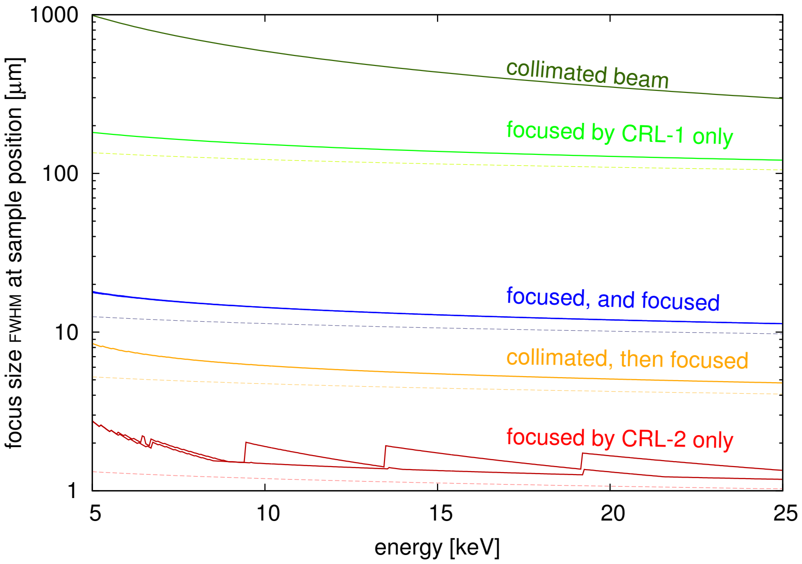

Figure 5.3: Spot sizes (FWHM) at the sample position for the different focusing schemes. The diffraction-limited focal spot sizes are shown as solid lines. The calculation follows Equation 5.3 on the preceding page, where either the beam FWHM or the effective aperture D_{eff} of CRL-2 is used to determine α (whichever is lower). In the case of focusing only with CRL-2, the two red solid lines correspond to the two specific lens sets discussed in Section 5.6, "CRL-2 transfocator at 931 m". The brighter dashed lines are given for reference and show the calculations of spot sizes using geometrical optics with a source size of b_{source} [μm] = $6 \cdot \ln(6 \cdot 10^3 \lambda$ [nm]), [109, p. 27].

5.4.1 Absorption and effective aperture

The imaginary part β of the index of refraction describes absorption in materials. β is small for Be and the X-ray energies used here; it varies between $\beta \approx 1.6 \times 10^{-8}$ at 5 keV and $\beta \approx 1.5 \times 10^{-10}$ at 25 keV. β is related to the linear absorption coefficient μ as

$$\beta = \frac{\lambda}{4\pi}\mu \tag{5.4}$$

and absorption leads to an effective lens diameter of [69]

$$D_{\text{eff}} = 2R_0\sqrt{\frac{1-\exp(-a_p)}{a_p}} \qquad \text{with} \qquad a_p = a\frac{R_0^2}{2R^2} \tag{5.5}$$

for N identical lenses with radius R. a is a fudge factor related to any loss. If we neglect surface roughness of the lenses and only consider absorption, we have $a = \mu N R$. If a combination of lenses with different radii is considered, and if losses due to surface roughness are included, the expression is more complicated. We adapt the approach in Ref. [69] and use

$$D_{\text{eff}} = \sqrt{\frac{4}{C_N, R}\left(1 - \mathrm{e}^{-C_{N,R} R^2_{0,\text{min}}}\right)} \tag{5.6}$$

$$C_{N,R} = \frac{\mu}{2}\sum_{in}\frac{N_i}{R_i} + \sum_{in}\frac{N_i}{R_i}\frac{4\pi^2\delta^2\sigma^2_{\text{rough}}}{R_{\text{average}}\lambda^2} \tag{5.7}$$

Normally, it is possible to realize a desired $\frac{N}{R}$ in more than one way. For example, with the lens radii available, $\frac{N}{R} = 3\ \text{mm}^{-1}$ can be realized as 3 × 1.0 mm, 6 × 2.0 mm, 12 × 4.0 mm, or even 17 × 5.8 mm. By using large-radius lenses, the effective diameter is maximized, and any given N/R can be achieved if enough lenses are used. The only drawback is that N may increase beyond financial and practical possibilities. We estimate that an effective lens diameter of 7σ of the incident beam size is desirable.

Furthermore, it is beneficial to use thicker lens material (thickness z), as this increases $R_0 = \sqrt{r(z-d)}$. A bigger R_0 increases D_{eff} almost linearly, as seen from Equation 5.5 on the preceding page.

5.5 CRL-1 transfocator at 235 m

5.5.1 Weak lenses

CRL-1, which is situated 235 m after the source, is used for collimation and focusing according to the schemes in Figure 5.2 on page 75. The lenses must be very weak as the focal length f varies between 158.9 m and 235 m. $\frac{1}{2\delta(E)f} = \sum_i \frac{N_i}{R_i}$ is the relevant parameter to quantify the required lens strength. It is listed in Table 5.1 for different values of f and different photon energies.

Table 5.1: Required $\frac{1}{2\delta(E)f} = \sum_i \frac{N_i}{R_i}$ for collimation and intermediate focusing by CRL-1 at 235 m. The strongest lens is required at 25 keV in the intermediate focusing scheme, namely $5.763\,\frac{1}{\text{mm}}$. At 4 keV, all focusing schemes require lenses weaker than the $R = 5.8$ mm lens, which is the weakest CRL commercially available.

E	$\delta(E)$	**Collimation** f **= 235 m**	**Direct focusing** f **= 177.4 m**	**Intermediate focus** f **= 158.9 m**
4 keV	2.14×10^{-5}	$0.099\,\frac{1}{\text{mm}}$	$0.132\,\frac{1}{\text{mm}}$	$0.147\,\frac{1}{\text{mm}}$
5 keV	1.37×10^{-5}	$0.155\,\frac{1}{\text{mm}}$	$0.206\,\frac{1}{\text{mm}}$	$0.230\,\frac{1}{\text{mm}}$
6 keV	9.47×10^{-6}	$0.225\,\frac{1}{\text{mm}}$	$0.298\,\frac{1}{\text{mm}}$	$0.332\,\frac{1}{\text{mm}}$
7 keV	6.96×10^{-6}	$0.306\,\frac{1}{\text{mm}}$	$0.405\,\frac{1}{\text{mm}}$	$0.452\,\frac{1}{\text{mm}}$
8 keV	5.26×10^{-6}	$0.404\,\frac{1}{\text{mm}}$	$0.536\,\frac{1}{\text{mm}}$	$0.598\,\frac{1}{\text{mm}}$
25 keV	5.46×10^{-7}	$3.897\,\frac{1}{\text{mm}}$	$5.162\,\frac{1}{\text{mm}}$	$5.763\,\frac{1}{\text{mm}}$

The weakest-focusing Be lenses available from RXOPTICS in Jülich, Germany, have radii of 5.8 mm (also a 5.6 mm variant exists, which we ignore here), 5.0 mm, 4.5 mm, 4.0 mm, and 3.5 mm [101]. The weakest combinations of these lenses are given in Table 5.2 on the facing page.

Table 5.2: Combinations of available weak lenses from RXOPTICS [101]

Lens	1 x 5.8 mm	1 x 5.0 mm	1 x 4.5 mm	1 x 4.0 mm	1 x 3.5 mm	1 x 3.0 mm	2 x 5.8 mm	1 x 5.8 + 1 x 5.0 mm	1 x 5.8 + 1 x 4.5 mm	1 x 2.5 mm	2 x 5.0 mm	1 x 5.8+1 x 4.0 mm	1 x 5.0+1 x 4.5 mm	2 x 4.5 mm
$\sum_i \frac{N_i}{R_i}$	0.172	0.2	0.222	0.25	0.286	0.333	0.345	0.372	0.395	0.4	0.4	0.422	0.422	0.444

The availability of these weak lenses is essential for the performance of CRL-1. Five of the seven weakest lenses of Table 5.2 must be installed in the CRL-1 transfocator to find an ideal energy, i.e. an energy at which perfect focus or perfect collimation is achieved, in intervals of ~ 0.5 keV for energies below 7 keV (Figure 5.4 on page 84). The five weak lenses we have chosen are: 1 × 5.8mm, 1 × 5.0mm, 1 × 4.0mm, 1 × 3.5mm and 2 × 5.8mm.

5.5.2 Total focusing power

As seen in Section 5.3, "Focusing and collimation schemes", the focal lengths for the CRL-1 transfocator will be 235 m, 196.0 m, 177.4 m, or 158.9 m. As the energy range to be covered varies from 5 to 25 keV, for the MID instrument, the focusing power $\frac{1}{2\delta(E)f} = \sum_i \frac{N_i}{R_i}$ has to be varied between $0.155\frac{1}{\text{mm}}$ and $5.763\frac{1}{\text{mm}}$. However, the HED instrument of SASE2 will also need focusing and collimation. As CRL-1 is located upstream of the distribution mirror, it is possible to share this device, which is of course desirable in order to reduce the cost of the instruments. The requirements for the HED instrument are slightly different [85]. In particular, the shortest focal length the HED group wants to realize with CRL-1 is $f = 133$ m up to 25 keV. This translates into a maximum $\sum \frac{N}{R}$ of $6.89\frac{1}{\text{mm}}$.

With the five weak lenses described above, a combined focusing power of $1.253\frac{1}{\text{mm}}$ can be achieved, which still leaves about $5.64\frac{1}{\text{mm}}$ required in CRL-1 to satisfy MID and HED. This remaining focusing power can be achieved by adding three lenses. The strongest lens should contribute half of the total focusing power, around $3.5\frac{1}{\text{mm}}$. The two remaining ones could have focusing strengths around $1.75\frac{1}{\text{mm}}$ and $0.8\frac{1}{\text{mm}}$.

5.5.3 Transmission

The transmission of a CRL stack should be maximized. It is possible to optimize the thickness of the thinnest lens area d and the number of lenses N_i together with their radius R_i. The total thickness of a lens z is also important, as a bigger z will allow focusing of more outer parts of the incoming beam towards the sample. The transmission of the lens system is calculated in the following.

Starting with a normalized Gaussian incoming beam

$$b_{\mathrm{in}}(r,\sigma) = \frac{1}{2\pi\sigma^2} \exp^{-\frac{r^2}{2\sigma^2}} \tag{5.8}$$

the beam intensity (unity) is obtained via integration over r and ϕ as

$$I_{\mathrm{in}} = \int_0^{2\pi} \int_0^{\infty} b_{\mathrm{in}}(r,\sigma)\ r\mathrm{d}r\ \mathrm{d}\phi = 1 \tag{5.9}$$

The total thickness t_{tot} of all lenses that are used in a given focusing scheme at a certain energy can be evaluated up to the aperture of the smallest lens, i.e the lens that has the smallest physical aperture $R_0 = \sqrt{2R(\frac{z}{2} - \frac{d}{2})}$. We find

$$t_{\mathrm{tot}}(r) = \sum_{i\in\mathrm{in}} (N_i d + \frac{N_i}{R_i} r^2) = N_{\mathrm{in}} d + r^2 \sum_{i\in\mathrm{in}} \frac{N_i}{R_i} \tag{5.10}$$

The transmitted intensity is then given by the following integral

$$I_{\mathrm{out}} = \int_0^{2\pi} \int_0^{R_{0,\mathrm{min}}} b_{\mathrm{in}}(r,\sigma)\ \mathrm{e}^{-\mu(E) t_{\mathrm{tot}}(r)}\ r\mathrm{d}r\ \mathrm{d}\phi \tag{5.11}$$

Evaluating this equation and denoting $T = \frac{I_{\mathrm{out}}}{I_{\mathrm{in}}}$ for the transmission, we finally obtain

$$T = \frac{\mathrm{e}^{-\mu(E) N_{\mathrm{in}} d}}{1 + 2\sigma^2 \mu(E) \sum_{\mathrm{in}} \frac{N_i}{R_i}} \left(1 - \mathrm{e}^{-(\frac{1}{2\sigma^2} + \mu(E) \sum_{\mathrm{in}} \frac{N_i}{R_i}) R_{0,\mathrm{min}}^2}\right) \tag{5.12}$$

RXOPTICS delivers lenses of radius $R \geq 2.5$ mm with a total thickness of $z = 0.7$ mm. Lenses with $R \leq 2$ mm can be pressed in $z = 1$ mm thick Be sheets. As will be seen in Section 5.5.4 on the facing page we can build a transfocator CRL-1 in which the transmission is always above ~ 90%.

5.5.4 Proposed configuration of CRL-1

Combining the results of the preceding analysis, a CRL transfocator with eight actuators seems reasonable. Length constrains do not really apply in the tunnel at 235 m, and 1 m is readily available for this device. In order to achieve a large effective aperture, we prefer to use many lenses of large radii for the remaining three lens actuators, as discussed above. A possible solution is thus:

Actuator	1	2	3	4	5	6	7	8
Filled with	1 x 5.8	1 x 5.0	1 x 4.0	1 x 3.5	2 x 5.8	3 x 4.0	7 x 4.0	7 x 2.0
N/R [$\frac{1}{\mathrm{mm}}$]	0.172	0.200	0.25	0.286	0.345	0.75	1.75	3.5

This amounts to 23 lenses in CRL-1 distributed on eight actuators. This transfocator configuration is further detailed in Figure 5.4 on the next page.

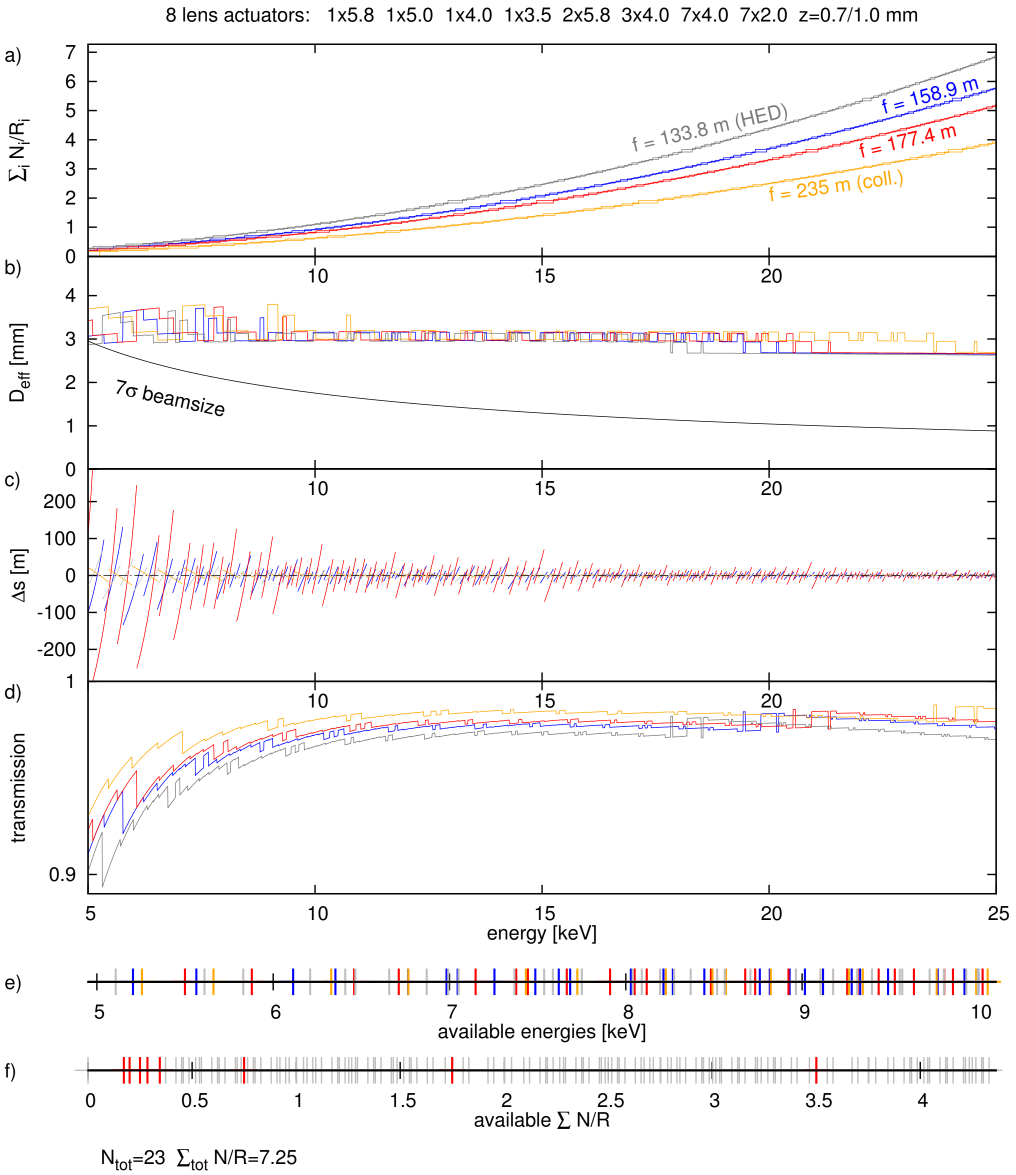

Figure 5.4: Characteristics of the proposed CRL-1 stack: (a) Available $\sum \frac{N}{R}$ to achieve $\frac{1}{2\delta(E)f}$ for collimating (f = 235 m, orange) or focusing the beam in the various schemes discussed. The focusing requirements for HED (f = 133 m) are shown in grey. (b) Effective lens diameter D_{eff} for all situations, showing that D_{eff} is always larger than the 7σ beam size at 235 m. (c) Δs indicates how far the focal spot is away from its target value (source point for the collimating case). $\Delta s = 0$ defines the energies where an ideal lens combination exists with the configuration proposed here for CRL-1. (d) Transmission through the specific lens configuration to be used at a given energy. The expected FWHM of the incoming beam at 235 m is used in the calculation. (e) The axis shows the energy positions of the $\Delta s = 0$ crossings zooming on the 5 to 10 keV range. At the lowest energies, a perfect match exists for every ~ 0.5 keV. (f) The axis shows the $\frac{N}{R}$ of individual lens stacks (eight in total) in red and all the possible combinations in grey.

5.6 CRL-2 transfocator at 931 m

The second lens transfocator CRL-2 must cover focusing needs according to the schemes of Figure 5.2 on page 75. The weakest lens is required for the combined focusing scheme (d) at 5 keV, (f = 29.7 m), the strongest for the direct focusing scheme (c) at 25 keV (f = 24.6 m). This implies that $\frac{1}{2\delta(E)f} = \sum_i \frac{N_i}{R_i}$ will vary from $1.24\frac{1}{\text{mm}}$ up to $37.29\frac{1}{\text{mm}}$, which is a huge range. A possible solution involves again a transfocator with eight actuators (Figure 5.5 on the next page). The proposed lenses in CRL-2 are the following:

Actuator	1	2	3	4	5	6	7	8
Filled with	1 x 5.8	2 x 5.8	3 x 5.0	7 x 5.8	8 x 3.5	5 x 1.0	5 x 0.5	6 x 0.3
N/R [$\frac{1}{\text{mm}}$]	0.172	0.345	0.600	1.21	2.29	5	10	20

Hence, 37 lenses are needed for CRL-2. Figure 5.5 on the following page analyses the lens configuration in a manner similar to CRL-1 in Figure 5.4 on the preceding page, the only difference being that the needs of the HED instrument are no longer considered (CRL-2 is not a shared device).

As seen in Figure 5.5 on the following page, at low energies below 7 keV, an ideal focusing condition is achieved at intervals of about 0.25 keV. This is twice as dense as in the case of CRL-1. This is possible here because the weakest lens available is much weaker than the weakest focusing power required. Removing the weakest actuator of CRL-2 (1 × 5.8 mm) would double the step size between ideal focusing conditions, making the situation similar to CRL-1. However, accounting for possible aberrations and errors in the lens radii, it is probably safer to maintain eight actuators. Figure 5.5 on the next page shows that CRL-2 can also fulfil the requirement of efficiently transmitting 7σ of the beam, except when it is used without CRL-1. The XFEL beam's natural divergence gives a beam size (FWHM) that is larger than D_{eff} of CRL-2, and hence the transmission of the unfocused beam is lower (see panel (d)).

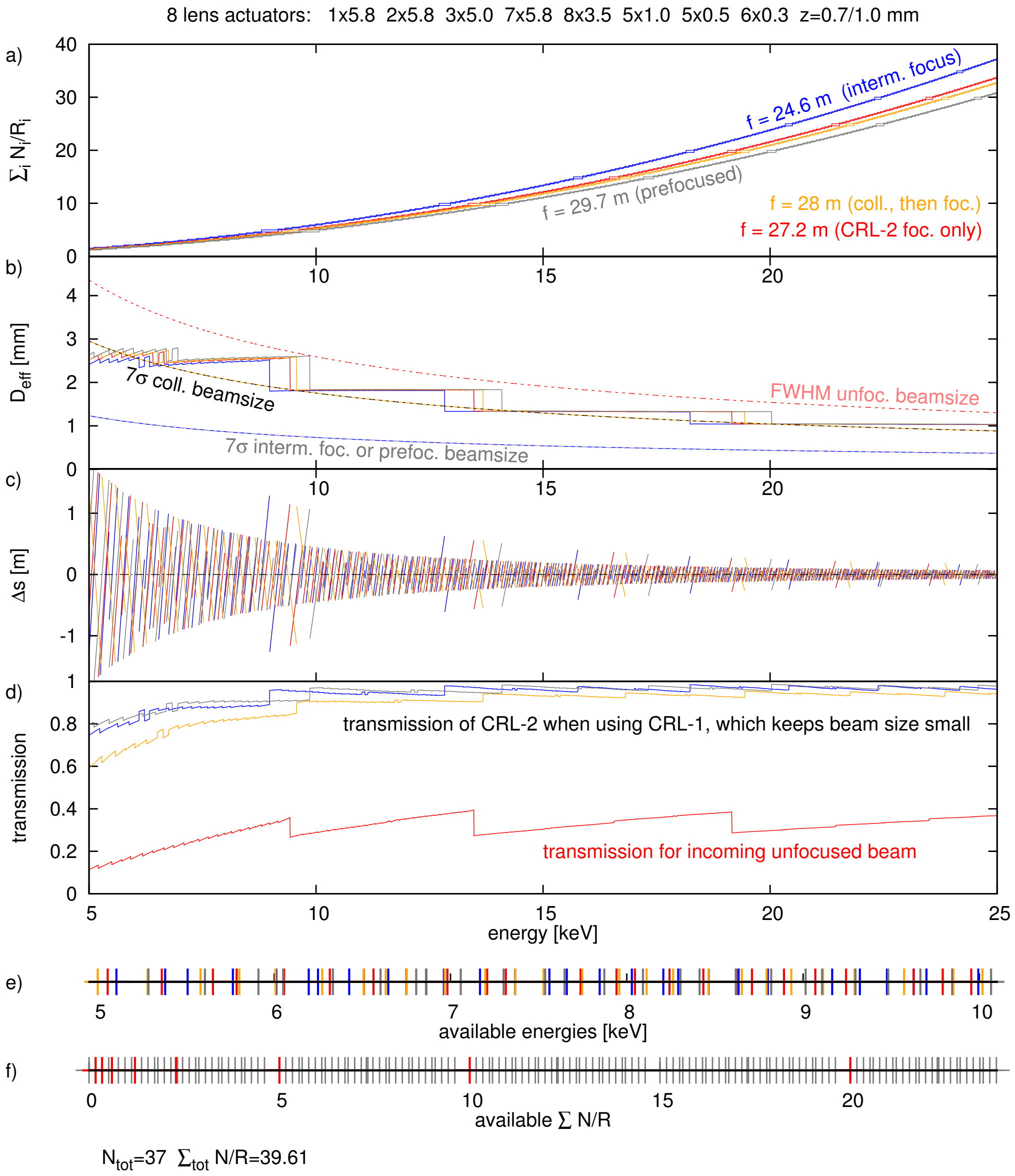

Figure 5.5: Possible configuration of the CRL-2 transfocator at 931 m. CRL-2 uses only 37 lenses, which therefore need to have rather small radii R. Still, the effective aperture D_{eff} is larger than the 7σ size of a collimated or focused incoming beam (see panel (b)).

If we want to increase the effective aperture and the transmission of CRL-2 for the brute focusing scheme, some actuators can be equipped with more lenses of larger radii, especially those with a large $\sum_i \frac{N_i}{R_i}$.

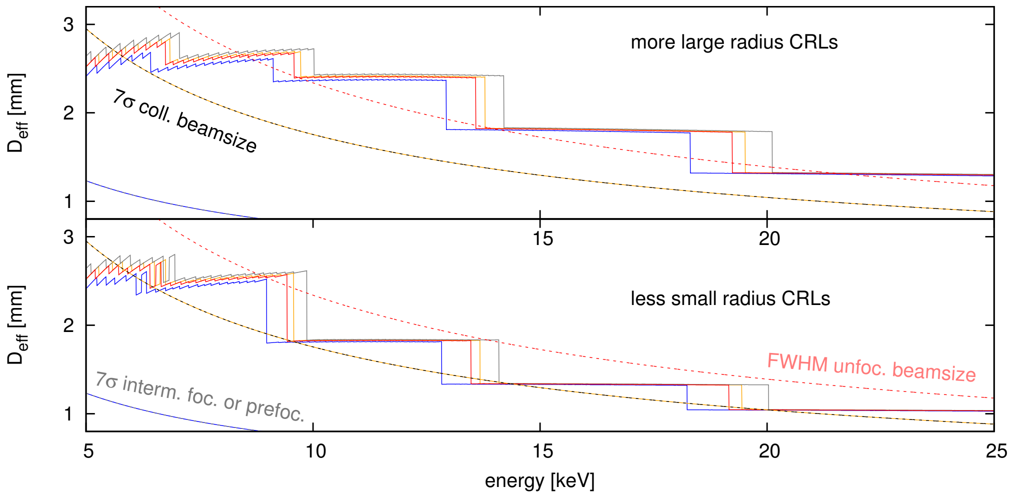

Figure 5.6: Comparison of the effective aperture D_{eff} for two different lens sets proposed for CRL-2. The upper panel uses more lenses (54) with large radii R, the lower panel less lenses (37) with smaller radii. In both cases, D_{eff} is larger than the 7σ beam size of a collimated incoming beam (solid line). For the large-radius solution, D_{eff} is also larger than the FWHM of the unfocused beam at most energies. The inconvenience is more lenses and a higher price.

The new actuator filling would be as follows, with the third and the last four actuators equipped with more lenses:

Actuator	1	2	3	4	5	6	7	8
Filled with	1 x 5.8	2 x 5.8	4 x 5.8	7 x 5.8	10 x 4.0	10 x 2.0	10 x 1.0	10 x 0.5
N/R [$\frac{1}{\mathrm{mm}}$]	0.172	0.345	0.689	1.21	2.5	5	10	20

The new solution requires 54 lenses in total, hence 17 more than the other proposed configuration. The option with 17 extra lenses will be implemented as it increases the efficiency of the *brute focusing* scheme (e) in Figure 5.2 on page 75 at energies above 9 keV. A comparison between the effective radius of the two options is shown in Figure 5.6.

5.7 Total transmission of the two CRL stacks

In Figure 5.7, the total transmission through CRL-1 and CRL-2 is shown for the different focusing schemes. Solid lines indicate the 37-lens configuration of CRL-2, while the dotted lines show the 54-lens case. The red curves represent the transmission in the *brute focusing* scheme (e) in Figure 5.2 on page 75, and the reduction is about a factor of three compared to the other cases (other colours than red). This focusing scheme, which does not use CRL-1, gives the smallest heat load on all optical components and the smallest spot size. Therefore, it must be implemented and hence requires the option with 17 extra lenses.

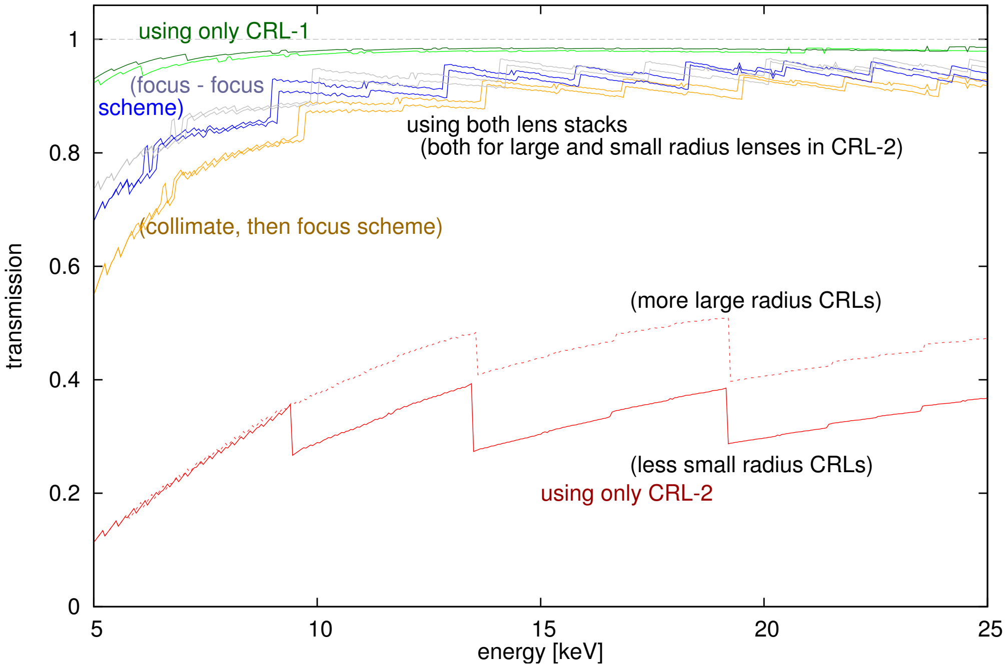

Figure 5.7: Transmission of the different focusing schemes. *Dark green:* Transmission of CRL-1 used to collimate the beam. CRL-2 is not used here, so this scheme gives the highest transmission. *Light green:* Transmission of CRL-1 when focusing directly onto the sample (CRL-2 not used). *Grey:* Transmission when using CRL-1 for prefocusing and CRL-2 for final focusing. The two curves correspond to the two different configurations of CRL-2 that are discussed in the text. *Blue*: Transmission for the intermediate focusing scheme. *Yellow:* Total transmission when CRL-1 collimates and CRL-2 focuses. *Red:* Transmission when using only CRL-2. The dotted lines show the case with 54 Be lenses in CRL-2, while the solid lines are calculated with 37 lenses.

5.8 Stability considerations

The CRL transfocators will need precise alignment and stability in the two directions perpendicular to the beam. This is particularly true for the first lens stack. The optical axis of the MID beamline can be defined as the straight line between the source and the centre of the CRL transfocator lenses at 235 m, and the sample must be positioned in the continuation of that line. If we use the source-magnifying scheme (b) in Figure 5.2 on page 75, the expected focal size is on the order of 100 µm. Allowing the focal spot position to vary by 10% of its size requires a stability of the optical axis at the sample (959 m) to better than 10 µm. At the CRL-1 position at 235 m, this implies a stability and precision of better than $10\ \mu\text{m}\cdot\frac{235\ \text{m}}{959\ \text{m}} = 2.45\ \mu\text{m}$, which is easily within reach. However, if we consider the *intermediate* and the *combined focusing* schemes (labelled (c) and (d) in Figure 5.2 on page 75), both yielding foci on the order of 10 µm, a stability and precision better than $1\ \mu\text{m}\cdot\frac{235\ \text{m}}{959\ \text{m}} = 0.245\ \mu\text{m}$ is needed. Therefore, high-precision mechanics and an excellent thermal stability of the CRL support structures are required. A local enclosure around the CRL mechanics should be envisioned to improve the temperature stability.

The angular alignment of the lenses is much less critical. Any tilt misalignments that keep the centre of the CRL transfocator on the ideal optical axis do not shift the beam downstream. However, when tilting the CRL out of the parallel alignment, more thicker lens parts enter the beam, and the transmission will decrease. This effect will nevertheless be minimal. To align the CRL transfocators, two pinholes at the entrance and exit of the transfocator should be foreseen. These could be realized as narrow apertures on additional actuators that can be removed after the initial alignment. Alternatively, permanently installed larger apertures of 3 mm diameter could be realized with tungsten pinholes protected by thick slabs of B_4C. A diameter of 3 mm would allow 7σ of the beam to pass at 235 m for all energies. The upstream pinhole will permanently protect the Be lens holders from accidental beam movements.

5.9 Beryllium as an optical element

Different Be grades have been investigated using SAXS at ESRF. The results are shown in Section C.1, “SAXS measurements of Be grades”. A Be grade that is as good as the reference material IF-1, but can be obtained in a thickness of 1 mm, was identified.

Wavefront simulations showing the effect of voids in the Be CRLs have been performed and are presented in Section C.2, “Wavefront propagation through Be CRLs”.

6 Split and delay line

Studies of fast dynamics ($t \ll \mu s$) at large momentum transfer q are presently limited to the energy domain (inelastic techniques). XFELs will make it possible for the first time to study fast dynamics in the time domain using correlation spectroscopy. This is particularly interesting for non-equilibrium dynamics, for instance initiated by an optical or X-ray pump. Ultrafast XPCS and pump–probe experiments are enabled by a split and delay line (SDL). SDLs have previously been built and operated with EUV light and soft X-rays [113; 96; 81; 80; 35]. The SDL concept was transferred into the hard X-ray range with a design based on Bragg crystals, and a prototype was built for LCLS [56; 5; 99; 98]. The Japanese XFEL facility SACLA also has an SDL project [126; 135; 88]. This chapter presents the technical design of the MID SDL.

6.1 Placement

The placement of the SDL is governed by two key aspects: 1) it needs to be positioned after a monochromator to reduce the heat load on the first beam splitter crystal, and 2) it should be placed as close as possible to the sample since a long lever arm is unfavourable for beam position stability. This is particularly true for the SDL, as both the pump beam and the probe beam need to overlap at the sample and at the detector for most experiments.

The MID beamline layout incorporating the SDL is shown in a simplified sketch in Figure 6.1. The SDL is positioned at 950.5 m , after CRL-2 and the Si(220) monochromator, which is in line with the arguments above.

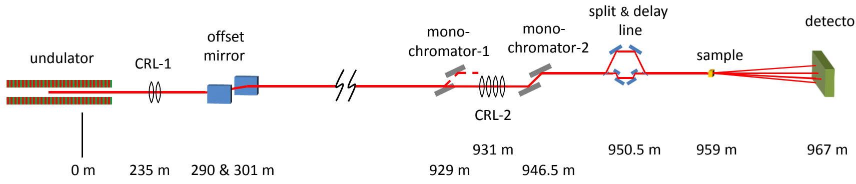

Figure 6.1: Side view of the MID beamline layout as relevant for the split and delay line

6.2 Bragg reflections and beam divergence

The SDL relies on wide-angle Bragg reflections, contrary to grazing-incidence mirrors, to deviate the beam and introduce the necessary path difference $\Delta s = c\Delta t$ in order to delay the pulse. As seen in Section 3.2.2, "Monochromator-1—Si(111)", certain focusing schemes can lead to divergences above the angular acceptance of even low-index Si Bragg reflections. In Figure 6.2, various crystal acceptances and beam divergences are shown in the energy range from 5 to 10 keV. For monochromatic incident radiation, the angular acceptance (Darwin width) of a Bragg reflection is given by

$$\omega = \frac{2\,|\chi_{hr}|}{\sin 2\theta_\mathrm{B}} \qquad \text{with} \qquad \chi_{hr} = \frac{e^2\lambda^2}{\pi m c^2 V} F_{hr} \mathrm{e}^{-M} \tag{6.1}$$

Here, χ_{hr} is the complex polarizability of an ideal crystal [74], V and F_{hr} are the unit cell volume and the scattering amplitude of the whole unit cell, respectively, and $\mathrm{e}^{-M} = \mathrm{e}^{-<qu>}$ is the Debye–Waller factor characterizing the rigidity of the crystal structure. Values of χ_{hr} for a given Si reflection can be obtained from the XOP package [95] or on the web [115]. Typical values for the Darwin width range from about 10 to 60 µrad in the energy range of interest.

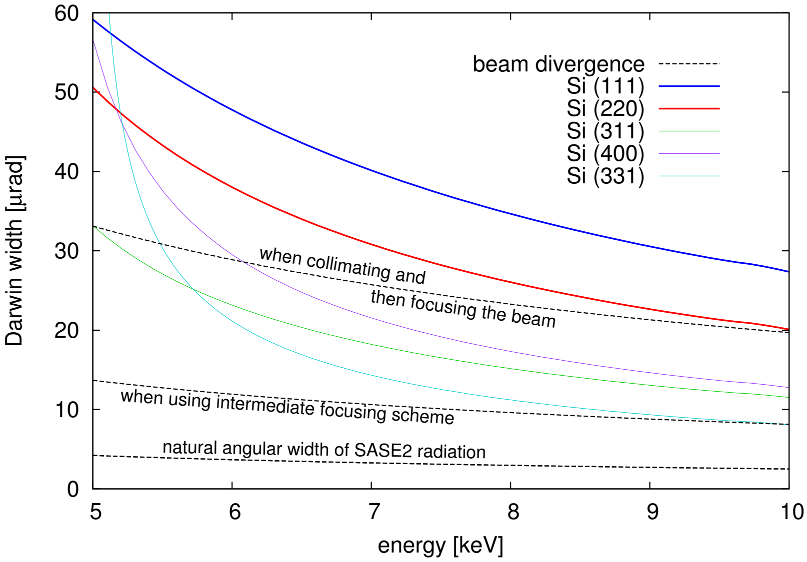

Figure 6.2: Darwin width of various Bragg reflections between 5 and 10 keV. The beam divergence introduced by the various focusing schemes is also shown.

The natural angular divergence of the SASE2 beam is quite small [109, Table 5 on page 22], but the focusing schemes employing CRL-1 and CRL-2 increase the divergence where the delay line is installed. Figure 6.2 on the facing page shows the expected divergence for the focusing schemes (a), (c), and (d) in Figure 5.2 on page 75. These schemes, as well as the use of a collimated beam (CRL-2 out), will be the options with SDL. When only CRL-2 is used to focus (CRL-1 out), the beam divergence will be much too high for the SDL (Figure 3.12 on page 34).

The five Si reflections shown in Figure 6.2 on the preceding page can all be used in the SDL if the focusing schemes are restricted to (c) and (d) in Figure 5.2 on page 75. If the *collimation, then focusing* scheme is requested, it is better to use Si(220) or Si(111) (red and blue curves in Figure 6.2 on the preceding page).

The various focusing schemes have also implications for the size of the SDL crystals. Ideally, all optics at MID should accept 7σ of the beam size. At the SDL, the biggest beam size is found when the collimated beam from CRL-1 is incident (without CRL-2 being used). These maximum beam sizes are $D_{7\sigma}(5\text{ keV}, 235\text{ m}) = 2.7$ mm and $D_{7\sigma}(10\text{ keV}, 235\text{ m}) = 1.6$ mm.

6.3 Stability considerations

The sample chamber is positioned about 7 m after the SDL and the detector approximately another 8 m (variable) downstream. In the range from 5 to 10 keV, the smallest beam size that can be obtained with the focusing schemes compatible with the SDL (see above) is slightly below 10 µm. Therefore, we demand a stability of 1 to 2 µm at a distance of 15 m, which is 10 to 20% of the beam FWHM in focus. This translates to an angular stability of 0.1 µrad. For motorized pitch or Bragg rotation stages, this means that a stability and precision of also 0.1 µrad are required. For the perpendicular direction (horizontal), the constraint is relaxed, as horizontal beam steering via a roll movement is attenuated by a factor of $\sin\theta_B$. If the Si(220) reflection at 5 keV is taken to determine the maximum Bragg angle, we find $\theta_B = 40.22°$ and $\sin 40.22° = 0.64$. In summary, an angular precision and stability of the order of 0.1 µrad in the vertical and 0.2 µrad in the horizontal must be provided.

In the vertical direction (y) and the horizontal direction along the beam (z), a translation of one of the SDL crystals translates into an up or down movement of the beam at the exit of the SDL. At a Bragg angle of 45°, the effect of both critical translations will be equal. At 18.8°, which is the Bragg angle of the Si(220) reflection at 10 keV, a vertical translation of the beam merger crystal by t_y will shift the outgoing beam by

$$\Delta y = 2\cos^2\theta_B \cdot t_y \tag{6.2}$$

as can be shown by simple trigonometry (Figure 6.3). If we require a vertical beam height stability of 1 µm, this translates, at 10 keV for the Si(220) reflection, into a t_y stability of better than 0.56 µm. Consequently, a stability of each crystal and positioning accuracy in the vertical and the in-beam direction of better than 0.5 µm are required.

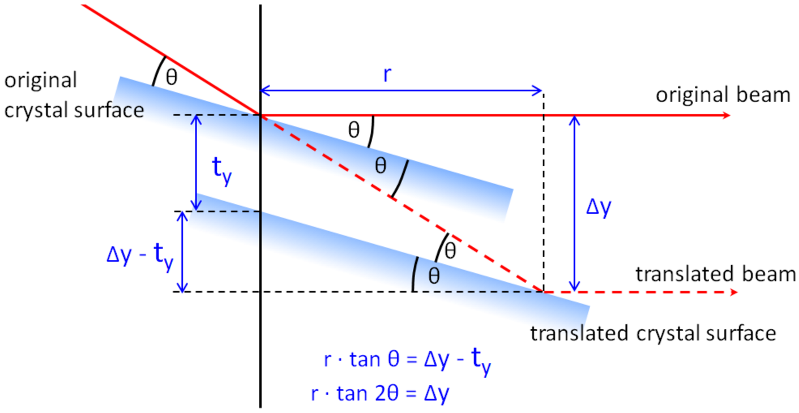

Figure 6.3: Effect of beam merger vertical displacement on exit beam height

We conclude that special attention to temperature stabilization of the SDL is required. Most likely, the SDL will need a proper enclosure in the optics hutch. The entire optics hutch must be stabilized in temperature, preferably to a level better than 0.1 K.

6.4 Geometry

The key SDL design criteria established in the introduction are summarized in Table 6.1. The maximum delay (800 ps) requested is limited by the possibility to fill two single RF buckets of the linear accelerator (two bunches spaced by the RF, 1.3 GHz). While the general repetition rate within a train is 4.5 MHz and not 1.3 GHz, it should nevertheless be possible to have for instance two pulses in the beginning of every train spaced by 800 ps. Hence, we consider that delays from 800 ps and onwards can potentially be generated in the machine, so that we only specify the SDL to operate up to 800 ps. The 5–10 keV operation range comes from geometrical constraints that will become apparent later.

Table 6.1: Main design criteria for developing an SDL for the MID instrument

Energy E	5–10 keV
Delay Δt	0–800 ps
Maximum length L_{max}	1–2 m
Energy bandwidth $\Delta E/E$	$< 1 \times 10^{-4}$

It is important to reach a delay of exactly 0 ps, and even slightly negative delays, in order to determine precisely $\Delta t = 0$. Hence, it is necessary to delay both branches of the SDL, which means that, after the beam splitter, both branches need to be deviated. One branch will be delayed in the $+y$ direction, the other one in the opposite, $-y$, direction. These branches are called the upper and lower branch, respectively. The main delay will be built up in the upper branch, while the lower branch is used only for the extra delay necessary in order to achieve $\Delta t = 0$ ps. The lower branch can conveniently be realized using channel-cut crystals and will provide an excellent stability. The lower branch is not discussed further here.

After the SDL, the beams must recombine and travel collinearly, or at least quite close to each other. In order to reach a net beam offset close to zero, the SDL will be symmetric, achieving half of the delay in the first part and half of the delay in the last part, where the beam is sent back into the initial beam direction. We now focus on the delay achieved in the first half of the upper branch. The geometry is sketched in Figure 6.4 on the following page.

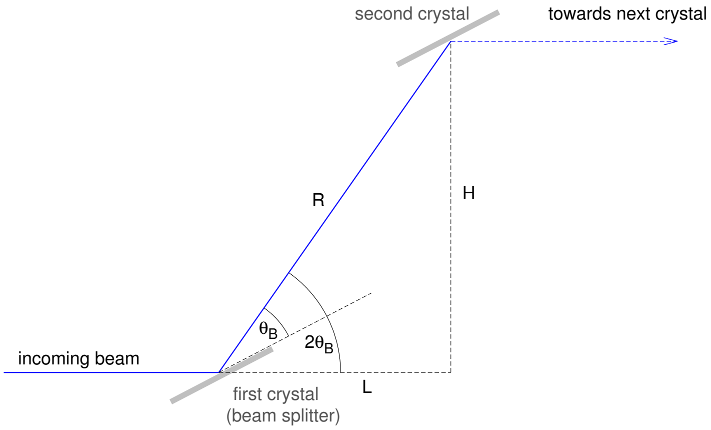

Figure 6.4: Geometry of the first half of the upper delay line branch

The delay acquired in this first half of the upper branch is given by

$$\Delta t_{\frac{1}{2}} = \frac{R - L}{c} \tag{6.3}$$

Using simple trigonometry, it is obvious that

$$R = \frac{1}{2\sin^2\theta_\mathrm{B}} c\,\Delta t_{\frac{1}{2}} \qquad L = \frac{1}{2}\left(\frac{1}{\tan^2\theta_\mathrm{B}} - 1\right) c\,\Delta t_{\frac{1}{2}} \qquad H = \frac{1}{\tan\theta_\mathrm{B}} c\,\Delta t_{\frac{1}{2}} \tag{6.4}$$

Inserting the expression for R into Equation 6.3 and using the expression for H with $\tan\theta_\mathrm{B} = \frac{\sin\theta_\mathrm{B}}{\sqrt{1-\sin^2\theta_\mathrm{B}}}$ yields

$$\frac{c\,\Delta t_{\frac{1}{2}}}{2\sin^2\theta_\mathrm{B}} - L = c\,\Delta t_{\frac{1}{2}} \qquad \text{and} \qquad \sin^2\theta_\mathrm{B} = \frac{\frac{c^2\Delta t^2_{\frac{1}{2}}}{H^2}}{1 + \frac{c^2\Delta t^2_{\frac{1}{2}}}{H^2}} \tag{6.5}$$

Combining the above and solving for H gives

$$H(L) = \sqrt{c\,\Delta t_{\frac{1}{2}}(2L + c\,\Delta t_{\frac{1}{2}})} \tag{6.6}$$

This behaviour is shown in Figure 6.5 on the facing page, which displays the beam path in the full upper branch as a function of the selected Si reflection for both 5 keV and 10 keV with $\Delta t = 2\,dt_{\frac{1}{2}} = 800$ ps.

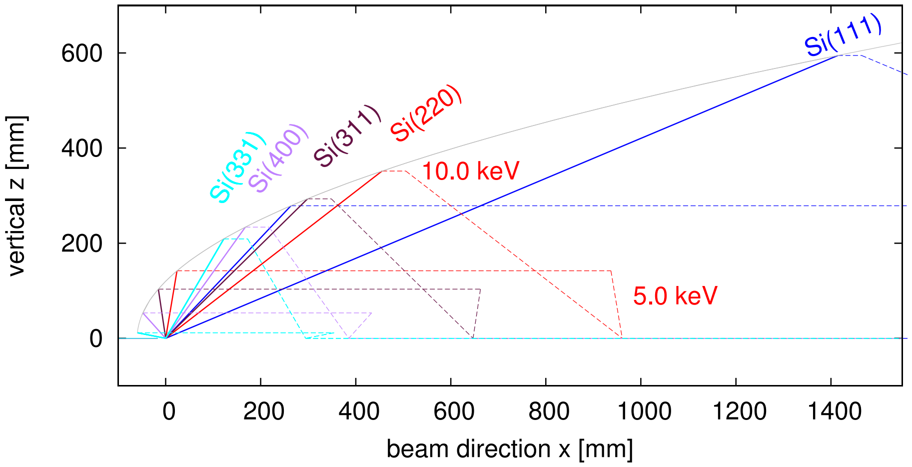

Figure 6.5: Upper branch of the SDL shown for Si reflections (111), (220), (311), (400), and (331), X-ray energies of 5 keV and 10 keV, and a total delay of 800 ps

A 3 m long SDL using Si(111) reflections is not an option due to space constraints. Thus, only the remaining options will be considered. Another conclusion to draw from Figure 6.5 is that the SDL must operate in a vertical scattering geometry. Otherwise, polarization effects become severe and will lead to attenuation of the transmitted beam.

6.5 Energy acceptance

The energy acceptance of a Bragg reflection is given by

$$\frac{\Delta E}{E} = \cot \theta_B \sqrt{\omega^2 + \Delta\theta_{\text{beam}}^2} \qquad (6.7)$$

where $\Delta\theta_{\text{beam}}$ is the divergence of the incoming X-rays. If we consider a collimated incident beam, $\Delta\theta_{\text{beam}} = 0$, the energy bandwidth is shown in Table 6.2.

Table 6.2: Energy bandwidth of several Si reflection at 5 keV and 10 keV

Reflection	$\frac{\Delta E}{E}$ **at 5 keV**	$\frac{\Delta E}{E}$ **at 10 keV**
Si(111)	1.37×10^{-4}	1.36×10^{-4}
Si(220)	5.99×10^{-5}	5.89×10^{-5}
Si(311)	2.86×10^{-5}	2.82×10^{-5}
Si(400)	2.54×10^{-5}	2.49×10^{-5}
Si(331)	1.43×10^{-5}(at 6 keV)	1.41×10^{-5}

As can be seen from Table 6.2, the relative energy bandwidth $\frac{\Delta E}{E}$ depends on the reflection but not really on the energy itself. The energy bandwidth of SASE is around $1\ \times10^{-3}$ but with random spikes that can be two orders of magnitude finer, depending on the length of the pulse. In self-seeded mode, the pulses are Fourier transform–limited, meaning that the bandwidth is inversely proportional to the length of the pulse. As a rule of thumb, 30 fs long Fourier transform–limited pulses have $\Delta E/E \approx 1 \times 10^{-5}$ [54]. Pulses longer than 5 to 10 fs fit well with the Darwin width of Si(220). For shorter pulses, losses can be expected, but this will happen already at the Si(220) pre-monochromator (Mono-2), which is also installed in the optics hutch.

6.6 Beam splitter

The beam splitter thickness is ideal when the transmitted and refracted beams have the same intensity. We will follow the approach from Bartels et al. [10; 9]. The full derivation is given in Appendix B.4, “Absorption, extinction, and reflectivity”. It is based on the atomic scattering factors and the crystalline structure factors, and only the main results will be described here.

If an X-ray beam travels through a thin crystal at Bragg condition, it experiences absorption, transmission, and reflection. The corresponding probabilities P_A, P_T, and P_R can be quantified as a function of crystal thickness [10]. These values are naturally related, and energy conservation implies

$$P_R + P_A + P_T = 1 \tag{6.8}$$

All the values above depend on the choice of Bragg reflection. If the Bragg condition is not fulfilled, the usual exponential attenuation factor P_E will determine the transmission, and

$$P_E = e^{-\frac{\mu t}{\sin\theta}} = e^{-\frac{t}{2t_{\mathrm{abs}}}} \tag{6.9}$$

Obviously, $P_E > P_T$, as P_E does not take the Bragg-reflected intensity into account.

A comparison of the intensities of P_A, P_T, P_R, and P_E is shown in Figure 6.6 on the following page. The calculation in panel (a) assumes the extinction length to be equal to the absorption length (3 µm).

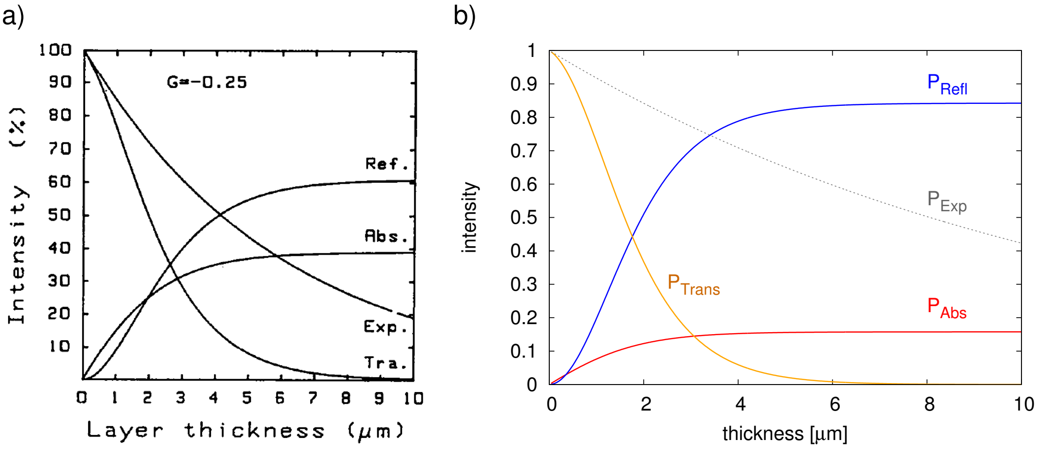

Figure 6.6: (a) Intensities of the different beam components for a beam at Bragg condition in Indium Phosphide, as a function of crystal thickness, taken from [10]. (b) Same calculation for 5 keV for the Si(220) Bragg reflection following [10]. Shown are reflectivity, transmission, and absorption. The exponential transmission function (Equation 6.9 on the preceding page) that applies for angles off the Bragg condition is shown for comparison.

For a perfect 1:1 beam splitter, obviously the Bragg-reflected intensity (proportional to P_R) must be equal to the transmitted intensity. This transmitted intensity will be proportional to P_T for photons inside the energy width of the reflection, but proportional to P_E for photons outside the energy width of the reflection. We thus distinguish two cases: In the first case, the transmitted and reflected beam can be considered to have the same energy distribution, i.e. the incident bandwidth is small. In the second case, the incident beam has a broad energy width. Now the reflected beam is only coming from photons of the right energy, and most of the photons have the wrong energy and travel through the crystal with a probability according to P_E. To determine which situation applies, the bandwidth of the incoming radiation needs to be known.

If the energy bandwidth of the incoming radiation is identical to the Darwin width of the SDL crystals, and if all the crystals are aligned to the peak of the rocking curve, we can calculate the necessary beam splitter thickness for a given reflection and energy by determining the intersection of the blue and orange curves of (b) in Figure 6.6. This has been done for a couple of reflections in Si and C, and is shown in Figure 6.7 on the facing page. Furthermore, for a selected number of conditions, similar results using the transmission and reflectivity of a thin crystal as calculated by XINPRO from the XOP package are shown.

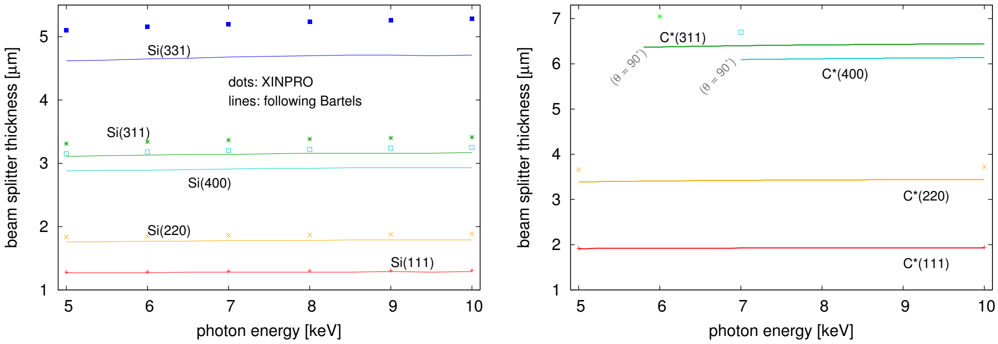

Figure 6.7: Thickness required for the beam splitter and merger. Lines are calculations based on the papers by Bartels et al. [9; 10]; points are results taken from the XOP [95] package XINPRO. In both cases, an incident collimated beam is assumed, with an energy bandwidth equal to or smaller than the width of the examined reflection. For the diamond (311) and (400) reflections, the lower energies are not accessible, as that would require a Bragg angle above 90°.

There is a negligible dependence of the ideal beam splitter thickness on photon energy, which is certainly much smaller than fabrication tolerances. Therefore, the beam splitter crystal can have a uniform thickness. However, a wedge-shaped splitter would be handy and allow for tuning of the splitting ratio.

The required splitter crystals are very thin and will be difficult to mount and operate. If, on the other hand, a slight energy shift (one Darwin width) is allowed between upper and lower branches, it will probably be possible to work with thicker crystals. This can be seen from the intersection of the blue and grey curves of (b) in Figure 6.6 on the preceding page. Now the optimum crystal thickness is about two times larger than the case examined above, where the energy of the two branches is identical. However, the details of the throughput depend on the bandwidth of the incoming radiation and on the crystal arrangement in the two branches. This full derivation of the SDL properties is beyond the scope of this TDR.

Recently, beam splitters have been designed for SDLs at LCLS and SACLA. It is possible to machine thin Si(110) crystals down to 4.4 µm [88; 87]. A sketch of such a splitter thinned down starting from a thick Si frame is shown in Figure 6.8 on the following page. Norcada in Canada is also producing thin crystals—Si(111), Si(110), Si(100)—for beam splitters at the LCLS with thicknesses in the 5 to 20 µm range [83].

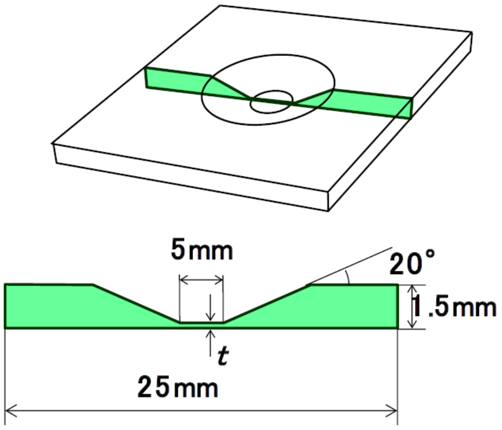

Figure 6.8: Thin Si crystals as prepared by the University of Osaka, taken from [87]

As the crystal thickness can be kept constant for a given reflection over an energy range from 5 to 10 keV, simpler designs using supported Si membranes could be considered for beam splitters. However, the impact of the X-ray pulse might excite vibrations [97] in such free-standing designs. For example, Norcada produces free-standing Si(110) boards of 10 µm thickness, which are attached only on one side [52].

Diamond crystals are superior to Si with respect to thermal properties. The Technological Institute for Superhard and Novel Carbon Materials in Troitsk, Russia [26], is developing thinning procedures for defect-free HPHT IIa diamond sheets [117]. Current state-of-the-art crystals can have thicknesses down to about 25 µm. We will follow this route for beam splitters if the machining capabilities approach 10 µm.

The key issues of any SDL are the beam splitter and beam combiner crystals. Anyone wanting to build a successful device will need to closely follow the developments in thin-crystal optics, and serious investments in R&D will be required.

6.7 Preliminary design

Great care has to be taken in the mechanical design of the SDL. The angular stability of the upper-branch crystals and of the beam splitter and merger is of paramount importance to achieve a precise overlap of the two beams at the sample and to ensure a stable splitting ratio between the two split beams. In addition, changes in Δt should be realized on-the-fly without modifying the angles. This is more than challenging. Any lateral movement of the upper-branch crystals will introduce an angular parasitic motion. Although these parasitic motions might probably be larger than the required angular stability, one workaround will be to use encoders on the lateral translations and a lookup table for angular corrections to be applied at a given position. This relies on the fact that the parasitic angular motion even on long translation stages can be extremely reproducible [11].

It is likely that the device needs to be equipped with online laser interferometry to control the path length difference. Also, the use of invar, inovco, and other materials with low thermal expansion is required whenever possible to relax the requirements on temperature stability.

Different schemes can be considered for the positioning of the upper-branch crystals. These are shown in Figure 6.9 on the next page. Intuitively, scheme (a) is very attractive, as a simple linear motion of an upper-branch crystal on the 2θ translation sets the time delay, requiring only one translation per crystal. However, scheme (b) seems easier to implement but needs the combined motion of two perpendicular translations to set the delay time. Finally, scheme (c) would reduce the amount of long-stroke rotation stages, but the setup becomes more bulky and a huge torque on the main goniometer axes is expected. In addition, it will be less simple to change the illuminated part of the beam splitter independently from the rest of the upper-branch mechanics. We therefore finish with an *artist's* impression of scheme (b) (Figure 6.10 on page 105).

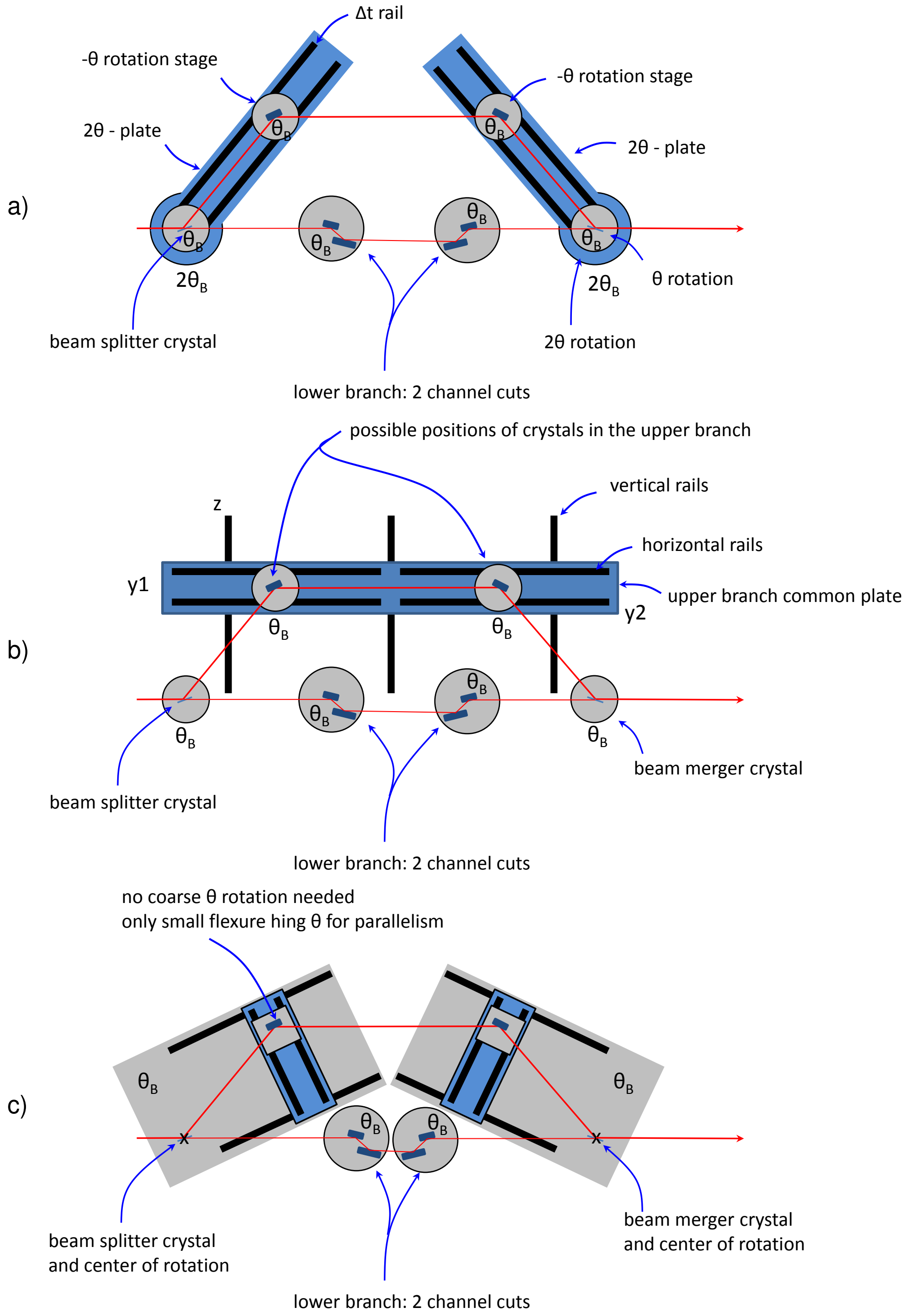

Figure 6.9: Three different ideas how to realize the positioning and angular alignment of the upper-branch crystals. The lower branch is realized using two channel-cut crystals.

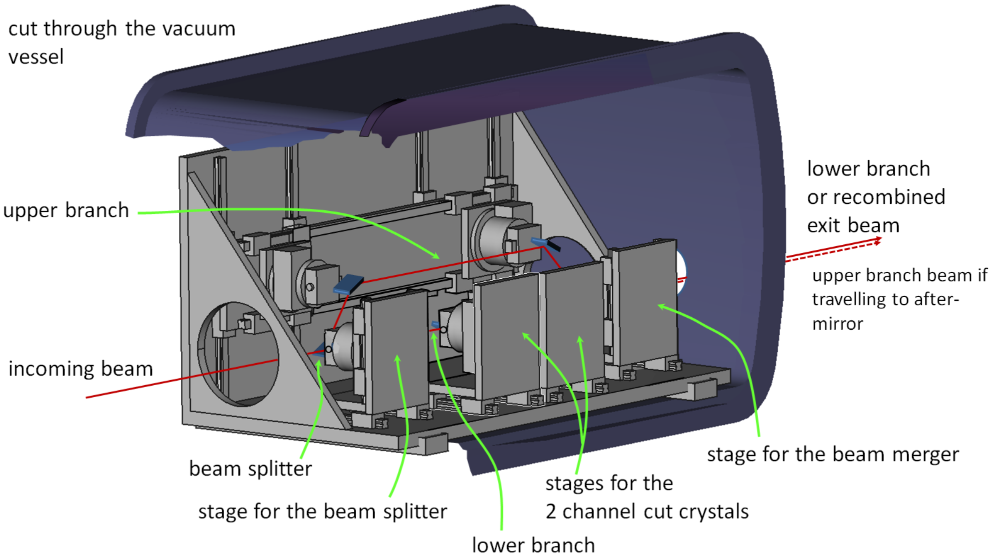

Figure 6.10: Artist's impression of what the SDL could look like, following scheme (b) in Figure 6.9 on the facing page

7 Experiment hutch

The experiment chamber of the MID instrument must be capable of hosting a multitude of different sample environments. The concept of windowless operation implies that the experiment chamber is connected directly to the X-ray delivery pipe via a differential pumping system. The design of the chamber should allow different operation modes and scattering geometries. A short vertical arm will carry the CCD detector developed by LBNL, and a long arm for horizontal wide-angle scattering (WAXS) and small-angle scattering (SAXS) will host the AGIPD. The length of the horizontal arm is modular, providing up to 8 m sample–detector distance. The LBNL CCD can also be placed on this long arm. A heavy-duty beam stop is required at the end of the instrument. It is implemented in a diagnostics end station, which also includes different beam characterization devices to access the energy spectrum and the intensity of individual pulses.

7.1 Experiment chamber

The experiment chamber (Figure 7.1 on the next page) is located ~ 959.5 m after the source point. The XFEL beam height is ~ 1.4 m over the floor. The chamber will be operated under moderate vacuum conditions of ~ 10^{-5}–10^{-1} mbar and be connected via a differential pumping section (for further information, see Section 3.4.2, “Differential pumping section”) to the UHV part of the beamline (~ 10^{-9} mbar). If the samples or sample environment do not tolerate vacuum, the experiment chamber can be separated from the beamline upstream using a transparent diamond window. This operation mode limits the possible beam parameters, e.g. the beam size, repetition rate, and intensity, to ensure that the window does not burst. A safety system with fast valves is envisaged to protect the beamline vacuum against such failures. Moreover, the window will be a source of background scattering and wavefront disturbance at a critical position close to the sample position. This is the reason why windowless operation is given high priority at MID.

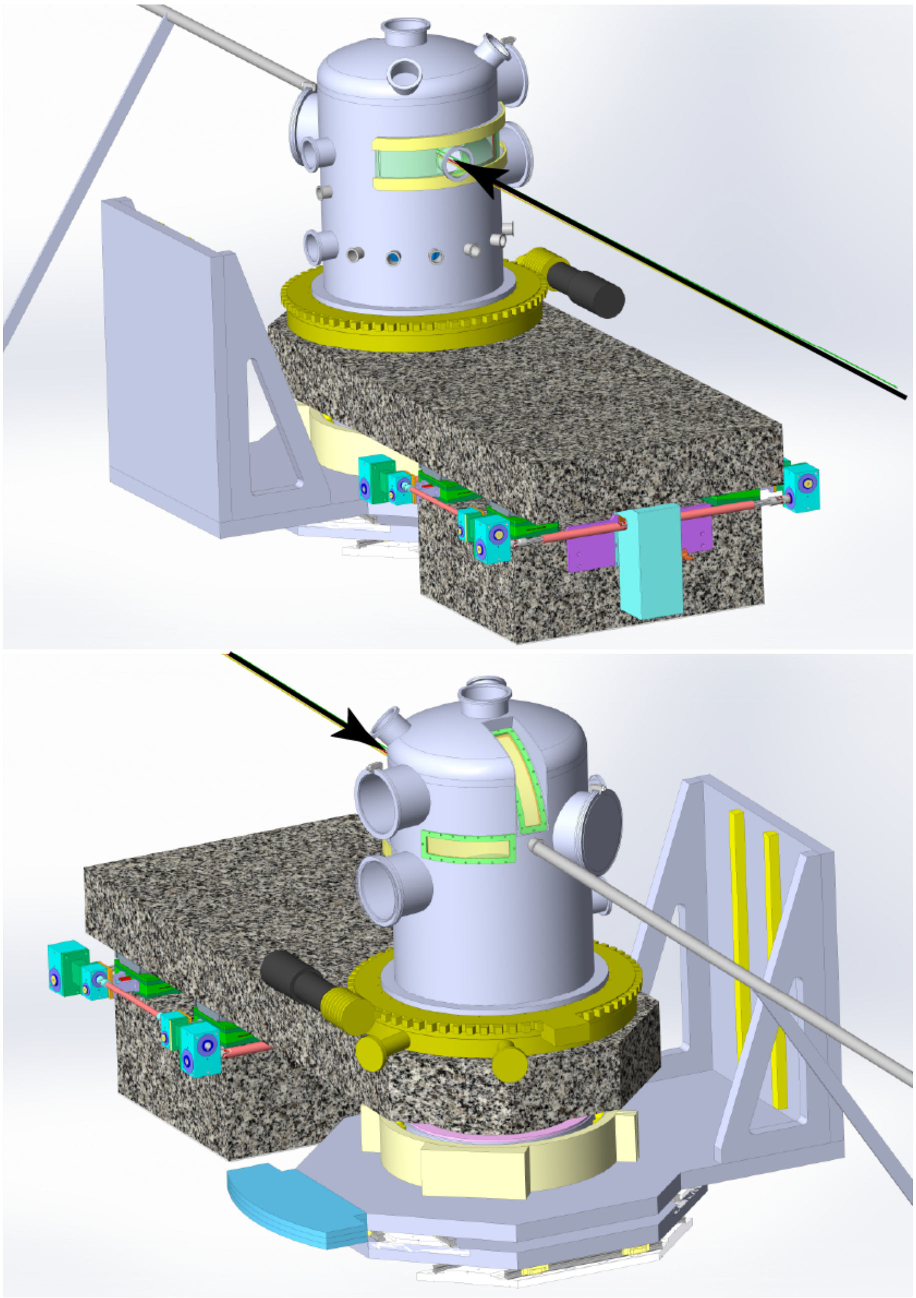

Figure 7.1: 3D drawings of the MID sample chamber. *Top:* The vessel can rotate to allow a fast change between different scattering geometries. A sliding mechanism at the entrance side allows the flange through which the beam enters (shown in green) to be moved. (Further information can be found in Section 7.1.1, “Sliding mechanism”.) On the top of the chamber, a flange is reserved for different liquid-jet injectors. *Bottom:* View of the rear side of the chamber. The chamber is shown in WAXS configuration where the transfer pipe connects to the diagnostics end station and allows characterization of the direct beam. The vessel is turned so the large SAXS flange is on the side. The black arrows denote the incoming beam.

The chamber will be situated on a granite fundament, keeping the external vibrations to an absolute minimum. This granite support also hosts two smaller upstream chambers for optical laser beam diagnostics and nanofocusing optics. Special efforts will be made to reduce vibrations caused by vacuum pumps, motors, and other equipment. Avoiding low-frequency eigenfrequencies of the setup is essential, and stiffness optimizations are ongoing. First simulations indicate that the current design provides very efficient damping of vibrations below 60 Hz and, in particular, there are no eigenfrequencies in this range.

The drawings in Figure 7.2 on the following page provide an overview of the current status of the chamber development. The vessel will have a circular base plate with an inner diameter of 650 mm and a curved top. The height of the vessel is ~ 980 mm and the overall volume is about 0.3 m^3. As described later (see Section 7.1.1, "Sliding mechanism"), the body of the vessel can be rotated, but the equipment inside rests on the granite support and hence remains fixed.

The experiment chamber offers different tools ensuring an easy alignment of the sample in the beam. Two optical microscopes directed towards the sample position allow a rough pre-alignment with a precision of ~ 20 µm. Both microscope are located on the incidence side of the chamber with an angle of 90° between them. This location allows an excellent view of the sample and simplifies its adjustment in the rotation centre and in the beam. Alignment of the spatial overlap between the X-ray beam and the optical laser beam is also facilitated by having powerful microscopes. An avalanche photodiode will be installed at a 90° horizontal angle to detect fluorescence from the sample. This photodiode will enable fine adjustment and calibration of the sample-positioning mechanics inside the chamber. Furthermore, the fluorescence signal can be used to monitor the intensity of the incident beam. Complementary to these tools, an optical alignment laser will be available. This device is coupled into the beam pipe upstream of the experiment hutch, either at the end of the tunnel or in the optics hutch. The alignment laser is adjusted to be collinear with the XFEL beam and hence allows a convenient offline alignment of the instrumentation.

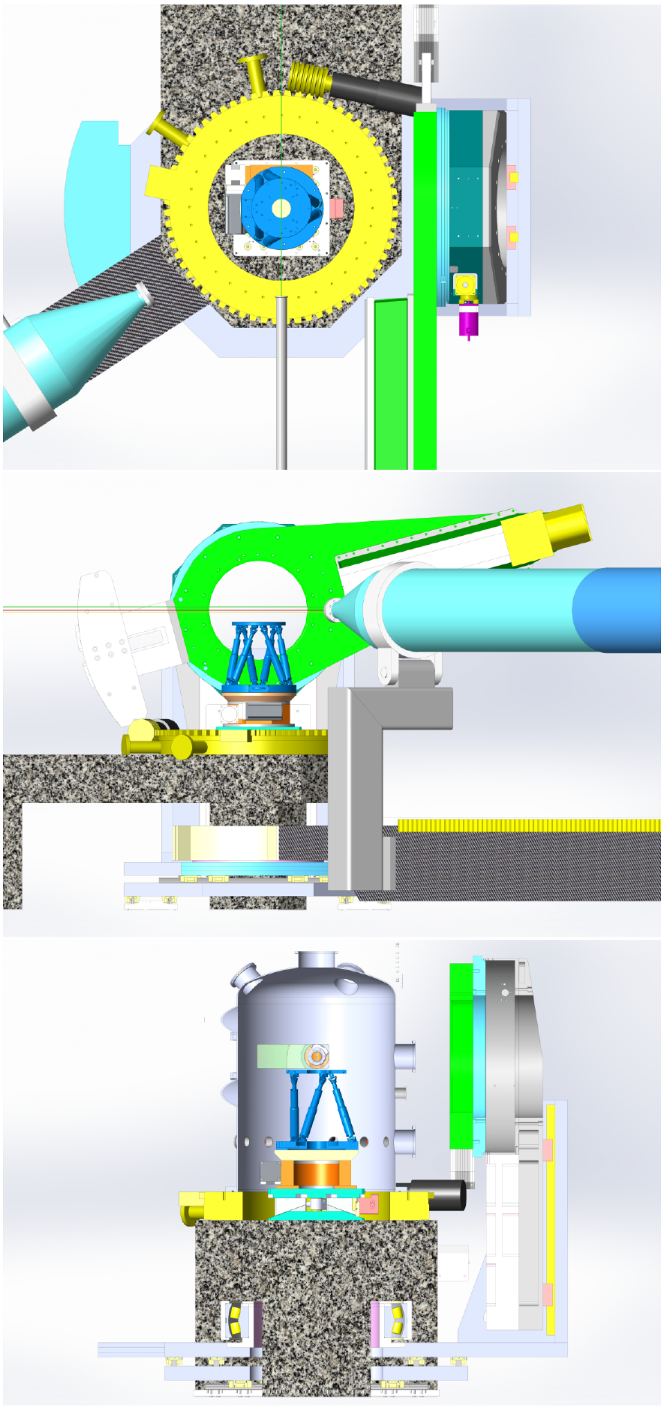

Figure 7.2: Technical drawings of the MID sample chamber, equipped with a hexapod positioning system. *Top:* Top view of the base of the chamber without the vessel. The base plate of the chamber is connected to the granite support and separated from the rotation mechanism of the vessel (yellow). *Middle:* Side view of the experiment setup without the vessel. Inside the vessel, a hexapod on a rotation stage is installed, but a classical goniometer can be used instead. *Bottom:* View of the inside of the vessel as seen from the exit side. The vertical scattering arm hosting the CCD is shown in green.

As mentioned above, the experiment chamber will be equipped with a sliding mechanism for the entrance flange (DN100 CF), allowing the chamber to rotate. More information is given in Section 7.1.1, “Sliding mechanism”. It is foreseen to implement a DN250 CF exit flange in the forward direction for SAXS. Here, the AGIPD can either be mounted directly on the chamber or connected via a vacuum pipe. WAXS geometry (vertical and horizontal) is available via Kapton exit windows in the experiment chamber. The windows allow X-ray scattering measurements between 7° and 60° (2θ). For smaller angles, the SAXS geometry must be employed. It is important not to miss any important combinations of q-range, detector resolution, and scattering geometry. Detailed investigations are in progress, but we are confident that the proposed setup gives the necessary degrees of flexibility, particularly because the photon energy is tunable in a wide range and with a dense coverage of ideal energies for beam focusing. Squeezed in between the two WAXS windows, the sample chamber has an exit flange to connect with the diagnostics end station. This constrains the design but is considered a necessary feature of the setup. Further information about the scattering geometries is found in Section 7.2, “Scattering geometries”.

7.1.1 Sliding mechanism

The sliding mechanism of the chamber allows an easy change from WAXS configuration to SAXS configuration, and vice versa. The SAXS–WAXS switching is achieved by rotating the vessel by ~ 35°. Equipment inside the chamber is not connected to the outer vessel, so it remains stable and will not move. The sliding mechanism is shown in Figure 7.3 on the next page. Here, the chamber is oriented in SAXS geometry with the DN250 CF flange in the middle of the direct beam. Turning the chamber counterclockwise, the smaller transfer tube for the direct beam will be aligned instead. The angular movement required is ~ 35°, as shown in Figure 7.3 on the following page. During the rotation, the transfer tube has to be disconnected and the chamber must be vented since the vacuum pressure could cause too high shear forces on the entrance pipe. Ideally, the scattering configuration is not adjusted during a shift (12 h of beam), and the vessel remains at its position (SAXS or WAXS, or the simultaneous SAXS–WAXS configuration). However, the volume of the chamber is small enough that the valve to the differential pumping section can be opened again ca. 15 min after the turbo pump on the experiment chamber has been started. Together with the intervention required on the chamber, it is estimated that it will take about 1 h to change the configuration.

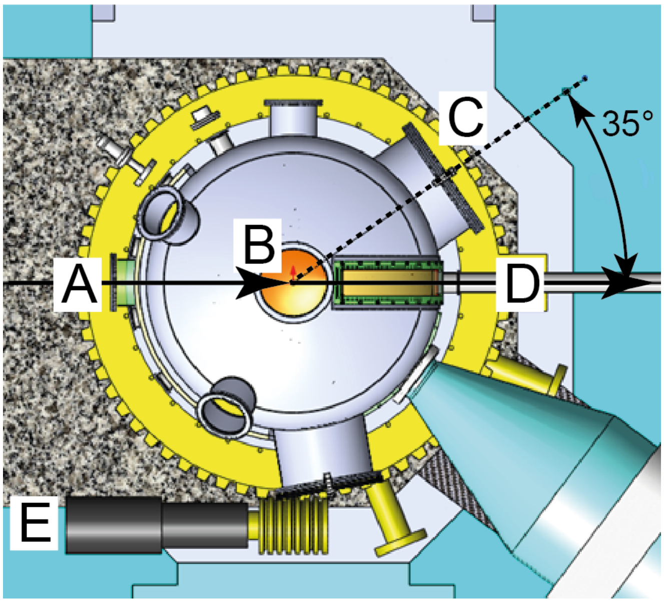

Figure 7.3: Concept of the sliding mechanism of the MID vacuum chamber. Connected to the entrance tube (A) of the beamline, the vacuum vessel can be moved from WAXS (straight line) to SAXS configuration (dashed line) by rotating the vessel around the sample position (B). With this rotation motion, the big SAXS window (C) replaces the smaller transfer tube (D) for the direct beam transfer to the diagnostics end station in WAXS configuration. The angle of this rotation is about 35° and realized using a servomotor (E).

7.2 Scattering geometries

Time-resolved scattering and imaging experiments with coherent X-rays will be the main activities at the MID instrument. The requirements for flexibility are comprehensive due to the multitude of samples and scattering geometries envisaged. Often, a horizontal scattering geometry is suitable, but in some cases a vertical scattering arm is required or of strong benefit. The two-arm solution proposed here also enables simultaneous SAXS–WAXS. The distance between sample and detector must be flexible as, together with the pixel size of the detector, it determines the spatial resolution and q-range of the setup.

The MID instrument features two different detector arms: a short vertical arm and a long horizontal arm, which are described in Section 7.2.1, “Horizontal arm—SAXS and WAXS configuration”, and Section 7.2.2, “Vertical arm”. The two main detectors foreseen at MID (AGIPD and the LBNL CCD) are further described in Section 8.1, “Detectors”.

7.2.1 Horizontal arm—SAXS and WAXS configuration

The option to operate a very long (8 m) horizontal scattering arm is a special feature of the MID instrument. The horizontal arm can move continuously from the small-angle scattering region (Figure 7.4 on the next page) to the wide-angle regime (Figure 7.5 on page 115). Hence, a detector placed on this arm will, together with the previously described sliding mechanism of the chamber, provide an angular range from 0° to 60°. The arm consists of a solid granite fundament with a length of 8 m, holding an evacuated tube to minimize air scattering. A lightweight telescope tube made of a composite material allowing a vacuum of down to 10^{-4} mbar is foreseen and under investigation. A solid detector stand for the AGIPD system is required. It will be equipped with industrial air pads that allow the stand to be lifted several millimetres over the floor. The stand moves along with the rotation of the granite arm but can also slide radially along the granite support to change the sample–detector distance.

The position precision of the detector depends on the flatness of the floor in the hutch. We envisage using the hardened and polished concrete floor of the experiment hall. A flatness of better than 1 mm over 10 m is probably possible. After casting and settling, the height variations of the floor can be mapped out and the necessary corrections directly implemented in the detector movement procedure. Alternatively, a granite floor can be installed for a more precise detector movement. In any case, it is expected that a precision much better than the 200 µm pixel size of the AGIPD system is possible.

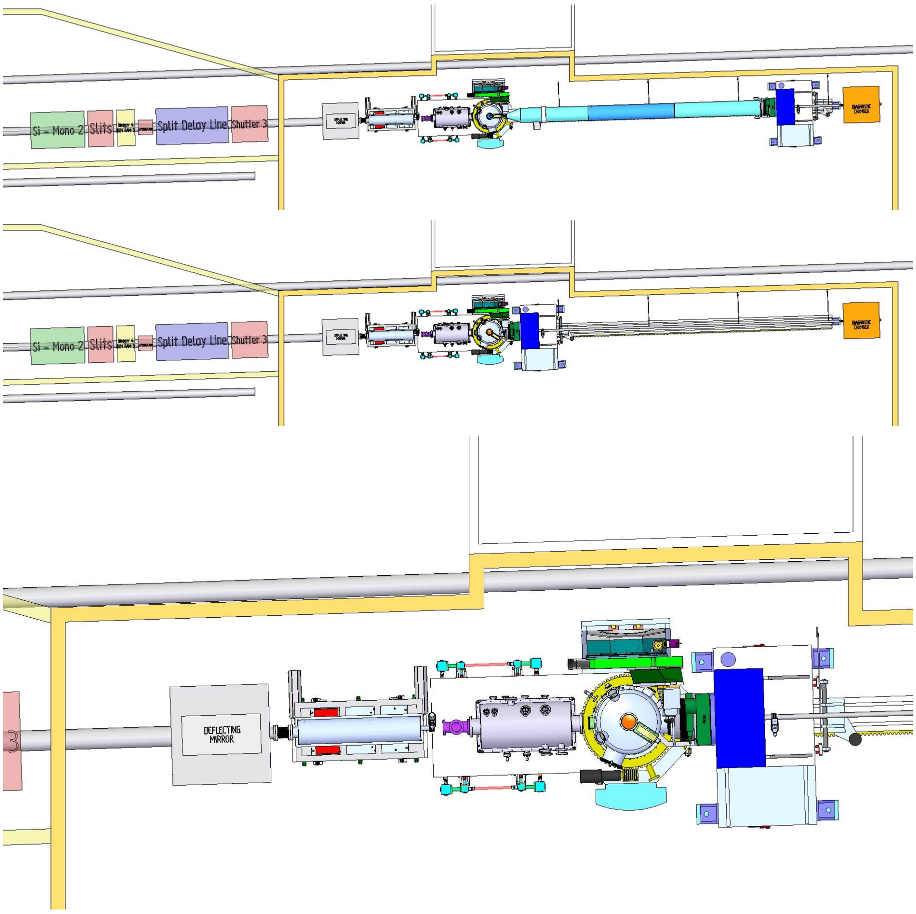

Figure 7.4: Horizontal arm in the SAXS configuration. *Top:* The detector (AGIPD) and the chamber are connected via a telescope pipe. In this way, the distance can easily be changed. In this configuration, an evacuated transfer pipe connects the rear side of the detector to the diagnostics end station. Both the AGIPD and the LBNL CCD have vacuum interfaces that provide this option. *Middle:* The configuration with the smallest sample–detector distance is shown (~ 800 mm). Efforts to reduce this number, approaching 500 mm in the design, are ongoing. *Bottom:* Zoom on the chamber at the smallest sample–detector distance.

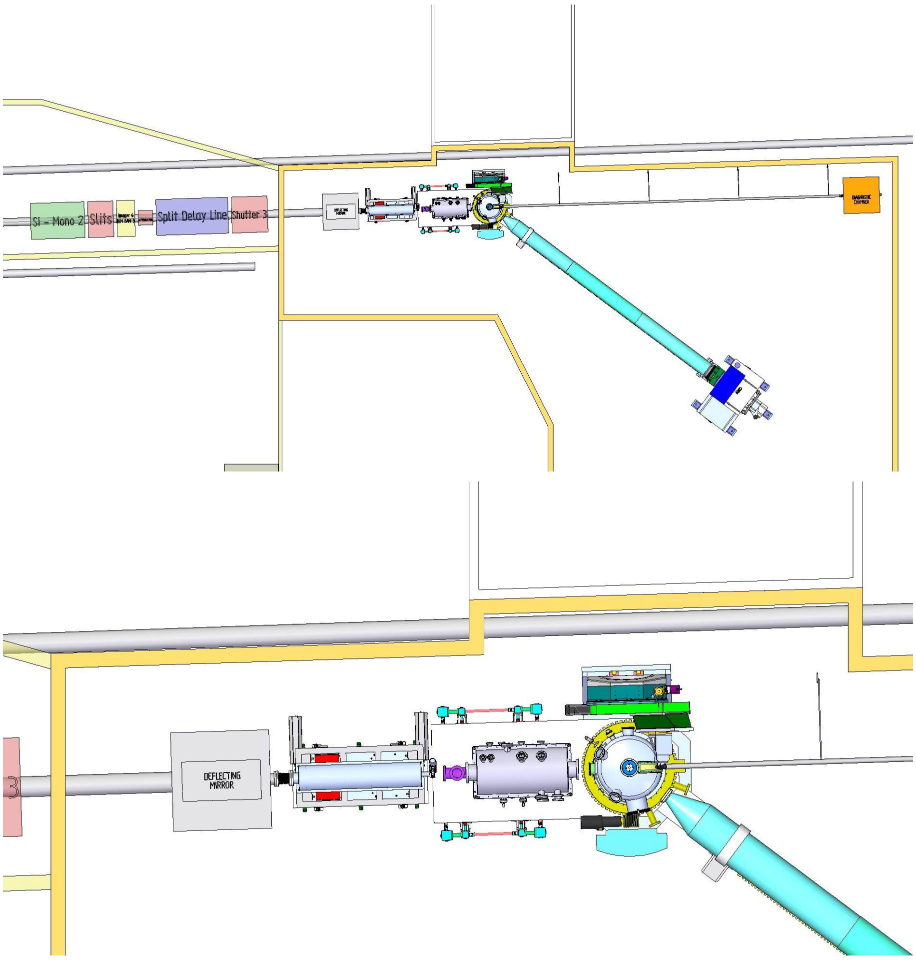

Figure 7.5: *Top:* Long detector arm in the WAXS configuration. In this case, the detector tube is not connected to the vessel, allowing the range from 7° to 60° to be freely scanned. *Bottom:* Zoom on the chamber showing the different arms and pipes in the WAXS configuration.

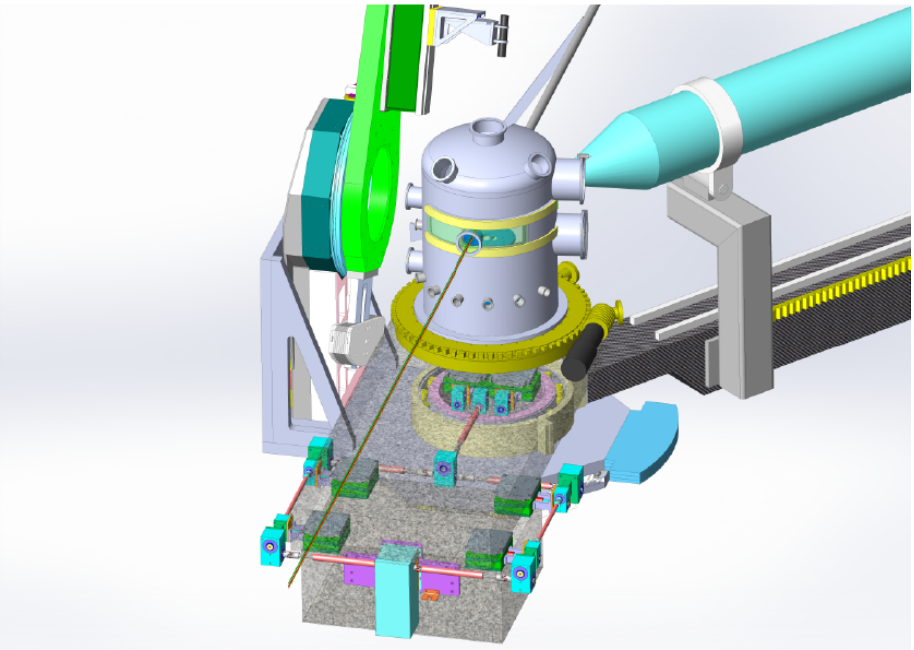

Figure 7.6: View of the sliding mechanics of the chamber and the rotation mechanism of the scattering arm. The motors are implemented in the granite stand of the chamber. For clarity, the granite was set semi-transparent in this technical drawing.

In the SAXS configuration, the tube can be connected directly to the exit of the experiment chamber via a flange. By the sliding mechanism described above, the sample–detector distance can be changed, which again requires a telescope pipe. Depending on the distance to the detector, in SAXS geometry, the connection to the chamber can be via either the small or the large exit flange. Use of the small flange enables the simultaneous use of the vertical scattering arm in WAXS geometry. Table 7.1 on the next page and Table 7.2 on the facing page show the available *q*-ranges at different sample–detector distances with the AGIPD system and the LBNL CCD, respectively.

Table 7.1: Available q-ranges for the SAXS geometry with the AGIPD system: small sample–detector distance of 800 mm, long sample–detector distance of 8 m, and the desired extremely short distance case of 500 mm

XFEL energy	q_{max} at 0.8 m	q_{max} at 8 m	q_{max} at 0.5 m (extreme case)
5 keV	$3.15\ nm^{-1}$	$0.31\ nm^{-1}$	$4.99\ nm^{-1}$
8 keV	$5.04\ nm^{-1}$	$0.50\ nm^{-1}$	$7.99\ nm^{-1}$
12 keV	$7.56\ nm^{-1}$	$0.75\ nm^{-1}$	$11.99\ nm^{-1}$
16 keV	$10.08\ nm^{-1}$	$1.00\ nm^{-1}$	$15.99\ nm^{-1}$
20 keV	$12.59\ nm^{-1}$	$1.26\ nm^{-1}$	$19.99\ nm^{-1}$
25 keV	$15.75\ nm^{-1}$	$1.57\ nm^{-1}$	$24.99\ nm^{-1}$

Table 7.2: Available q-ranges for the SAXS geometry with the LBNL CCD detector: long sample–detector distance of 800 mm, mid-range sample–detector distance of 0.5 m, and the desired extremely short distance case of 70 mm

XFEL energy	q_{max} at 0.8 m	q_{max} at 0.5 m	q_{max} at 0.07 m (extreme case)
5 keV	$0.48\ nm^{-1}$	$0.76\ nm^{-1}$	$5.34\ nm^{-1}$
8 keV	$0.76\ nm^{-1}$	$1.22\ nm^{-1}$	$8.55\ nm^{-1}$
12 keV	$1.14\ nm^{-1}$	$1.83\ nm^{-1}$	$12.82\ nm^{-1}$
16 keV	$1.52\ nm^{-1}$	$2.43\ nm^{-1}$	$17.09\ nm^{-1}$
20 keV	$1.90\ nm^{-1}$	$3.04\ nm^{-1}$	$21.37\ nm^{-1}$
25 keV	$2.38\ nm^{-1}$	$3.80\ nm^{-1}$	$26.71\ nm^{-1}$

For the WAXS geometry, the detector tube is equipped with a Kapton entrance window and will not be linked to the chamber. At the exit side of the tube, the detector will be directly connected and mounted on a supporting base that moves with the arm. The huge dimensions and mass of the AGIPD system make this a real engineering challenge that is currently under investigation. As mentioned above, air pads giving several millimetres of ground clearance can be implemented and probably ensure a safe and precise motion on a well-conditioned floor. To enable an easy exchange of tube or detector, a shutter valve is envisaged between them. The movement of the detector arm should be precise and match a minimal incremental motion of 10 µrad as well as a repeatability of 20 µrad (pixel size of the AGIPD system at a distance of 10 m). The rotation of the long arm can be adjusted to the beam centre set of translations located under the granite table of the chamber. In this way, a centre-of-rotation movement of ± 25 mm in the x and z directions is possible, as well as a vertical motion of ± 30 mm in the y direction. A detailed study of the movable detector stand and the mechanics of the long arm cannot be finalized before the mechanical design of the AGIPD system is known. Nevertheless, a preliminary concept is presented in Figure 7.7.

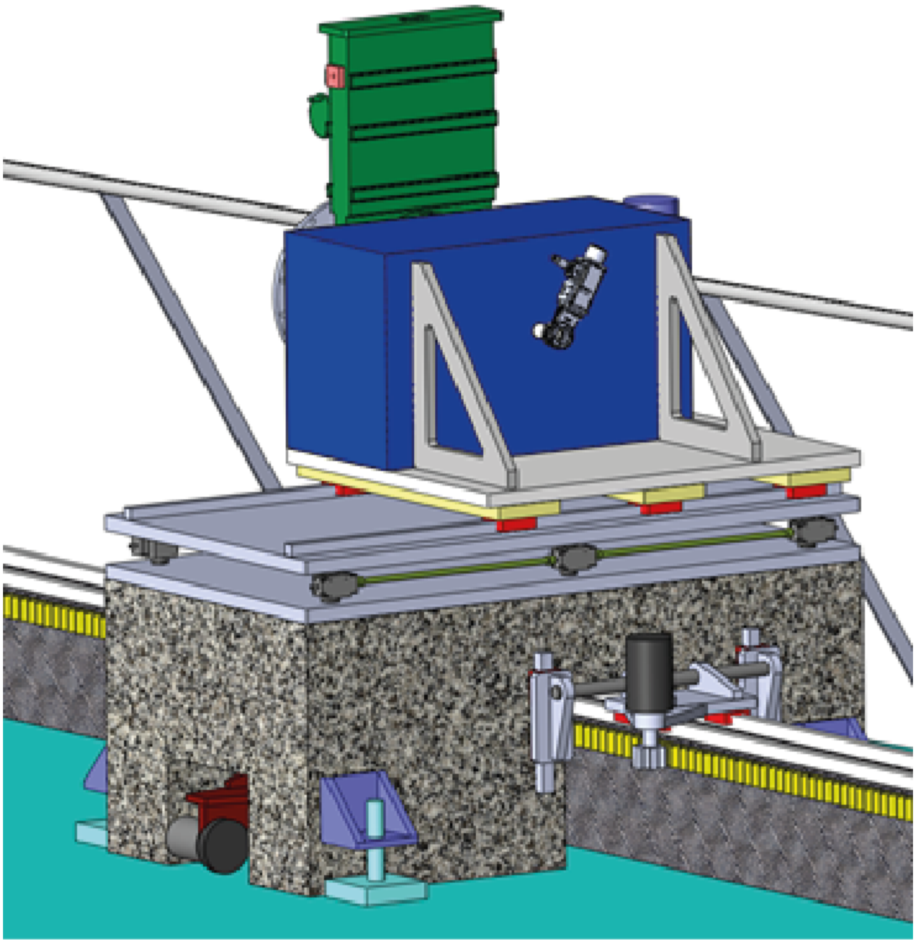

Figure 7.7: Concept of the detector stand hosting the AGIPD system. This table is movable over the available angular range and can be placed (and locked) at any desired location. In the SAXS configuration, the AGIPD is connected to the diagnostics end station via a vacuum pipe.

7.2.2 Vertical arm

Complementary to the horizontal arm, the MID instrument also offers a vertical scattering geometry using a more compact arm. This arm is designed to host a smaller X-ray camera (e.g. the LBNL CCD). It will be 1.5 m long and provide the capability of scanning an angular range from 10° to 75° with a minimum incremental motion of 5 μrad and a repeatability of 15 μrad (one third pixel and a half pixel of the CCD at a distance of one metre, respectively). The small-angle limit is mainly determined by the flange and tube connecting to the diagnostics end station or the SAXS tube. The large-angle constraint is given by the central top flange used for mounting liquid injectors. Design efforts are ongoing aiming to maximize the angular range of the vertical arm.

The vertical arm is directly connected to the base motors of the instrument (under the granite) and can be aligned to the centre of the sample position (specifications in Section 7.2.1, "Horizontal arm—SAXS and WAXS configuration"). Fine adjustment of the detector is realized using a set of motors on the vertical arm allowing a movement of 40 mm perpendicular to the beam with a precision of 15 μm. The detailed concept enabling the necessary degrees of freedom of the vertical arm is still under development (Figure 7.8).

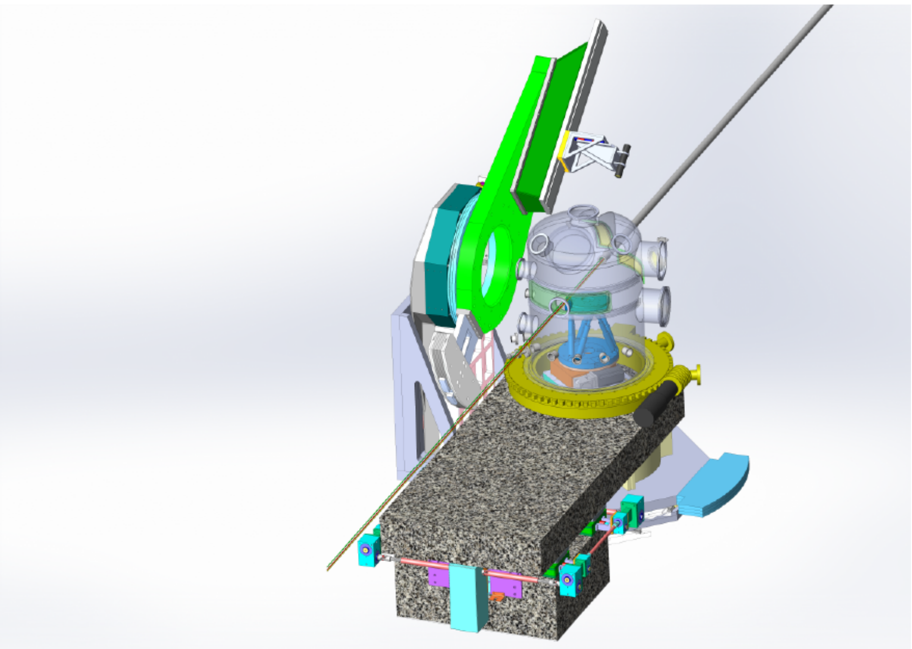

Figure 7.8: Drawing of the experiment chamber with the vertical scattering arm. A small CCD detector with evacuated flight tube can be hosted on the arm. Its rotational movement covers an angle up to 75°. The arm can be aligned with the centre of rotation by adjusting the base movements (under the vessel), and fine-tuning of the detector position on the arm is available via a set of motors. The sample–detector distance available in this configuration ranges from 0.5 m to 1.5 mm. The chip size of the LBNL CCD is up to 30 × 60 mm^2, which determines the size of the WAXS Kapton windows.

7.3 Sample environment

7.3.1 Goniometer

The sample environment at the MID instrument must allow for a multitude of different experiments [75]. A three-circle goniometer (theta, phi, chi) is required as a base for most setups inside the experiment chamber. The goniometer is mounted on a base plate that is movable in *x* (± 100 mm). On this plate, a 360° theta circle is mounted with a minimum step size of 0.1 mdeg. Phi and chi circles are mounted on top of the theta circle, each covering a range of ± 30° with a precision of 0.1 mdeg. Fine alignment of the sample can be done via *x*, *y*, and *z* translation stages within a range of ± 20 mm each and with a precision of 1 µm. It is possible to replace parts of the goniometer setup by a motorized hexapod. In-vacuum hexapods with encoders have been developed by Physik Instrumente (PI) and are being considered by SYMETRIE. ESRF is working together with SYMETRIE to increase the damping and eliminate eigenfrequencies in the low-frequency regime of their hexapods, with very promising first results. Figure 7.9 shows the possible implementation of both devices—the goniometer and the hexapod—in the current design of the sample chamber of the MID instrument.

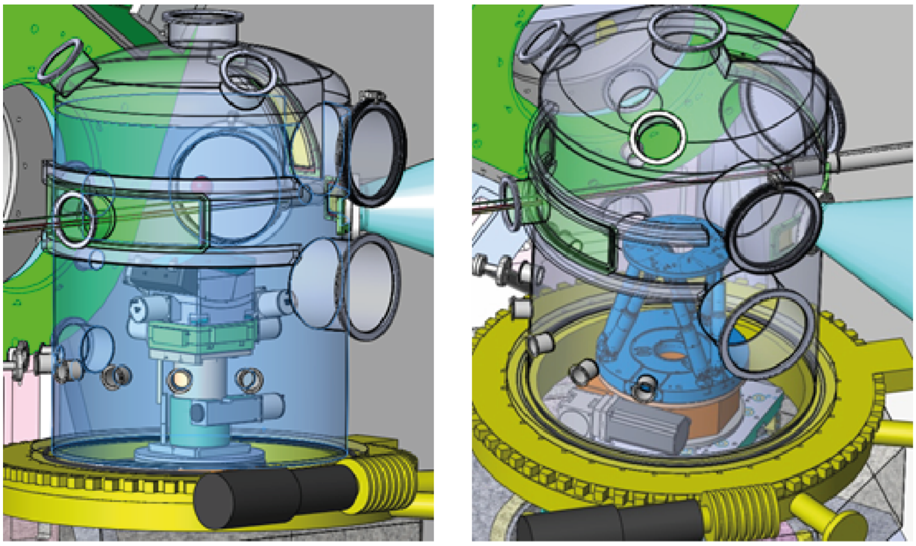

Figure 7.9: *Left:* Technical drawing of the vacuum chamber including a goniometer setup. *Right:* Hexapod on a rotation stage with a vertical translation stage.

Table 7.3: Vertical beam offset at the sample position ($z \approx 959.5$ m) depending on the operation mode. The individual offset will be adjusted using the y-translation of the goniometer or hexapod.

Beam option	Beam offset (min)	Beam offset (max)
Pink beam	0 mm	0 mm
Mono-1 Si(111)	0 mm	12.9 mm
Mono-2 Si(220)	0 mm	15.5 mm
SDL with Mono(111)	0 mm	+ 12.9 mm
SDL with Mono(220)	0 mm	+ 15.5 mm
Deflecting mirror	− 50 mm	+ 15.5 mm

7.3.2 Liquid-jet systems

Liquid injector systems provide unique possibilities for all single-shot experiments with high duty cycle, and different setups will be available at the MID instrument. This sample delivery technique has already proved to be very successful for XFEL experiments [73; 93; 132]. The first custom-made jet system for the European XFEL is under development in a collaboration between the Sample Environment group at European XFEL and Microliquids GmbH in Göttingen, based on a well-known design [20] (Figure 7.10 on the following page). The liquid-jet setup consists of a convergent quartz glass nozzle that is fixed in a custom-made PEEK holder. The nozzle is connected via a capillary tubing to a high-performance liquid chromatography (HPLC) pump, which runs the liquid jet typically at 10–50 bar pressure, resulting in flow speeds up to 120 m/s. The diameter of the jet is tunable in the range from 5 µm to about 200 µm. The liquid is recuperated through a narrow beam catcher aperture, which improves the vacuum and allows the material to be recycled, if necessary. Formation and growth of ice crystals are prevented by heating the catcher aperture, leading to stable operation conditions. The whole setup is mounted on a rail system and can be fixed on the goniometer planned for MID.

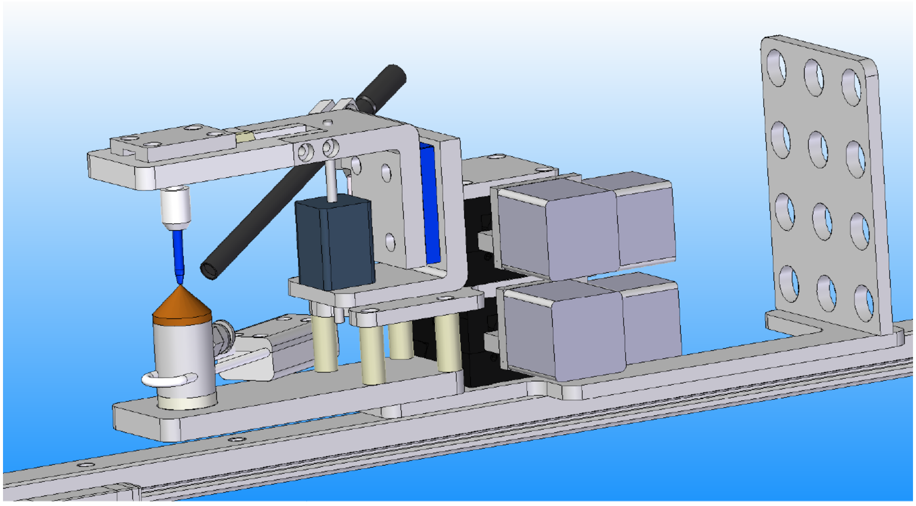

Figure 7.10: Drawing of the liquid-jet setup (Microliquids). The jet nozzle (blue) and the catcher (brown) located on the opposite side are mounted on a rail system to adjust the sample to the X-ray beam. A microscope camera system for this purpose is shown in black.

An alternative method for sample delivery is an aerosol injector under development at Uppsala University. This method is mainly of interest for samples allowing or requiring a lower degree of hydration. It uses a highly collimated particle stream generated by an aerodynamic lens. The lens consists of a series of small apertures through which gas with the sample particles streams. The decreasing aperture diameters can focus the particle stream down to 15 µm at speeds of about 50–100 m/s. By removing the bulk water from around the sample particles, the scattering background caused by water is effectively eliminated. The sample consumption is also smaller than for the liquid-jet setup. A first design is shown in Figure 7.11 on the next page. The MID experiment chamber will be designed so that the top flange fits with the specifications of the aerosol injector.

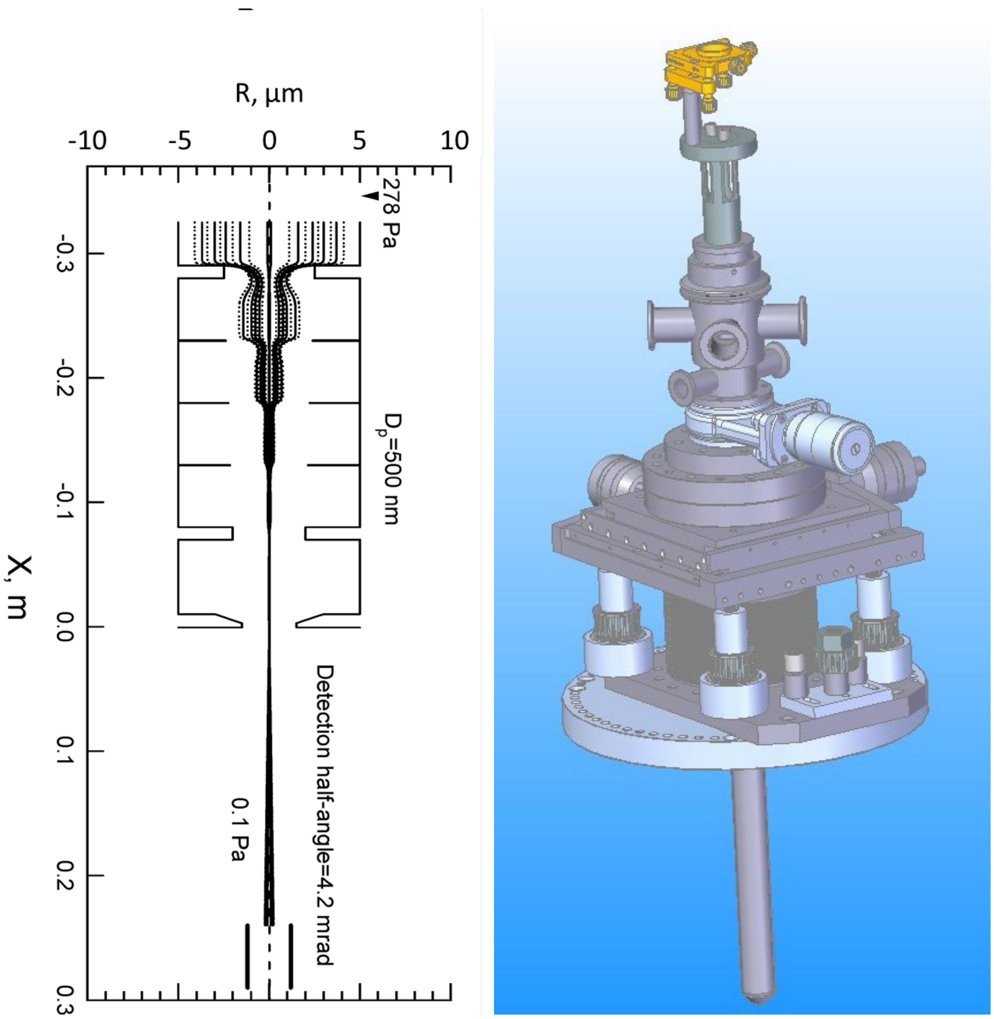

Figure 7.11: *Left:* Sketch of an aerosol injector system. The aerosol is guided through a series of small apertures, resulting in a strongly compressed particle beam (taken from Ref. [138]). *Right:* Drawing of the aerosol jet system (courtesy of D. Westphal, Uppsala University).

7.3.3 Liquids at high temperatures

The study of liquids at high temperatures in transmission scattering geometry is required, for instance, to address questions related to ordering and dynamics in liquid metals. The local structure of liquid metals in the supercooled state has been debated, and, thanks to the femtosecond pulse length of the European XFEL, it will be possible to take snapshots of these transient states in bulk. For such experiments, a wide *q*-range must be covered in one snapshot, and hence a small sample–detector distance and high photon energies are preferred. High photon energies also provide sufficient penetration power for the samples, which can be highly absorbing.

A sample environment for such studies has been developed by Tamura et al. [119]. The liquid is contained in a sapphire cylinder, and, with a sapphire piston, it is possible to apply pressure to the liquid and change the sample thickness (Figure 7.12). Resistive heaters made of tungsten are integrated in the cylinder and allow heating of the sample to 1650°C, which is enough to bring most elements into the liquid state. The use of high energies allows the sapphire to be penetrated and scattering from the sample squeezed between the piston and the bottom of the outer cylinder to be recorded. Single-crystalline sapphire is used for the cell, and, by choosing the right crystallographic orientation, through a careful pre-orientation of the sample cell, it is possible to bring all Bragg spots from sapphire away from the forward scattering. Hence, the scattering from the liquid can be recorded almost without any parasitic background, as demonstrated in Ref. [119]. Such a setup will be easy to integrate in the experiment chamber where the control necessary for alignment will be available.

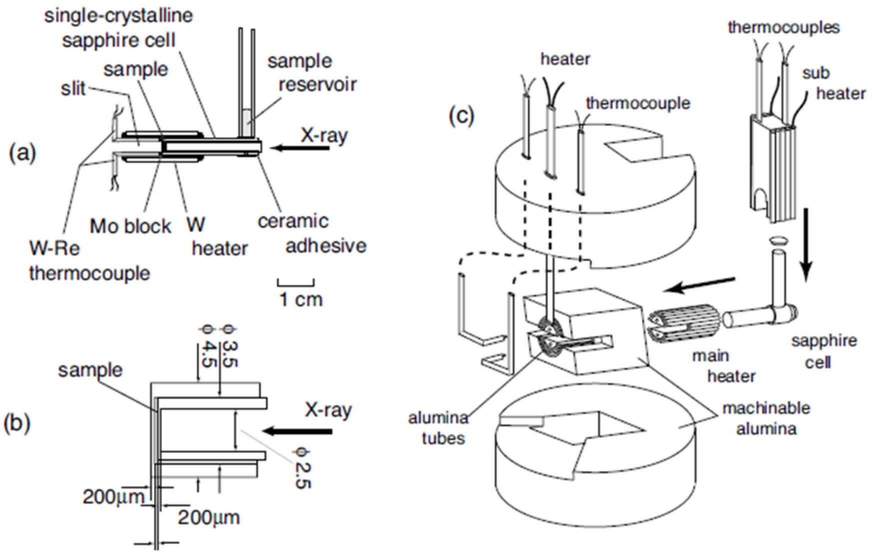

Figure 7.12: Sketch of the high-temperature sapphire sample cell. The X-ray beam travels inside the inner cylinder (used as a piston in the outer cylinder) and traverses the bottom to scatter off the liquid sample contained between the two sapphire slabs. Heating of the entire sample environment is ensured by powerful tungsten resistive heaters. A sample reservoir is connected to the outer cylinder. Figure reproduced from Ref. [51].

7.3.4 Cryostat for pulsed magnetic fields

Studies of the kinetics and dynamics in samples following the application of a pulsed magnetic field are an active area of research. Questions relating to the development of anisotropy in the ordering and dynamics are particularly interesting in connection with phase transitions, magnetic ordering, superconductivity, and so on. The European XFEL will provide novel opportunities for such measurements thanks to its short pulses. Combinations with the possibilities provided by the split and delay line, the coherent properties of the beam, and the optical laser excitation will make such a setup at MID unique. Access to high magnetic field is also interesting for nuclear forward-scattering experiments, where the 220 ns time window of the European XFEL would provide good possibilities to study the beating dynamics of the Mössbauer line due to magnetic hyperfine splitting.

Low-temperature sample environments with pulsed magnetic field capabilities have been developed at synchrotron sources like APS [55] and ESRF [72; 71]. The ESRF system operates with two separate cryostats for the sample and the coils. The sample temperature is controlled by a mini-flow helium cryostat with a minimum temperature of about 5 K. The coil is immersed in liquid nitrogen. The entire system is very compact and shown in Figure 7.13. With the structure of the European XFEL beam and a pulse train duration of 600 µs, it would be possible to follow the response of the sample during the rise, culmination, and relaxation of the magnetic field.

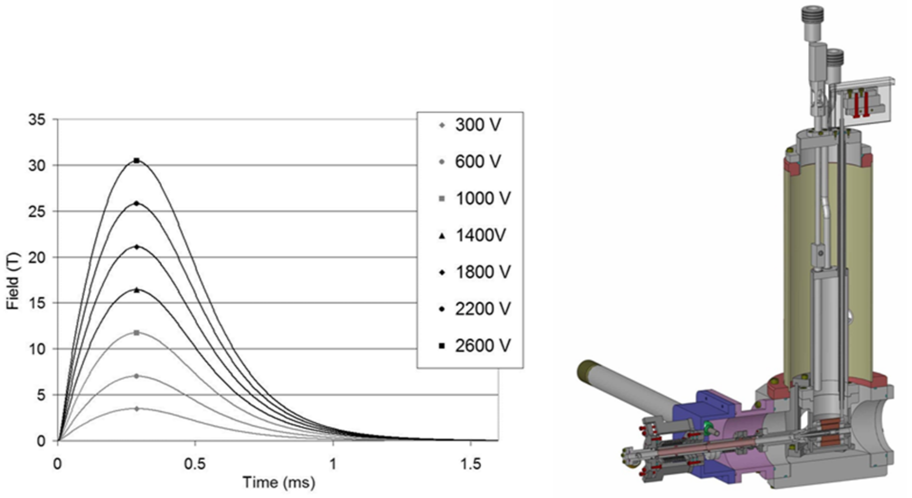

Figure 7.13: Cut view of the pulsed magnetic field mini-cryostat developed at ESRF [71]. The graphs show the magnetic field pulse that builds up and culminates after about 250 µs in a 7 mm slit coil. Different charge voltages are shown, and the peak field can reach 30 T. The pulse duration is about 1 ms, which fits well with the 600 µs duration of a pulse train at the European XFEL. Figure courtesy of P. van der Linden (ESRF).

7.3.5 Liquid surface/interface sample cell

Sample environments for grazing incidence X-ray studies of liquid surfaces and interfaces have been developed [106]. For the liquid–gas interface, the challenges reside in the wish to stabilize a large flat surface (due to the projected beam footprint) and minimize the temperature gradient over the surface, which requires excellent temperature control and stability. Existing sample environments operating with liquid-nitrogen cooling could be implemented in the MID experiment chamber. In this case, the pressure needs to be below the vapour pressure of the liquid sample. In the MID experiment chamber, it is possible to work windowless up to 0.1 mbar thanks to the powerful differential pumping section installed. These operating conditions would make it possible to work with many liquids directly exposed in the chamber without evaporation taking place. The heat exchanger and liquid-nitrogen pipes of the surface sample cell may need a higher vacuum to minimize heat exchange with the surroundings and thus achieve an optimum temperature stability. Still, a setup based on previous experience could be constructed and conveniently operated inside the experiment chamber.

With the high-energy option of MID, it would be possible to study buried interfaces, e.g. liquid–liquid or liquid–solid interfaces. Penetrating the solid with an X-ray beam, the sensitivity of the probe can be tuned by changing the incidence angle. In this manner, it would be possible to investigate the difference in structure and dynamics between the first layer of interfacial liquid molecules and the bulk liquid. Sample cells for X-ray scattering from liquid interfaces have been developed (see e.g. Ref. [103] and references therein) and can easily be integrated into the MID chamber and operated, provided that the liquid does not evaporate.

7.3.6 SAXS chamber

A high-performance SAXS chamber was built for the ID10A beamline at ESRF [114]. It operates in transmission with samples contained in capillaries, but container-free operation is also possible for solids and for liquid samples with low vapour pressure [23]. The vacuum requirements for the temperature stabilization specifications to be reached (1 mK stability or $\Delta T/T > 10^{-4}$) are about 10^{-4}–10^{-5} mbar. These values fit well with the planned performance of the MID experiment chamber. A moderate magnetic field ($B_{\text{max}} = 0.1$ T) can be applied to the sample, either parallel or perpendicular to the beam direction. This field can serve to align magnetic particles, liquid crystals, or ferrofluids. A sample temperature down to 100 K can be reached when the chamber is operated with nitrogen gas from a cold gas generator. This SAXS chamber could be used as it is, only without Kapton windows, in the MID experiment chamber. A drawing of the chamber is shown in Figure 7.14.

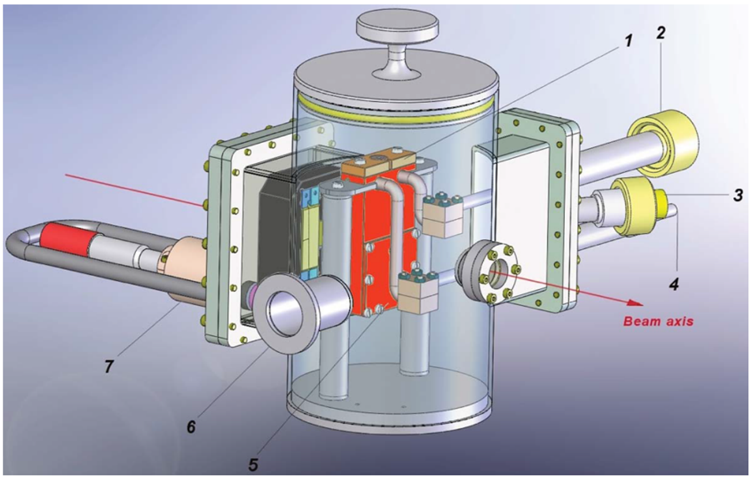

Figure 7.14: Drawing of the low-temperature SAXS chamber at ESRF [114]: (1) sample holder, (2) N_2 inlet, (3) electrical connector, (4) N_2 outlet, (5) heat exchanger (red), (6) vacuum port, and (7) adjustable magnetic assembly (dark grey)

7.3.7 Furnace for Bragg reflection studies

The MID instrument also requires a general-purpose furnace for scattering experiments. Its design could be based on the ESRF sample environment group's furnace with a maximum temperature of more than 1300 K [70]. The ESRF furnace allows scattering and imaging experiments in reflection and transmission geometry. The vacuum compatibility and compactness of the device would ensure a straightforward integration into the MID instrument. A setup optimized for very high temperature stability in the range of 100–500°C is currently being designed by JJ X-Ray in Denmark. Excellent temperature control and stability is achieved by using a stabilized resistive heater and closed-loop PID feedback with input from several temperature sensors. The whole setup is controlled by a Lakeshore 336 four-channel controller. The aim is to obtain sufficient stability to unambiguously observe critical dynamics close to the transition temperature in systems exhibiting a second-order phase transition, e.g. phase ordering binary alloys. The specific goal of the setup is to observe slow critical dynamics by XPCS. Even if slow dynamics is not a focus area at the future MID instrument, a setup with excellent temperature stability will still be required for many experiments.

7.3.8 Millifluidic and microfluidic sample delivery

The vacuum sample environment in the experiment chamber imposes a certain working mode when it comes to changing the sample and the sample environment. Even if the chamber volume is kept at a minimum and the valve connecting to the differential pumping can be opened ca. 15 min after pumping of the chamber has begun (0.1 mbar required), there is a strong inducement not to break the vacuum too often. Interventions in the chamber should be kept at a minimum during a shift, so automatic sample exchange has to be considered. For soft matter and liquids, it seems logical to implement a system of tubes that allow the injection or flowing of sample through the beam. The aim can be simply to exchange the sample, to study the dynamics of flow [29], or to operate a microfluidic setup controlling e.g. liquid alignment and reactions ("lab-on-a-chip" approach) that is compatible with X-ray scattering [8]. Setups have been developed for synchrotron radiation sources for a long time and applied, for instance, in stopped-flow and mixing experiments [90], to study reaction kinetics [82], in nucleation and growth studies [1], and in investigations of protein folding [91]. The time structure and flux of the European XFEL allows orders of magnitude in timescale to be gained compared to earlier experiments, and the combination with coherent illumination will bring new insight into the dynamics. It is also possible to use just the liquid as a carrier medium, for instance to bring in nanoparticles or biological material at a high rate through the beam for high-throughput scattering and imaging experiments.

7.3.9 Free-standing sample environments

Serial positioning of samples in the beam without a container can be achieved by continuous injection with a liquid-jet setup or an aerosol injector, as described above. Maintaining a sample aligned in the beam without container is even more challenging. To this end, levitation sample environments have been built and operated for scattering experiments (see Figure 7.15 on the next page). An aerodynamic levitator is incompatible with the vacuum environment, but electrostatic levitation is possible, as demonstrated by the BESL facility at APS [61; 79]. Electrostatic levitation is applicable to a wide range of materials. Strong electric fields are required to lift the sample and keep it in place.

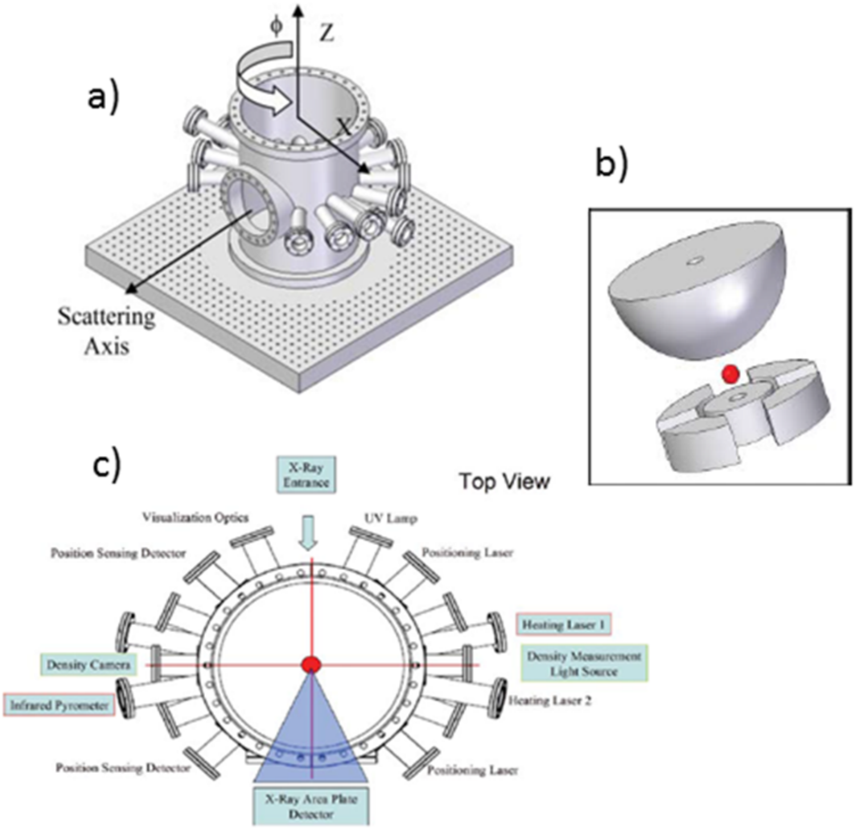

Figure 7.15: Illustration of the electrostatic elevation setup at APS: (a) Outline of the chamber with a 180 mm exit flange. (b) Sketch of the three electrodes used to produce the electric field that keeps the sample in place. (c) Top view of the chamber showing all the view ports required for heating, positioning, and sensing. Figure reproduced from Ref. [79].

If at all possible, it is intended that the MID chamber be compatible with electrostatic levitation. The strong electric fields can potentially create problems for other equipment nearby, but this will require further investigation. A free-standing bridge of liquid can also be formed under the influence of high potential differences. High-energy X-ray scattering experiments were recently performed at APS on such water bridges to search for structural changes and anisotropy of water [111]. This type of container-less setup also constitutes an interesting sample environment for XFEL experiments.

7.4 Nanofocusing

As described in Section 3.1.3, “Primary lens stack (CRL-1)”, Section 3.2.3, “Secondary lens stack (CRL-2)”, and Appendix A, “Beam sizes”, the minimum focal size on the sample position is limited to 1–2 µm using CRL-1 and CRL-2. Aiming for higher spatial resolution, the instrument has to be equipped with an additional focusing optics to achieve beam sizes in the sub-µm range. Abbe’s law (see Equation 3.1 on page 23) states that the focal spot size in the diffraction-limited case depends only on wavelength and opening angle (numerical aperture). Hence, illumination of short focal length optics with a large beam ensures the smallest spot size.

A vacuum vessel 1.5 m upstream of the sample provides enough space for such a setup. The vessel is installed on the same granite block that hosts the sample chamber. Hence, excellent stability is expected for nanofocusing application, but the vessel can be used for any local optics required for a given experiment. A distance of 1.5 m between the nanofocusing lenses and the sample would lead to sub-µm foci over the whole energy range, provided that the beam acceptance of the lenses is about 800 µm. The focal sizes at the sample position in this configuration are listed in Table 7.4.

Table 7.4: Beam sizes at the sample position with a focal distance of 1.5 m and an initial beam size at the lenses of 800 µm. Calculations following Abbe’s formula.

Energy	Beam size (FWHM)
5 keV	473 nm
8 keV	296 nm
12 keV	197 nm
16 keV	148 nm
25 keV	95 nm

A complementary focusing setup can also be implemented directly in the sample chamber and hosted together with a nanopositioning system (e.g. from attocube.com) directly on the goniometer. With a focal length of 300 mm, the beam size at the sample position is further reduced. Assuming that the beam acceptance in this configuration is about 400 µm, focal sizes in the sub-100 nm range can be realized. The values for different energies are shown in Table 7.5 on the facing page.

Table 7.5: Beam sizes at the sample position with a focal distance of 0.3 m and an initial beam size at the lenses of 400 µm. Calculations following Abbe's formula.

Energy	Beam size (FWHM)
5 keV	187 nm
8 keV	117 nm
12 keV	78 nm
16 keV	58 nm
25 keV	37 nm

We note that a nanofocusing setup is not included in the current MID baseline instrumentation. Nevertheless, in the future, it will be mandatory to have such a nanofocusing option at the MID instrument to take full advantage of the scientific possibilities offered by the European XFEL.

8 Ancillary instrumentation and software

8.1 Detectors

8.1.1 Adaptive Gain Integrating Pixel Detector (AGIPD)

The Adaptive Gain Integrating Pixel Detector (AGIPD) [49; 14; 15; 16] is a fast 2D detector development project initiated by European XFEL in collaboration with DESY (project leader: H. Graafsma), the University of Hamburg, the University of Bonn, and Paul Scherrer Institut in Switzerland. The AGIPD chip consists of a classical hybrid pixel array with an application-specific integrated circuit (ASIC) bump-bonded to a silicon sensor. The ASIC is based on 8 metal layer 0.13 µm CMOS technology and uses dynamic gain switching to cover a large dynamic range. An analogue random access memory pipeline enables the storage of images recorded during the 0.6 ms long bunch train of the European XFEL. The stored images are subsequently read out and digitized during the 99.4 ms interval between bunch trains. A block diagram of the integrated circuitry of an AGIPD chip is shown in Figure 8.1. Each chip contains 64 × 64 pixels. The chips are grouped in detector modules of 2 × 8 chips. Four modules are assembled to constitute a detector quadrant. The main AGIPD performance parameters are summarized in Table 8.1 on the following page.

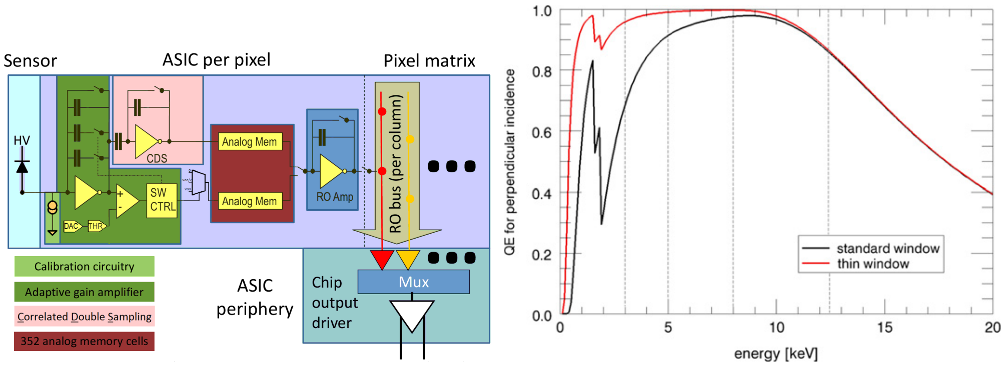

Figure 8.1: *Left:* Block diagram of the integrated circuitry of the AGIPD chip. *Right:* Approximate quantum efficiency as a function of energy for the two different window designs. The thin window significantly improves the quantum efficiency (QE) for energies below approximately 5 keV [15].

Table 8.1: Summary of the AGIPD specifications

Parameter	**Parameter value**	**Comment**
Energy range	QE > 80% in the range 3.5–13 keV	22% QE at 25 keV
Dynamic range	0–34 $\mathrm{Me^{-}\ pulse^{-1}\ pixel^{-1}}$	> 10^4 ph at 12.4 keV, 4×10^4 ph at 3 keV, 14-bit counter
Frame rate	4.5 MHz	—
Noise (ENC)	About 359 e^- rms (100 eV)	Before irradiation, values after irradiation under investigation
Storage cells	352	Max. images per train
Sensor thickness	500 µm	Silicon sensor
Pixel size	200 µm × 200 µm	—
Number of pixel (total)	1024 × 1024 (physical)	Double-sized pixels between ASICs on the same module
Central beam hole	Yes	Variable hole
Mechanical gap between sensor modules	About 3.4 mm (long side) and about 0.4 mm (short side)	

The detector is built to serve the hard X-ray instruments at the European XFEL with particular emphasis on the characteristic 4.5 MHz pulse rate in 10 trains per second. The plan is to integrate one AGIPD in the MID instrument for small- and wide-angle scattering experiments. Details of AGIPD integration at the instrument are still being finalized, and the status can be found in Section 7.1, “Experiment chamber”. The mechanical design of the detector itself is also still under development. It was decided to adapt a variable hole in the centre of the detector, and a module design as shown in Figure 8.2 on the next page (left) was chosen. Within the current concept of quadrant movability, the hole size can be increased to 27 × 27 $\mathrm{mm^2}$, and off-centring is possible. The hole can also take on rectangular shapes or even become a slit opening.

The motion of the detector quadrants is ensured by two-phase stepper motors with microstepping capability and low power consumption. The right side of Figure 8.2 shows the current status of the mechanical design of the AGIPD system. The main operation parameters are summarized in Table 8.2. A drawing of the sliding stages that enable the flexible hole is shown in Figure 8.3 on the following page.

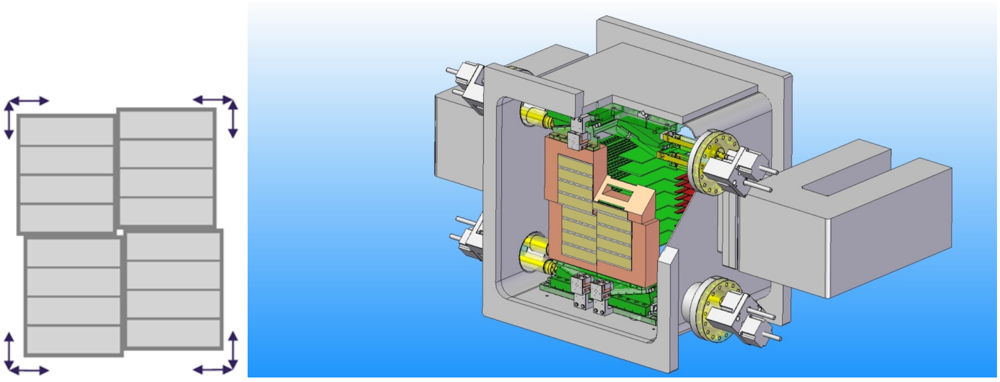

Figure 8.2: *Left:* Configuration of the AGIPD modules into a 1 Mpx detector system ("pile" configuration). *Right:* Preliminary concept for the AGIPD mechanics as of February 2013. The design of the detector is not finalized yet [13].

Table 8.2: Summary of the AGIPD detector operation parameters (preliminary)

Parameter	**Parameter value**	**Comment**
Detector weight	> 500 kg	Sensor, electronics, motors, vacuum vessel (without screws, gaskets, flanges)
Total detector size	Still to be defined	—
Operation pressure	10^{-3} – 10^{-0} mbar	Pressures above 1 mbar are not safe due to HV sparking
Operation temperature	-25°C – 25°C	—
Total power consumption	Less than 28 kW	13 kW into cooling water

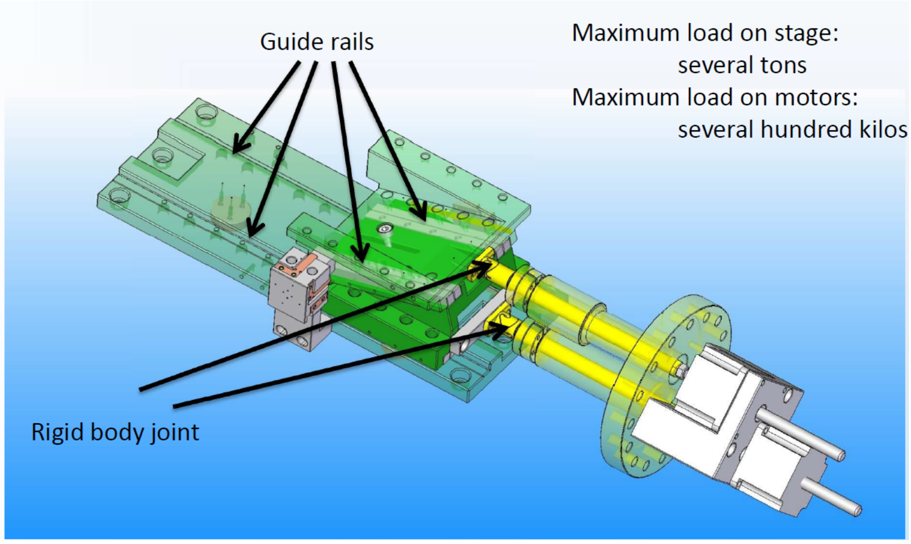

Figure 8.3: Drawing of the sliding stages for the quadrants. They allow adjustment of the size and position of the central hole in the detector. [13]

8.1.2 LBNL CCD—small pixel size X-ray camera

One of the options that the MID instrument must provide is the possibility of photon detection with the highest spatial resolution. Obviously, the best spatial resolution is achieved by having a large sample–detector distance and small pixels. The maximum sample–detector distance at MID is 8 m, which is determined by the hutch size and geometry as well as by the outline of the SASE2 area and the experiment hall. The angular speckle size is the relevant parameter to compare with the available detector resolution. The optimum signal-to-noise ratio (SNR) in XPCS is obtained when the two quantities are identical. In CXDI, oversampling is required, i.e. the detector resolution must be better that the speckle size. The angular speckle size is approximately given by the size of the Airy disc as

$$\Delta\Omega_{\text{speckle}} = 1.22\frac{\lambda}{d} \tag{8.1}$$

where d is the beam size and λ the wavelength. Figure 8.4 on the next page shows the beam sizes needed in order to fulfil the above-mentioned criterion (speckle size equal to pixel size) for energies in the range from 5 to 25 keV, and for different sample–detector distances. The calculation is shown for 200 µm pixels as well as for 30 µm pixels (solid and dashed lines, respectively). The figure illustrates that AGIPD (200 µm pixels) will require small beams (typically 1–2 µm or smaller) in order to correctly resolve the speckles. Only for the lowest photon energies (5 keV) and the maximum sample–detector distance (8 m), beams up to 10 µm can be tolerated. Oversampling will obviously require even smaller foci.

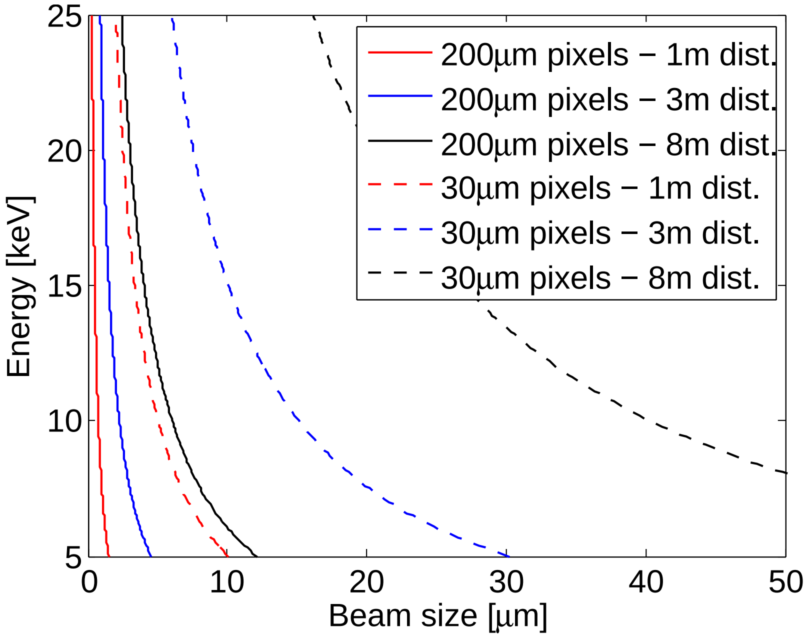

Figure 8.4: Relation between required beam size and energy to match the detector resolution to the speckle size. Two different pixel sizes corresponding to the AGIPD (200 µm) and the LBNL CCD (30 µm) are shown.

While small beams are desirable for certain experiments, there exists a class of multiple-exposure experiments on radiation-sensitive materials where this will be very problematic. The dose absorbed by the sample in order to obtain a certain SNR, contrast, or sampling rate, will scale proportionally to the pixel area. In practice (Figure 8.4), this means that, for a given sample–detector distance, two detectors with different pixel sizes can give similar data quality but only at the expense of energy deposited in the sample. In the example of Figure 8.4, the scattering volume will hence receive a dose which is $(200/30)^2 > 40$ times higher when AGIPD is used. Details of this discussion can be found in Ref. [75].

As anticipated in Figure 8.4, a possible solution to this problem is the use of a CCD [25] developed by LBNL with a pixel size of 30×30 µm^2. At 8 m distance, this detector would allow perfect sampling of speckle patterns generated by a 50×50 µm^2 beam at 8 keV. Contrary to AGIPD, the CCD has only a small dynamic range and no MHz capability, so it is indeed only a viable solution when the ultimate spatial resolution is required. The performance parameters of the detector are summarized in Table 8.3 on the next page. The detector was originally designed for soft X-rays, but the 200 µm Si sensor thickness also makes it useful for higher energies. The chip consists of 960 × 1920 pixels and can work in a frame transfer mode where half of the pixels (960 × 960) are used to record the image and the other half store the previous image before it is read out. In this mode, the deadtime is about 500 µs and hence allows recording of two images from a pulse train at the European XFEL (about 600 µs duration). Ten such image pairs can be recorded per second. The detector will also feature a central hole of a few millimetres diameter allowing the direct beam to pass if the detector is used in forward-scattering geometry. The detector head requires vacuum to operate and is rather compact (about 10 × 10 × 10 cm^3). The sensor is cooled to −50°C during operation, and a vacuum interface is being developed so that the detector with all its connectors can be integrated into the experiment vacuum chamber or become a stand-alone device with a Be window interface. An image of the vacuum interfaces developed by LBNL is shown in Figure 8.5.

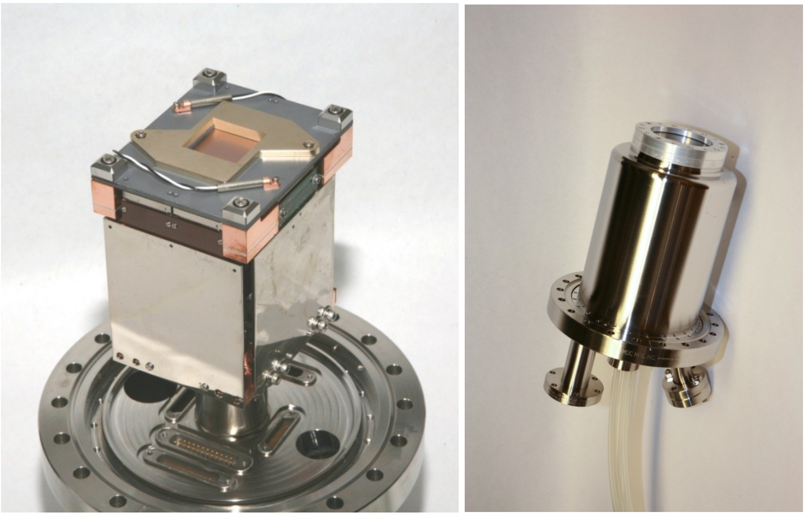

Figure 8.5: Images of the LBNL CCD detector head with the sensor visible (left) and a stand-alone detector with the head in a vacuum vessel (right). Photographs courtesy of John Joseph, LBNL [27].

Table 8.3: Specifications of the LBNL CCD detector

Parameter	Parameter value	Comment
Energy range	0.25–6 keV (optimum)	Defined by the QE of the sensor; operation above or below possible with reduced performance
High-energy efficiency	5 keV (> 99%), 10 keV (78%), 25 keV (10%)	—
Dynamic range	10^5 e^- pixel^{-1}	~ 70 photons/pixel (5 keV), 15 photons/pixel (25 keV)
Max. frame rate	200 kHz	In frame transfer mode (reduced sensitive area)
Noise (ENC)	~ 25 e^- (90 eV) r.m.s.	Before irradiation; values after irradiation under investigation
Sensor thickness	200 µm	Thinned silicon sensor
Pixel size	30 µm × 30 µm	—
Number of pixels (total)	1920 × 960	Active area: 960 × 960 in frame transfer mode
Central beam hole	Yes	Fixed hole diameter (few mm)

Potentially, the detector could be further developed to become even more suitable for hard X-ray experiments. Employing a thicker sensor to increase the efficiency and obtain a larger dynamic range would be of particular interest. Both developments seem feasible. The important boundary condition is that single-photon sensitivity is maintained in the range of 5–25 keV. The plan is to integrate one LBNL CCD at MID to complement the performance of AGIPD, as described above.

8.1.3 Gotthard 1D detector

The Gotthard detector is a 1D microstrip detector system operating with a charge-integrating readout ASIC based on IBM's 130 nm CMOS technology. Using three automatic gain stages, it achieves a dynamic range of 10^4 photons at 12 keV. The ASIC consists of 128 identical channels operated in parallel with a pixel size of 50 µm. The device is capable of operating at 1 MHz without loosing performance regarding noise level and linearity. The readout is realized by a fast readout clock and a parallel architecture consisting of four analogue outputs per chip or 40 ADC channels per detector module. Further specifications can be found in Table 8.4 and in Ref. [84].

Table 8.4: Specifications of the Gotthard detector

Energy range	**> 3.5 keV**
Dynamic range	10^4 (at 12 keV)
Min. integration time	80 ns
Deadtime	< 50 ns
Readout frequency	Up to 1 MHz
Linearity	Better than 0.5%
Pixel size	50 µm
Sensitive area	64×8 mm^2
Sensor thickness	320–500 µm

It is planned to use a 1D Gotthard strip detector module with 1280 pixels in the single-shot spectrometer to be installed at the diagnostics end station of MID. If a diamond analyser is used in (111) or (333) scattering geometry, the entire range from 5 to 25 keV can be covered with a resolution better than ~ 1.5 eV if the detector is placed 1 m from the crystal (Figure 3.28 on page 55). It is necessary to move the detector on an arc as the energy and Bragg angle change. Different models for a suitable vacuum integration enabling this motion are being discussed. Possibilities for 4.5 MHz operation of a Gotthard 2.0 detector are also being scrutinized.

8.2 Optical lasers

X-ray investigations of matter subject to optical excitations have been very valuable for the understanding of dynamics on atomic length scales in a multitude of different systems. As a consequence, most synchrotron and XFEL sources offer at least one instrument with an optical laser, hence allowing optical pump–X-ray probe measurements [120; 34; 129]. The integration of an optical laser is foreseen at all instruments at the European XFEL. At MID, the focus will be on materials science applications. In conjunction with the coherent illumination and the possibilities offered by the X-ray split and delay line and the experiment chamber, the optical laser system will make the MID instrument a unique setup for scattering and imaging studies.

8.2.1 Pump laser system

The European XFEL Optical Lasers group is currently developing a general pump–probe laser that will be made available to all instrument groups. One laser system will be installed in every SASE area. The laser system at SASE2 will be shared among the two instruments HED and MID—and possibly a future third instrument (NNN) that could be constructed later. Consisting of a front end, a burst mode power amplifier, and a non-collinear optical parametric amplifier (NOPA), the laser system can be operated in two different modes: high-repetition operation in pump–probe (PP) mode and low-repetition operation in molecular alignment (MAL) mode. The parameters of both laser modes are listed in Table 8.5.

Table 8.5: Main laser parameters delivered by the European XFEL Optical Lasers group in pump–probe (PP) mode and molecular alignment (MAL) mode.

Parameter	PP mode	MAL mode
Pulse length	sub-15 fs – 100 fs	800 fs – 500 ps
Intensity	0.2–3 mJ	~ 100 mJ
Wavelength	800 nm	1030 nm
Frequency	0.2–4.5 MHz	200 kHz intra-burst (“pulse on demand”)
Frequency (burst mode)	10 Hz	10 Hz

The PP laser system (Figure 8.6) is based on a high-energy NOPA. An ultrastable fibre seed laser is synchronized by the general European XFEL synchronization system (further information in Section 8.3.1, “Timing system”) and drives the amplification process. Its pulses are launched through a long delay stage that compensates for jitter and drifts in the laser system and permits temporal overlap between the X-rays and the optical laser. A fibre-based pre-amplifier modifies and splits this signal to enable white-light generation in one branch and high-energy chirped-pulse amplification in a second branch. The high-energy pulses of the amplifier chain can either be sent directly to the experiment or utilized to drive the parametric process. Therefore, the fundamental wavelength has to be converted to double frequency. The white-light signal is pre-chirped by dispersive mirrors and spatially and temporally overlapped in non-linear crystals. Depending on the required energy and repetition rate, four NOPA stages can be employed.

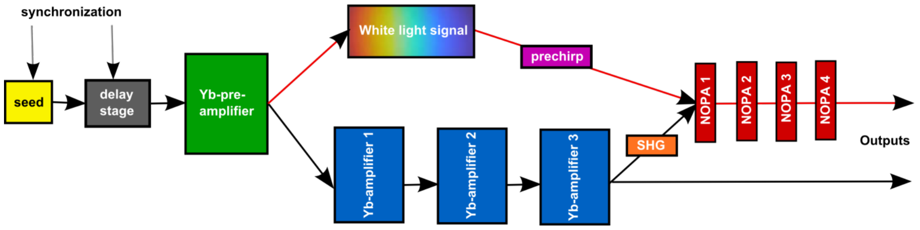

Figure 8.6: Concept of the laser system provided by the European XFEL Optical Lasers group. The synchronized seed pulse passes an Yb pre-amplifier and is split in two parts—one for white-light generation, one for a further amplification chain (Yb amplifier 1–3). Both branches are recombined in a set of NOPAs and generate the output beam.

In PP mode, very short pulses (in steps: 15 fs, 30 fs, 50 fs, 100 fs) at 800 nm are available with the option to generate second-harmonic (SHG: 400 nm) and third-harmonic (THG: 266 nm) radiation to achieve a shorter wavelength. In addition, a commercial broadband device (TOPAS, Light Conversion) will provide access to a tunable wavelength spectrum ranging from ca. 400 nm to several micrometres. Jitter and coincidence management will be mandatory to achieve adequate time resolution for the experiments. This requires a thorough treatment of dispersion and non-linearity to provide the shortest pulse duration on the sample inside the chamber.

In the MAL mode, long pulses in the range of either 800 fs (compressed) or 500 ps (uncompressed) at 1030 nm with the highest possible pulse energies up to 100 mJ (200 kHz) will be available on request. Additional SHG and THG units could complement this setup.

The following section introduces the current optical layout of the instrument laser hutch of SASE2, where the delivered laser beam will be tailored according to the experiment requirements. The instrument laser hutch is conveniently located close to the MID experiment chamber. Distinct parts and components of the setup are currently undergoing a careful evaluation in close collaboration with the Optical Lasers group and may be subject to changes. Figure 8.7 illustrates the most recent layout.

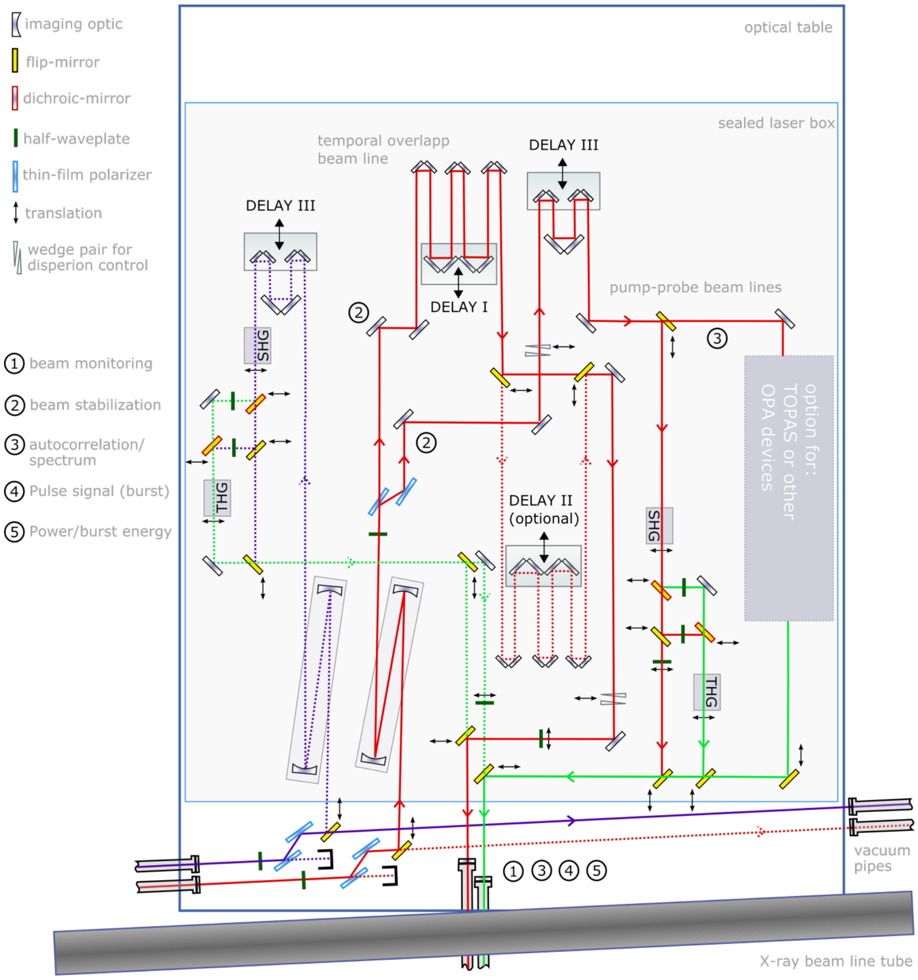

Figure 8.7: Sketch of the optical setup in the instrument laser hutch at SASE2 (no real distances). *Red beamline:* 15–100 fs short pulses. *Purple beamline:* Long pulses (800 fs or 500 ps) with high energies. *Green beamline:* Optical path for multiple wavelengths (SHG: second-harmonic generation, THG: third-harmonic generation, OPA: optical parametric amplifier).

For repetition rates below 1 MHz, pulses will be delivered from the main laser hutch to the instrument laser hutch via a 6 inch vacuum pipe (~ 1–10 mbar). The beam diameter at the exit window will be around 30 mm. For higher repetition rates, pulses will be send through a 2 inch pipe (red beam in Figure 8.7) with a 10 mm beam diameter at the same vacuum pressure. At the exit of the delivery beam pipe, a remotely controllable attenuator might be used to tweak the input power and energy. This would consist of a half-wave plate in combination with a thin-film polarizer (TFP) pair. However, in the case of 15 fs pulse duration, the coating on the TFP must be very advanced in order to control dispersion. Yet, it is not clear whether the manufacturers can provide such a design. Alternatively, exchangeable reflective optics (i.e. output coupler) could permit a gradual attenuation, or splitters could be used.

In PP mode, the beam will be picked up by a displaceable mirror from any of the two entrance beamlines. After relay imaging, it will be divided into a coincidence arm and a pump–probe arm. The attenuator/splitter ($\lambda/2$ wave plate and thin-film polarizers) could permit a continuously tunable energy splitting. As previously mentioned, such an attenuator is currently subject to evaluation as TFPs might introduce too much chirp (pulse broadening). Delay Line III is responsible for pump–probe scanning, whereas Delay Line I and the optional Delay Line II are quasi-fixed translation configurations to compensate any coarse path differences between the pump–probe and the coincidence arms. This could occur when changing the instrument setup between experiments. To ensure that the pump–probe and coincidence beams can be selected individually, they are sent into separate delivery pipes through the wall to the MID experiment hutch.

Displaceable SHG and THG units offer frequency conversion, and wave plates ($\lambda/2$, $\lambda/4$) will serve as polarization control for the actual experiment, but also for THG (i.e. Type I critical phase matching in beta barium borate (BBO)). For slightly longer pulses between 20 fs and 30 fs, commercial broadband devices such as TOPAS (Light Conversion) might be utilized to significantly increase the wavelength range.

All reflective mirrors are equipped with zero-dispersion coatings for the respective wavelength regimes. In the current design, the 15 fs long pulse will enter the MID laser hutch negatively chirped to 300 fs pulse duration. Its dispersion is conjugated to fused silica. By propagating through fused silica components with predetermined length, the pulse will be compressed to the 15 fs bandwidth limit (reached inside the chamber after the entrance window). The amount of fused silica required will be on the order of 30–40 mm thickness. A pair of fused silica wedges will make fine-tuning possible in each arm. The drawing actually does not include any additional fused silica imaging optics between the setup and the experiment vacuum chamber (i.e. for focusing).

For SHG, THG, and TOPAS operation, the turning mirrors must be changed to optimize the dispersion and reflection efficiency. The actual arrangement of components is not predetermined and might change at a later stage.

For the MAL configuration, the setup poses much lower constraints on dispersion. On the other hand, mirrors need to have sufficient damage thresholds. In Figure 8.7 on page 143, the purple dotted line represents the optical path of the long pulses at 1030 nm. Optional SHG, THG, and polarization control units may be inserted for completion.

The numbers in Figure 8.7 on page 143 indicate monitoring and control locations where pulse properties should be analysed and corrected if appropriate. Some of these observation points are locally flexible, whereas others might have to be fixed (i.e. beam stabilization in red beamline after delay lines). The whole assembly will be mounted on an optical table that is mechanically damped and possibly passively stabilized against thermal drift. A sealed box will protect the setup against any potential external disturbance. The beam delivery pipes will not contain any mirror mounts (purely transmitting) and will be decoupled from the optical configuration to ensure maximum stability. The design is considered as initial, and further extensions may be added at a later stage. Possible changes foreseen could include simultaneous operation of different pulses (length, wavelength, spectra, beam size, etc.).

8.2.2 Temporal overlap of optical laser and XFEL beam

Determination of the temporal overlap between the optical laser pulses and the XFEL pulses is crucial for ultrafast experiments. The expected jitter of both sources is ~ 100 fs and therefore longer than their shortest pulse widths (sub-15 fs). As a consequence, this jitter limits the time resolution of ultrafast experiments and must be improved by a time-of-arrival measurement for every pulse. Several methods are under investigation to provide this measurement. The most promising ones are spectral encoding, spatial encoding, and terahertz (THz) streaking.

Spectral encoding [54; 18; 17; 44] relies on the ionization of a semiconductor target (e.g. Si_3N_4) by the XFEL radiation. This results in a change of the optical transmission of the material. Using a temporally chirped broadband laser pulse ($\Delta\lambda \approx 80$–200 nm) coupled out of the pump laser system, this modification can be probed collinearly by transient absorption. Here, depending on the chirp, different frequency components of the optical beam translate to different arrival times and give a direct insight into the temporal relation between the XFEL and optical laser. The temporal resolution of this method is limited by the energy resolution of the transient absorption spectrometer, and the temporal range available depends on the spectral width of the optical probe pulse. A chirp of $\Delta\lambda = 200$ nm results in about $\Delta t = 3$ ps.

Spatial encoding [44] relies on the interaction of the XFEL beam with a transparent sample at a certain angle. Depending on the angle, the arrival times on the different positions of the target differ and generate temporal information about the beam. The transmission change of the target can be probed using an optical laser beam coupled out from the pump laser system. This change can be measured with a high-resolution microscope. The temporal range of the technique is mainly limited by the XFEL beam size at the interaction point and by the angle of the target. The temporal resolution is defined mainly by the resolution of the microscope.

THz streaking [41; 120] is an alternative method to determine the temporal overlap. To this end, a part of the optical laser is used to generate single-cycle THz pulses. These pulses are used to investigate the photoelectron spectrum of a noble-gas target that was previously ionized by an incident XFEL pulse. Since the THz streaking field has a long rise time, it is possible to determine not only the arrival time, but also the temporal profile of the individual XFEL pulses.

All three methods are currently under investigation by the X-Ray Photon Diagnostics group, the Optical Lasers group, and the individual instrument groups of European XFEL. For the MID instrument, spectral encoding seems to be the best solution to determine the temporal overlap of the optical laser beam and the XFEL. In the case of THz streaking, the required optical laser intensity is too high and will weaken the pump pulse. Furthermore, the spatial encoding might not be usable for strongly focused XFEL beams, as the available temporal range is very small in this case.

8.3 DAQ system

The MID instrument's data acquisition (DAQ), data management, and scientific computing system architecture foresees multiple levels and will be fully integrated with the hardware and software framework developed by the DAQ and Control Systems group at European XFEL. This is a common development that serves the entire facility. Central parts of the development are reviewed in the following sections.

8.3.1 Timing system

The European XFEL timing signal will be distributed from a central place in the injector building close to the master oscillator. It will receive a stable 1.3 GHz clock signal from the master oscillator, and a further input will be a 50 Hz signal from the mains. A master timing transmitter distributes the signal. The MID instrument will be connected to this master timing transmitter via an optical fibre and receive all necessary information about triggers and shot IDs. This output has a delay compensation keeping the propagation time to the receivers constant and correcting for timing drifts. Furthermore, slave timing transmitters will be set up near the experiment hall that send out the received information to all their clients.

The 2D pixel detectors for the MID instrument (mainly the AGIPD system) will be connected to the timing system via an interfacing micro telecommunications computing architecture (MTCA) module called “Clock and Control”. This module is a special rear transition module (RTM), compatible with the DAMC2 boards of DESY. As timing-related input, it uses TCLKA or TCLKB clocks to receive the continuously running 4.5 MHz bunch clock or 99.3 MHz (22 × 4.5 MHz) as well as the eight M-LVDS bus signals. The bus is used for triggers and to decode the information provided on the bus data line. In this manner, the AGIPD system will be fully synchronized with the machine. The images are stamped with the pulse and train ID, and the detector can track and follow changes in bunch pattern distribution, machine parameters, etc.

The programmable logic controller (PLC)–based solution for slow control and monitoring applications will use Beckhoff’s Ethernet for control automation technology (EtherCAT) series. Most applications do not require synchronization with the machine. However, for those that do rely on timing, special synchronization modules are used allowing hardware triggering down to nanosecond levels. Those modules will be connected to the timing systems through an RJ45 connector and a level converter or through a specialized RTM for the timing receiver allowing a higher fan-out and longer distances to the PLC modules.

The pump–probe laser system will be locked to the optical synchronization system. As for almost all non-MTCA.4 systems, the interfacing will be done with RJ45 connectors and level converters. For the systems defined up to now, these will use TTL levels and BNC connectors.

8.3.2 Karabo software tool

Efficient usage of the European XFEL requires an interface that allows for experiment control, readout of all associated detectors and sensors, safe storage of all produced data, and immediate (on-the-fly) data analysis. Using a standardized, homogeneous software landscape allowing communication between distributed endpoints of any category (e.g. control, acquisition, data management, or scientific computing) is an essential point to fulfil these requirements. Such a software system, named Karabo, is currently under development at European XFEL[46].

The scientific computing framework is part of Karabo. It is directly linked into the data management layer and capable of autonomously and immediately starting data processing once the data arrives at the online storage layer. Data is processed in modules, which can be connected to form a scientific analysis workflow.

Every module provides a compute function, which can be equipped with customized procedural code. Furthermore, each module provides a sophisticated way to (self-)describe its possible/expected configuration parameters. Part of this configuration allows the description of expected input and output (I/O) channels. I/O channels are specific to the underlying data structures, and only channels using the same underlying data structure may be connected between modules. The framework will provide highly optimized data structures for common tasks (such as image processing or meta-data handling). Foreign data structures can easily be "registered" to the system and are readily exchangeable between modules. In most cases, binary blobs may be used, allowing shipping of files (of any type) between modules.

Modules can be written in either C/C++ or Python. Java may become available at a later stage. Usage of Karabo data structures within the compute function is encouraged though not required. In a minimal case, system calls to existing binary scientific applications can be issued and the produced files be transferred to the next connected module(s). In a more involved case, an existing source code is placed into the compute function, slightly adapted to use Karabo data structures for I/O, and fetches the startup parameters from the Karabo configuration system. This allows for a more flexible re-usage of such modules in other workflows (as the I/O channels are standardized and not file format specific). If circumstances allow, algorithms may be rewritten or newly developed to exploit the full capability of the framework, such as GPU-enhanced computations (Figure 8.8 on the next page).

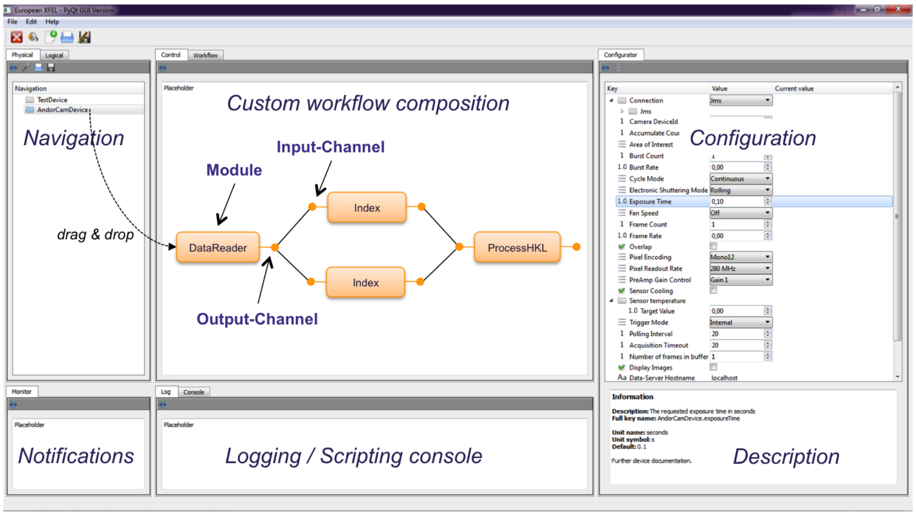

Key	Value	Current value
Connection	Jms	
Jms		
Camera DeviceId		
Accumulate Cou		
Area of Interest		
Burst Count	1	
Burst Rate	0,00	
Cycle Mode	Continuous	
Electronic Shuttering Mode	Rolling	
Exposure Time	0,10	
Fan Speed	Off	
Frame Count	1	
Frame Rate	0,00	
Overlap	☐	
Pixel Encoding	Mono12	
Pixel Readout Rate	280 MHz	
PreAmp Gain Control	Gain 1	
Sensor Cooling	☐	
Sensor temperature		
Target Value	0,00	
Trigger Mode	Internal	
Polling Interval	20	
Acquisition Timeout	20	
Number of frames in buffer	1	
Display Images	☐	
Data-Server Hostname	localhost	

Information

Description: The requested exposure time in seconds
Full key name: AndorCamDevice.exposureTime

Unit name: seconds
Unit symbol: s
Default: 0.1

Further device documentation.

Figure 8.8: GUI-based creation and configuration of scientific workflows. Workflows can be composed by dragging and dropping required modules from the navigation panel. Individual modules may be configured by a simple click. Data flows are configured by connecting compatible I/O channels.

A standardized wiki page [58] is associated to each module, which holds documentation, authorship(s), references, institution logos, etc. This wiki page will be editable in a regular browser or directly within the multipurpose Karabo GUI system.

Workflows may be assembled and edited by means of dragging and dropping modules and their connections. Workflows can be stored and shared (following the general rules of data privacy and security), executed, paused, and stepped. Workflow execution will be visualized, and any data may be inspected at execution time (limited frequency and resolution). Notifications about finished runs or errors will be visible in the GUI and can be forwarded via email or SMS. Final results of workflow runs will be re-integrated into the data management layer for seamless and user-aware access. The workflow allows for pipelined operation on chunks of data and automatic parallelization on a per-module level (either as CPU threads or in form of distributed computing, depending on where modules run relative to each other).

Data will be locally accumulated, and the compute function only triggers upon completed accumulation. The I/O and the processing system are decoupled from each other (asynchronous I/O) such that data can be transferred while modules are processing. The workflow system provides built-in protection systems for memory overruns. By default, the processing speed will automatically be adjusted to the I/O capabilities. The data transfer model follows an event-driven poll architecture, allowing maximum per-module performance even on heterogeneous hardware. From a technology point of view, workflows are realized by two different communication patterns, a message-broker-based publish–subscribe pattern (allowing $N \times N$ module control communication and distributed meta-data management) and a highly optimized point-to-point communication pattern (for fast I/O transfer between connected modules). Communication in general is cross-network, cross-language (initially C/C++ and Python), and cross-platform (initially Linux and MacOS X, later Windows 7) capable.

Besides the graphical system, a command line/scripting interface (based on Python/iPython) is available for workflow control.

The described system is intended to provide scientists with a user-friendly system that allows them to process their collected data using in-house hardware and community-driven, sharable software resources in the form of plug-in modules or predefined workflows.

Of particular interest for MID are GPU-accelerated auto- and cross-correlation calculations. For weak scattering and noisy datasets, droplet-izing algorithms and event correlation could be of interest (see Ref. [23] and references therein). These also speed up the processing of thousands of images. Iterative phase retrieval algorithms and ptychography also require top-notch computing facilities to handle the large data streams, for instance coming from the AGIPD system running at full speed.

8.4 Infrastructure

The stability of room temperature and humidity is important for different parts of the MID experiment area. Especially, the experiment hutch, the optics hutch, and the instrument laser room contain sensitive devices. Therefore, the temperature and humidity stability was set to 21°C ± 0.5°C and 45% ± 2.5%, respectively. All other rooms have a 21°C ± 1°C temperature stability and 45% ± 10% humidity stability. The design of the air conditioning systems for the different rooms takes these stability values into account as well as the estimated power requirements. A list of rooms relevant for the MID instrument can be found in Table 8.6. It is currently being investigated whether an upgrade of the air conditioning system in the optics hutch is required to get an even better temperature stability (0.1 K).

Table 8.6: Power and air conditioning stability requirements of the MID instrument

Location	Power	Temperature stability	Humidity
Experiment hutch	5 kW	21°C ± 0.5°C	45% ± 2.5%
Optics hutch	5 kW	21°C ± 0.5°C	45% ± 2.5%
Rack room	50 kW	21°C ± 1°C	45% ± 10%
Control room	8 kW	21°C ± 1°C	45% ± 10%
Instrument laser room	6 kW	21°C ± 0.5°C	45% ± 2.5%
Laboratory	6 kW	21°C ± 1°C	45% ± 10%
Sum	**80 kW**	—	—

The bulk part of motor drives and controllers for devices in the experiment hutch, the optics hutch, and at the end of the tunnel will be placed in the MID rack room. Therefore, the major requirements for power and power dissipation are assigned to this room. Currently, the rack room is located on the hall floor, but it could be moved to the roof of one of the hutches if additional floor space is required.

9 Timeline and risks

9.1 Planning risks

The goal is to have the MID instrument "ready for beam" by June 1, 2016 with all main components in place. First lasing at SASE2 is foreseen in December 2016.

The current status of the planning indicates that this will be possible if sufficient resources are available to prepare calls for tender, follow up on procurement and suppliers, perform acceptance tests and assemblies, and finally proceed to installation in Schenefeld. The current allocation of personnel to MID will be insufficient to undertake all these activities.

It is of major importance that sufficient laboratory space is made available to MID so the aforementioned assembly and test tasks can be performed in a proper environment. These tasks need to begin before the Schenefeld laboratories become available. There is no free space at the current location of European XFEL (office buildings) for such work, however, so laboratory space must be made available at the HERA South hall or elsewhere.

From the budget point of view, in the current understanding, all the items described in this TDR as *baseline* can be realized within the financial envelope foreseen for construction of the MID instrument. One important exception is the split and delay line unit, which will be rather expensive. To build this device, we rely on success of the German Federal Ministry of Education and Research (BMBF) grant application that was submitted by S. Eisebitt from Technische Universität Berlin. Additional funding for realizing specialized instrumentation (e.g. sample environments like furnaces, SAXS chambers, and optics for nanofocusing) has been applied for in collaboration with external user groups, e.g. through the Röntgen–Ångström cluster or BMBF.

The high-energy option still awaits an experimental verification of high-harmonic lasing, which is planned at LCLS later in 2013.

To progress with the mechanical design of the SAXS/WAXS arm in a detailed study, it will be important to finalize the mechanical design of AGIPD as soon as possible. Specification and definition of items at the interface to other groups (e.g. lead hutches, DAQ systems, diagnostics units, and detectors) develop in parallel with the design of MID. Close coordination between the various activities is not always easy.

9.2 Technological risks

The technological risks currently identified seem not to be severe.

CRL optics are successfully used at LCLS without problems relating to ablation. Even if the first CRL-1 transfocator at MID is located closer to the source, simulations suggest that it will still be far from the damage threshold. CRLs have been operated at synchrotron sources for years, often at average heat loads higher than those that will occur at the European XFEL. Hence, we believe that Be CRLs can be successfully used. The risk for optical components of the beamlines has been addressed by H. Sinn et al. in the TDR for the European XFEL X-Ray Optics and Beam Transport group. Obviously, protection systems have to be installed to prevent damage to mirrors, monochromators, attenuators, and absorbers.

The experiment chamber and setup we propose carry minor risks. The most challenging part will be the rotational motion of the vacuum flange at the bottom of the experiment chamber. Outgassing of granite needs further studies, and it might become necessary to install a bottom plate.

Windowless operation requires the powerful differential pumping section described in this report. The device was specified with help from ESRF's vacuum group, which has extensive experience in this area. In any case, a diamond window can be inserted to separate the beamline vacuum (UHV) from the vacuum of the experiment hutch.

9.3 Schedule

A rough time schedule related to planning, manufacturing, and installing the main components is given in Figure 9.1. A more detailed planning has been developed for the split and delay line, a summary of which is shown in Figure 9.2 on the following page.

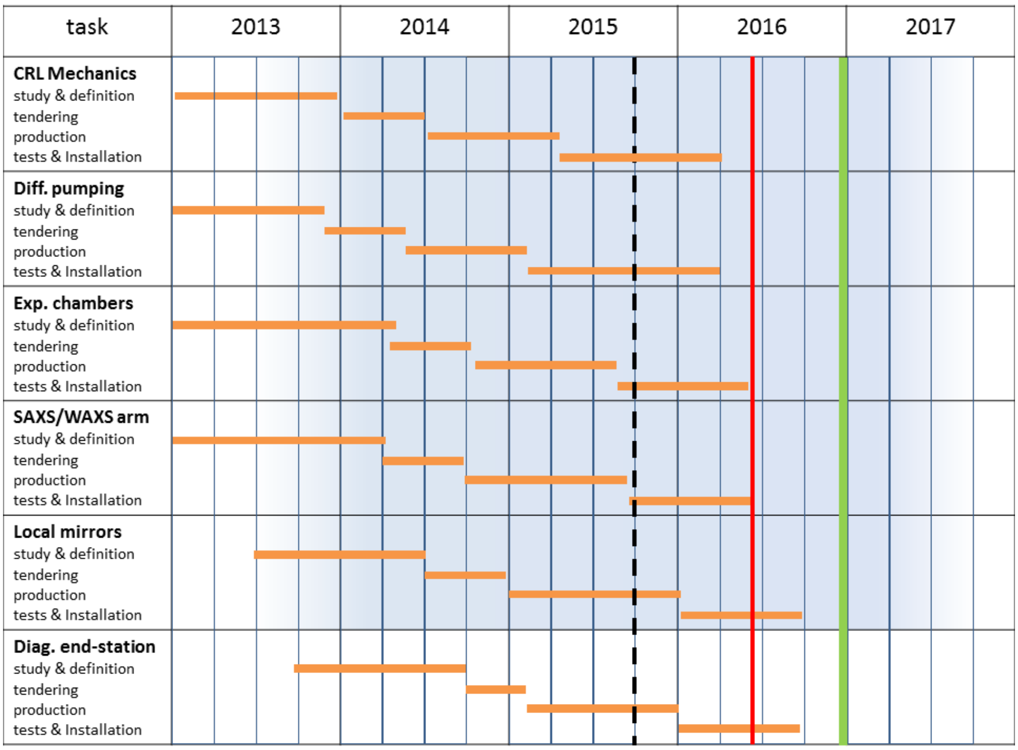

Figure 9.1: Gantt diagram of the main components under development by the MID group. The dashed black line indicates the current estimate of when installation in the experimental hall can begin. The red line indicates the "ready for beam" date (June 1, 2016). The green line indicates first lasing at SASE2 (December 2016)

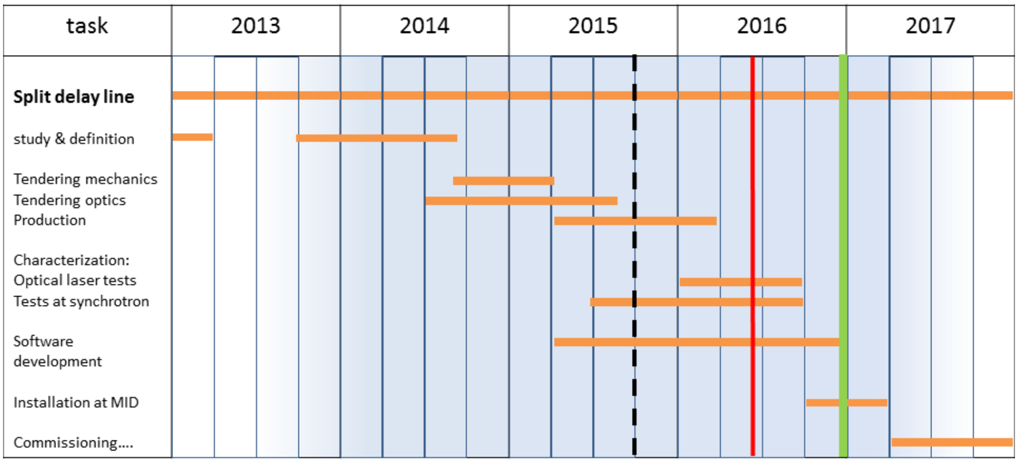

Figure 9.2: Gantt diagram concerning development of the X-ray split and delay line. The dashed black line indicates the current estimate of when installation in the experimental hall can begin. The red line indicates the "ready for beam" date (June 1, 2016). The green line indicates first lasing at SASE2 (December 2016)

10 Acknowledgments

The engineering collaboration with the ISDD division at the European Synchrotron Radiation Facility (ESRF) is acknowledged.

We thank B. Heisen, M. Mattenet, G. Palmer, L. Samoylova, J. Sztuk-Dambietz, and JJ X-Ray for contributions to this TDR.

J. Als-Nielsen, S. Bari, L. Batchelor, J. Becker, N. Coppola, S. Eisebitt, F. Fihman, G. Geloni, H. Graafsma, G. Grübel, J. Grünert, T. Haas, J. Hajdu, J. Hastings, A. Koch, M. Kuster, P. Kwasniewski, A.-V. Lalechos, M. Lederer, B. Lengeler, T. Lippmann, C. Mammen, H. Marques, M. Nakatsutsumi, J. Navntoft, C. Ozkan, H.F. Poulsen, A. Robert, I.K. Robinson, W. Roseker, G. Ruocco, N. Saaristo, T. Salditt, E. Schneidmiller, C. Schroer, J. Schulz, H. Sinn, K. Tiedtke, T. Tschentscher, M. Turcato, I. Vartaniants, D. Xiaohao, C. Youngman, and M. Yurkov are acknowledged for inspiration, feedback, and stimulating discussions.

The Central Instrument Engineering (CIE) group, the technical support groups, the scientific instruments, and the European XFEL Management Board are acknowledged for their support.

Many thanks to K. Ament and I. Flegel for editing and proofreading the document.

A Beam sizes

This appendix details the beam size evolution for the different focusing schemes and the individual beam sizes on the optical elements along the MID beamline. It refers to Chapter 5, “Beryllium lenses”, for the description of the focusing option and to Section 3.1.3, “Primary lens stack (CRL-1)”, and Section 3.2.3, “Secondary lens stack (CRL-2)”, for the general layout of the MID instrument.

A.1 Beam size and divergence

The photons are generated in the 220 m long SASE2 undulator (magnetic length: 175 m). The source point is assumed to be in the middle of the third-to-last undulator segment. The expected source size for energies in the range from 5 to 25 keV varies between 60 and 25 µm (FWHM) in both the horizontal and the vertical direction. It varies more with bunch charge than with energy [109, Figure 10]. The expected divergence in the 5 to 25 keV range is between 4.2 and 0.7 µrad [109, Figure 12]. The lowest number corresponds to 25 keV and 1 nC bunch charge. The highest number corresponds to 5 keV and 20 pC bunch charge.

Without focusing, an upper limit for the beam size can be evaluated using a conservative approximation for the beam divergence [109, page 26] and multiplying this with the distance. The initial source size can be neglected here.

$$\delta\theta_{\mathrm{FWHM}}\,[\mathrm{rad}] = 1.2 \times 10^{-5} (\lambda\,[\mathrm{nm}])^{3/4} \tag{A.1}$$

$$D_{\mathrm{FWHM}} = \delta\theta_{\mathrm{FWHM}} \cdot z \tag{A.2}$$

$$D_{7\sigma} = 7/2.35 \cdot \delta\theta_{\mathrm{FWHM}} \cdot z \tag{A.3}$$

A.2 Intermediate focusing scheme

The intermediate focusing scheme is based on the generation of a focus at 726 m after the source point. The divergent beam after the focus will be focused again by CRL-2 at 931 m. This scheme is explained in detail in Chapter 5, "Beryllium lenses". Table A.1 and Table A.2 on the facing page show the XFEL beam sizes in locations between CRL-1 and CRL-2, and between CRL-2 and the sample position, respectively.

Table A.1: Beam size (FWHM) at the different beamline components in the *intermediate focusing* scheme after CRL-1. The intermediate focus in this configuration is located ~ 726 m after the source point.

Device	Position [m]	5 keV Size [µm]	8 keV Size [µm]	12 keV Size [µm]	16 keV Size [µm]	25 keV Size [µm]
CRL-1	235	938	663	493	401	292
Imager-1	242	918	640	482	391	285
Shutter-1	264	858	607	453	368	269
Offset mirror	290	811	575	429	349	256
C-Monochromator	307	775	549	410	334	245
Distribution mirror	390	631	449	337	277	205
Slits-1	727	135	120	109	101	90
Attenuator-2	880	313	232	182	155	124
Slits-2	888	326	241	189	160	127
XBPM and XGMD	918	346	254	198	167	131
Monochromator-1	929	396	288	222	186	143
CRL-2	931	399	290	223	187	144

Table A.2: Beam size (FWHM) at the different beamline components in the *intermediate focusing* scheme after CRL-2

Device	Position [m]	5 keV Size [µm]	8 keV Size [µm]	12 keV Size [µm]	16 keV Size [µm]	25 keV Size [µm]
Shutter-2	940	262	191	147	123	95
Monochromator-2	946	156	113	87	73	57
Split and delay line	949.5	109	80	62	52	40
Shutter-3	951.5	83	61	47	40	31
Mirror	954	63	47	37	31	24
Sample position	959.5	18	16	14	12	10
Beam stop	968.5	116	84	65	55	42

A.3 Collimating then focusing scheme

In the *collimating then focusing* scheme, CRL-1 collimates the beam until CRL-2, which then focuses the beam onto the sample. Compared to the previous scheme (*intermediate focus*), the beam size on CRL-2 is larger and results in a smaller focus on the sample position, according to Abbe's formula. The beam size between CRL-1 and CRL-2 is constant and can be seen in Figure A.1 on the next page. Table A.3 on the following page shows the beam size at different positions of the beamline after CRL-2 and until the beam stop.

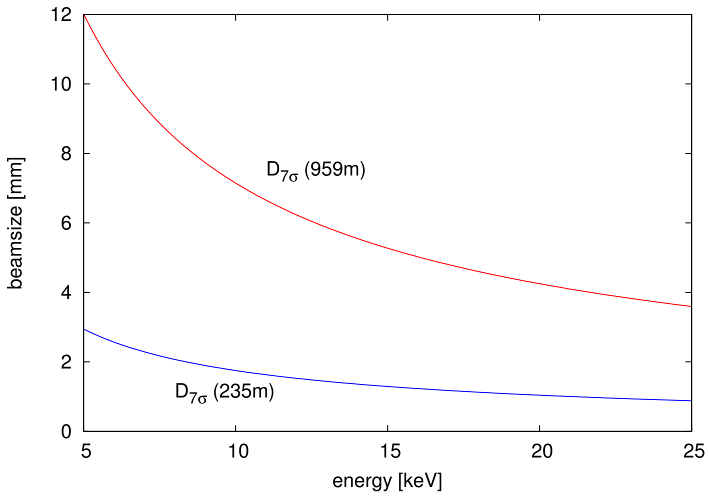

Figure A.1: Expected 7σ beam size of the X-ray beam at the MID instrument. The size of the unfocused beam at the sample position at ~ 959 m is shown in red. At 235 m, a CRL lens stack will be available to collimate the beam. The beam size of a collimated beam after this CRL stack is shown in blue.

Table A.3: Beam size (FWHM) at the different beamline components in the *collimating then focusing* scheme after CRL-2

		5 keV	**8 keV**	**12 keV**	**16 keV**	**25 keV**
Device	**Position [m]**	**Size [μm]**	**Size [μm]**	**Size [μm]**	**Size [μm]**	**Size [μm]**
Shutter-2	940	635	446	329	265	190
Monochromator-2	946	374	263	194	157	112
Split and delay line	949.5	261	183	135	109	78
Shutter-3	951.5	195	137	101	82	59
Mirror	954	146	103	76	61	44
Sample position	959.5	7.6	6.7	6.1	5.7	5.1
Beam stop	968.5	277	195	144	116	83

A.4 Focusing with CRL-1

The CRL-1 stack is capable of focusing the XFEL beam directly onto the sample. This configuration will produce the largest focus of all described schemes. The beam sizes along the whole beamline are presented in Table A.4 and in Figure A.2 on the following page.

Table A.4: Beam size (FWHM) at the different beamline components for focusing only with CRL-1

		5 keV	**8 keV**	**12 keV**	**16 keV**	**25 keV**
Device	**Position [m]**	**Size [µm]**	**Size [µm]**	**Size [µm]**	**Size [µm]**	**Size [µm]**
CRL-1	235	949	675	507	415	307
Imager-1	242	923	658	494	305	300
Shutter-1	264	895	638	480	394	293
Offset mirror	290	863	616	464	381	284
C-Monochromator	307	839	599	452	371	277
Distribution mirror	390	742	532	403	333	251
Slits-1	727	351	269	219	191	158
Attenuator-2	880	221	189	167	153	135
Slits-2	888	217	187	165	152	135
XBPM and XGMD	918	211	183	163	151	134
Monochromator-1	929	201	178	160	149	133
CRL-2	931	201	177	160	148	133
Shutter-2	940	199	176	159	148	132
Monochromator-2	946	198	176	159	148	132
Split and delay line	949.5	198	176	159	148	132
Shutter-3	951.5	198	176	159	148	132
Mirror	954	198	176	159	148	132
Sample position	959.5	198	176	159	148	132
Beam stop	968.5	198	176	159	148	132

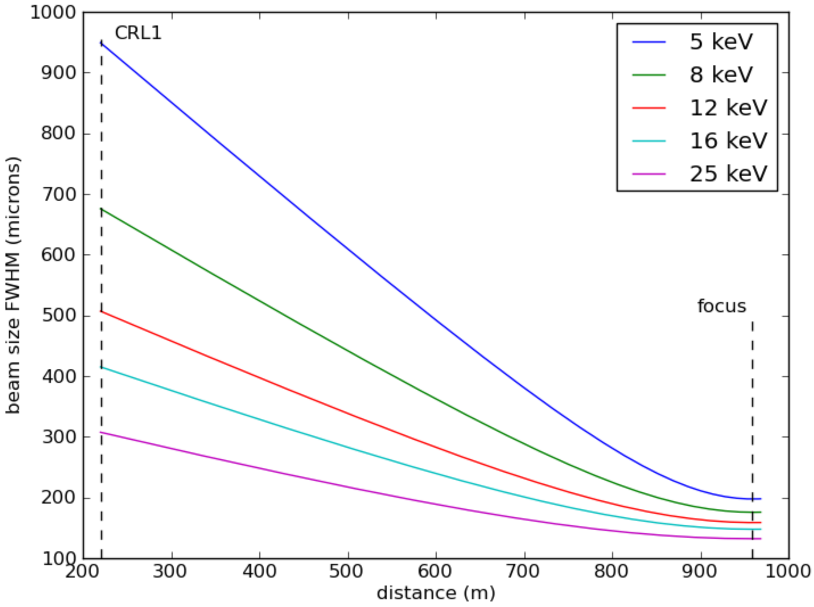

Figure A.2: Evolution of the beam size by focusing onto the sample position using only CRL-1. The graph presents the diameter (FWHM) of the XFEL beam at 5 keV (blue), 8 keV (green), 12 keV (red), 16 keV (cyan), and 25 keV (purple). The dashed lines indicate the position of the CRL-1 stack and the focus at the sample position. The calculation is based on Equation 3.1 on page 23 and Equation 3.2 on page 23.

A.5 Focusing the naturally divergent beam only with CRL-2

Aiming for the smallest possible foci at the sample position, the naturally divergent beam can be focused only by CRL-2 (CRL-1 not used). Table A.5 and Figure A.3 on the following page present the beam sizes of this scheme in the ideal case. We note that the lens acceptance D_{eff} is typically smaller than the size of the naturally divergent beam.

Table A.5: Beam size (FWHM) at the different beamline components for focusing only with CRL-2

Device	**Position [m]**	**5 keV Size [µm]**	**8 keV Size [µm]**	**12 keV Size [µm]**	**16 keV Size [µm]**	**25 keV Size [µm]**
CRL-2	931	3730	2621	1934	1559	1154
Shutter-2	940	2686	1888	1393	1123	803
Monochromator-2	946	1584	1114	822	662	474
Split and delay line	949.5	1102	775	572	461	330
Shutter-3	951.5	826	581	429	345	247
Mirror	954	620	436	321	259	185
Sample position	959.5	1.80	1.60	1.45	1.35	1.20
Beam stop	968.5	1171	823	607	489	350

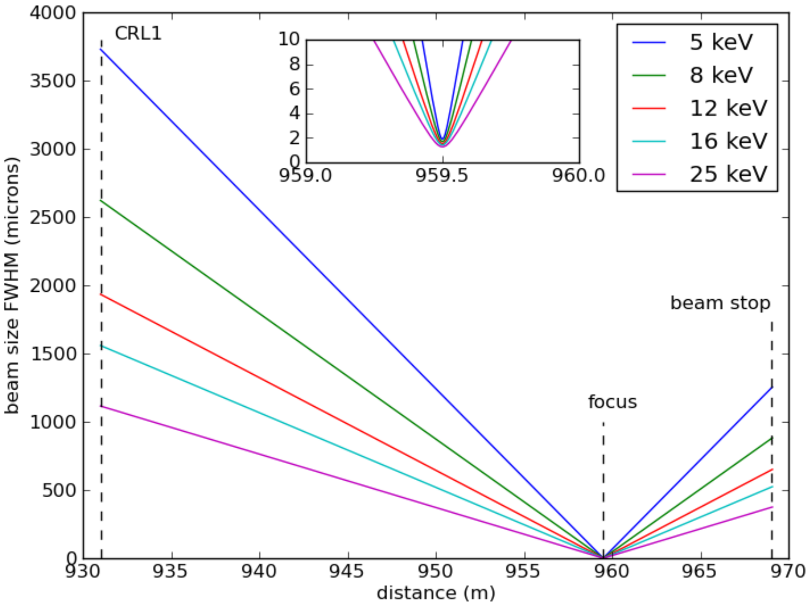

Figure A.3: Evolution of the beam size by focusing the naturally divergent beam with CRL-2 (CRL-1 not used). The graph shows the diameter (FWHM) of the XFEL beam at 5 keV (blue), 8 keV (green), 12 keV (red), 16 keV (cyan), and 25 keV (purple). The dashed lines indicate the position of the CRL-1 stack and the focus at the sample position. The inset shows a magnification of the area around the sample position at 959.5 m. The calculation is based on Equation 3.1 on page 23 and Equation 3.2 on page 23. In this geometry, the smallest spot sizes are obtained.

B Split and delay line calculations

This appendix presents additional information concerning the split and delay line (SDL) calculations.

B.1 Atomic scattering factors

The starting point for evaluating the scattering by a Bragg crystal is to calculate the X-ray scattering from single atoms. To this end, the complex atomic scattering factor f is used. f denotes the coherently scattered amplitude by all electrons of the atom [48] (Thomson and Rayleigh scattering). f is therefore expected to be proportional to Z, the number of electrons in the atom. Incoherent Compton scattering is neglected, as this is relevant only at higher photon energies. f can be decomposed into several parts, taking the specific dependencies on energy and scattering angle into account. The imaginary part of f allows absorption to be incorporated. We thus write

$$f = f_1 + \imath f_2 \tag{B.1}$$

f_2 does not vary with angle but strongly with energy. More about different notations on the scattering factor can be found in [48, pp. 183–184, 208].

Detailed calculations of f require knowledge of the electron distribution in the atom. f_1 and f_2 can also be determined experimentally using atomic photoabsorption cross sections and Kramers–Kronig dispersion relations. Henke et al. have investigated this issue in detail and published tables of f_1 and f_2 in the forward scattering direction [48]. More precisely, one can write $f_1^{\mathrm{fwd}} = f_0 + \Delta f'$ and $f_2^{\mathrm{fwd}} = f_2 = \Delta f''$, where the primed contributions specifically indicate the energy variation. The values for f_1^{fwd} and f_2^{fwd} in the forward direction can also be obtained using the software package XOP [95]. Alternatively, the XOP package provides $f_1^{E>>\mathrm{edges}}(\theta) = f_0 - \Delta f_0(\theta)$. In order to obtain f_1 for a given energy and angle, we have to disentangle and combine parts of f_1^{fwd} and $f_1^{E>>\mathrm{edges}}(\theta)$. For silicon and carbon, the necessary curves are shown in Figure B.1 on the next page and Figure B.2 on the following page.

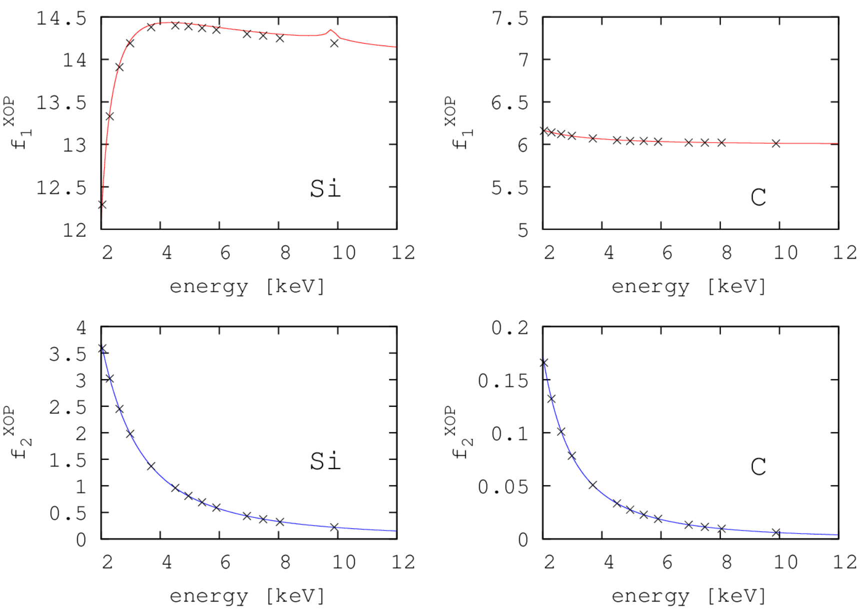

Figure B.1: The lines show the atomic scattering factors f_1^{fwd} and f_2^{fwd} for Si and C as calculated using XOP [95]. The crosses are the tabulated values taken from [48].

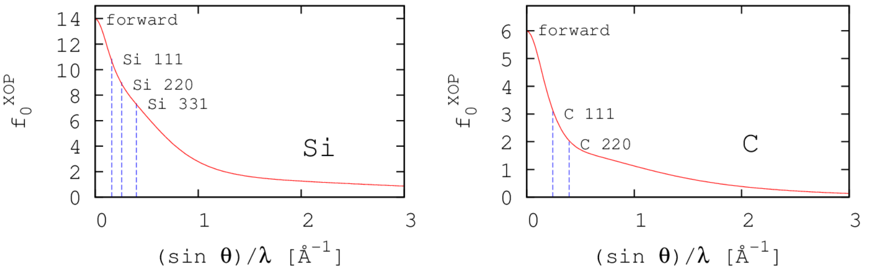

Figure B.2: Atomic scattering factors $f_1^{E>>\text{edges}}(\theta)$ for Si and C as calculated by XOP [95]

Away from the forward direction, we need to subtract an angle-dependent correction $\Delta f_0(\theta)$ from the real part of the scattering factor in the forward direction f_1^{fwd}, also when considering Bragg reflections. We will investigate $f_1^{E>>\text{edges}}(\theta)$ in more detail and follow [48, p. 207] and [131, pp. 9–10]. The value for the scattering factor without anomalous correction terms, assuming a spherical electron charge distribution around the nucleus, can be calculated using $k = \frac{4\pi \sin\theta}{\lambda}$ and

$$f_1^{E>>\text{edges}}(\theta) = \sum_n \int_0^\infty 4\pi r^2 \rho_n(r) \frac{\sin kr}{kr} \mathrm{d}r \tag{B.2}$$

For $\theta = 0$ (forward direction), one has $\frac{\sin kr}{kr} = 1$, and the integral gives one electron. Accordingly, the sum above yields $f_1^{\text{fwd}} = Z$ [131]. Henke et al. define

$$\Delta f_0(\theta) = Z - f_1^{E>>\text{edges}}(\theta) \tag{B.3}$$

This illustrates how f_1^{fwd} can be corrected to obtain the angular variation of f_1 as $f_1 = f_1^{\text{fwd}} - \Delta f_0(\theta)$.

Henke et al. also show how to tackle the calculation of the energy-dependent part [48, pp. 205–206]. The starting point is the scattering of an electromagnetic wave with frequency ω_0 by a single electron bound to a nucleus with resonant frequency ω

$$f_{\text{osc}} = \frac{\omega_0^2}{(\omega_0^2 - \omega^2) - I\eta\omega_0} \tag{B.4}$$

where η is a damping constant. This must be integrated over all electrons of the atom, and the real and imaginary parts can be separated. Furthermore, a small relativistic correction needs to be added. Finally, there is a relationship between the oscillator density and the photoabsorption cross section μ [48, pp. 205–206], and the following expression is obtained

$$f_1^{\text{fwd}} = Z^* + \frac{1}{\pi r_e hc} \int_0^\infty \frac{\epsilon^2 \sigma_a(\epsilon)}{E^2 - \epsilon^2} d\epsilon \qquad \text{with} \qquad Z^* \approx Z - (Z/82.5)^{2.37} \tag{B.5}$$

$$f_2^{\text{fwd}} = \frac{1}{2 r_e hc} E \sigma_a(E) \tag{B.6}$$

Silicon has an absorption edge at 1.84 keV, while carbon has no edged in the X-ray regime. The energy-dependent part of f_1, $\Delta f'$, is therefore of little (Si) or no (C) importance in the cases considered here, namely at energies between 5 and 10 keV (Figure B.1 on the preceding page).

B.2 Crystal structure factor

The structure factor for a Bragg reflection must take both the scattering by individual atoms and their arrangement in the lattice into account [131]. In analogy with Bartels et al. [9, Eq. 9] or Cole and Stemple [24, Eq. 1.2], we write the structure factor as

$$F_h = F_h' + \imath F_h'' \tag{B.7}$$

where F_h' and F_h'' are specified as

[9]
$$F_h' = \sum_n f_{1n} \exp^{2\pi\imath(hx_n+ky_n+lz_n)} \tag{B.8}$$
$$F_h'' = \sum_n f_{2n} \exp^{2\pi\imath(hx_n+ky_n+lz_n)} \tag{B.9}$$

with $f_n = f_{1n} + \imath f_{2n}$ and (hkl) denoting the Miller indices of the reflections. Since the spatial part of the structure factor may be complex, $F_{h'}$ and $F_{h''}$ themselves are both complex numbers. These expressions are required when calculating the thickness of the beam splitter.

B.3 Linear absorption coefficient

The linear absorption coefficient μ must also be taken into account [10]. Its inverse is the absorption length t_{abs}. The linear absorption coefficient describes the transmission of X-rays through an absorbing medium

$$I = I_0 \cdot e^{-\mu x} \tag{B.10}$$

The linear absorption coefficient is connected to the imaginary part of the atomic scattering factor and thus also to the imaginary part of the crystal structure factor. We have

[10]
$$\mu = \frac{2r_e\lambda}{V} F_0'' \tag{B.11}$$

[48]
$$\mu = 2r_e\lambda \sum_i n_i f_{2i}(0) \tag{B.12}$$

B.4 Absorption, extinction, and reflectivity

When an X-ray beam travels through a thin crystal at Bragg condition, it experiences absorption, transmission, and reflection. It is possible to quantify these intensities P_A, P_T, and P_R as a function of crystal thickness [10]. These values are related by

$$P_R + P_\mathrm{A} + P_\mathrm{T} = 1 \tag{B.13}$$

Following the paper by Bartels et al. [10, Eq. 41–43], we write

$$P_\mathrm{R} = \frac{\sinh^2(A\sqrt{1+g^2})}{Q_0^2} \tag{B.14}$$

$$P_\mathrm{A} = -\frac{2g\sinh(A\sqrt{1+g^2})}{Q_0} \tag{B.15}$$

$$P_\mathrm{T} = \frac{1+g^2}{Q_0^2} \tag{B.16}$$

where Q_0, A, and g are given by [10, Eq. 40, 38, and 37]

$$Q_0 = \sqrt{1+g^2}\cosh(A\sqrt{1+g^2}) - g\sinh(A\sqrt{1+g^2}) \tag{B.17}$$

$$g = -\frac{t}{4t_\mathrm{abs}} \tag{B.18}$$

$$A = \frac{t}{t_\mathrm{ext}} \tag{B.19}$$

Here, t_abs is the absorption length and t_ext is the extinction depth for the Bragg case. They are given by [9, Eq. 3 and 4]:

$$t_\mathrm{ext} = \frac{\sqrt{\gamma_0\gamma_h}V}{r_\mathrm{e}\lambda C_\mathrm{pol}|F_{H'}|} = \frac{\sin\theta_\mathrm{B} V}{r_\mathrm{e}\lambda|F_h'|} \tag{B.20}$$

$$t_\mathrm{abs} = \frac{1}{\mu\left(\frac{1}{\gamma_0}+\frac{1}{\gamma_h}\right)} = \frac{\sin\theta_\mathrm{B}}{2\mu} \tag{B.21}$$

where $\gamma_0 = \sin(\theta_\mathrm{B} - \phi)$ and $\gamma_h = \sin(\theta_\mathrm{B} + \phi)$ are the so-called direction cosines [121, Eq. 6; 94, text after Eq. 7; 9, Eq. 3]. In the case of a symmetric cut crystal, $\phi = 0$. For σ-polarized light (scattering plane perpendicular to the direction of $\vec{E}$ of the photon), the polarization factor is $C^\sigma_\mathrm{pol} = 1$. For π-polarized light, it is $C^\pi_\mathrm{pol} = |2\cos\theta_B|$. $V = a^3$ is the volume of the unit cell, and $|F_h'|$ is the part of the structure factor $F_h = F_h' + iF_h''$ that originates from the real part of the atomic scattering factors (see Equation B.8 on the facing page).

When Bragg scattering is not considered, the transmission through a medium is given by $I_{out} = I_{in} e^{-\mu x}$. In analogy, we write the probability P_E of observing the intensity I_{out} after traveling the distance t in the crystal as

$$P_E = e^{-\frac{\mu t}{\sin\theta}} = e^{-\frac{t}{2t_{\mathrm{abs}}}} \tag{B.22}$$

P_{E} follows an exponential decay and is independent of the choice of lattice planes, but P_{T} is not, as the transmitted intensity at Bragg condition depends, of course, on the reflected intensity.

C Beryllium

Beryllium is an excellent material for XFEL optics (high ablation threshold, low Z, relatively high melting point). Here, we address the issue of determining which Be grade is best for X-ray optics and what impact impurities or voids in the Be lenses will have on the wavefront as it propagates along the beamline.

C.1 SAXS measurements of Be grades

SAXS measurements on different grades of Be sheets and lenses have been performed on Beamline ID02 at ESRF in collaboration with P. Kwasniewski (ESRF). The sheets and lenses were provided by RXOPTICS [101]. In Figure C.1 on the next page, unprocessed Be sheets of different origin are compared. So far, the IF-1 material from the company Materion Brush Beryllium & Composites was considered to be the state-of-the-art–grade Be for CRLs. Unfortunately, the maximum thickness of a sheet is 0.5 mm for IF-1. This leads to lens apertures R_0 that, in many cases, are comparable to or smaller than the expected 7σ beam size. A reduction in effective lens aperture below the beam size leads to beam broadening at focus (see Chapter 5, "Beryllium lenses"). Moreover, the transmission decreases, and unwanted scattering and refraction effects at the lens edges can take place.

Fortunately, RXOPTICS offers lenses of a new material, IS50-M. These lenses are available in a thickness of 1 mm. As evidenced in Figure C.1 on the following page, IS50-M has a smaller USAXS intensity than IF-1. Only at $Q > 0.4$ nm^{-1} does the scattering exceed that of IF-1, but here the data is very sensitive to a correct background subtraction. Two other Be grades from Materion were tested, resulting in a scattering that was a factor of 10 to 100 more intense in the relevant q-range (see Figure C.1 on the next page). These Be grades should be avoided for the highest-quality Be optics.

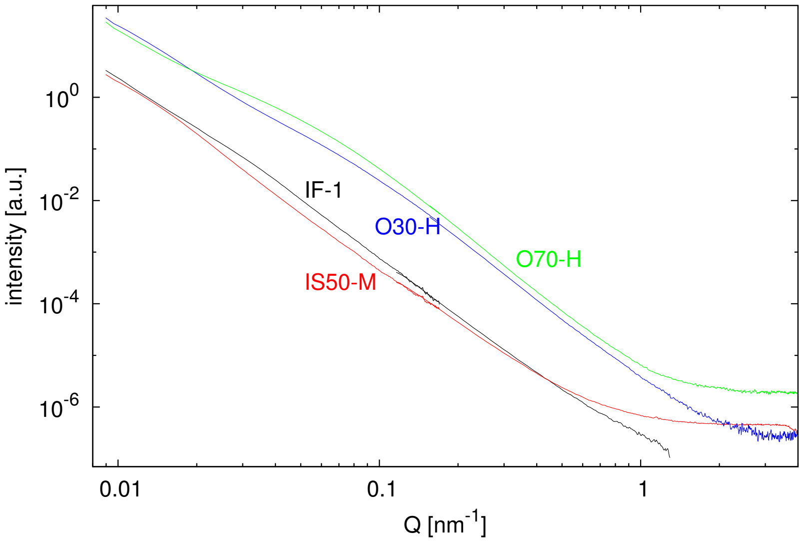

Figure C.1: Comparison of SAXS intensity from different grades of Be sheets

In Figure C.2 on the facing page, the SAXS intensity of the unprocessed IF-1 material is compared to two lenses—of radius R = 4 mm and R = 1.5 mm—of the same Be grade. The SAXS intensity is slightly increased for the lenses. This could be caused by micro- and nano-cracks introduced during the lens manufacturing. However, the changes are small. All SAXS curves are featureless, which makes a determination of sizes of impurity clusters or voids almost impossible. Interface scattering clearly dominates, and the intensity curves scale approximately like q^{-4} over the investigated q-range. In order to gain more insight into the structure of the Be sheets, X-ray laminography [47] measurements have been performed at ID19, ESRF. The data is currently being evaluated.

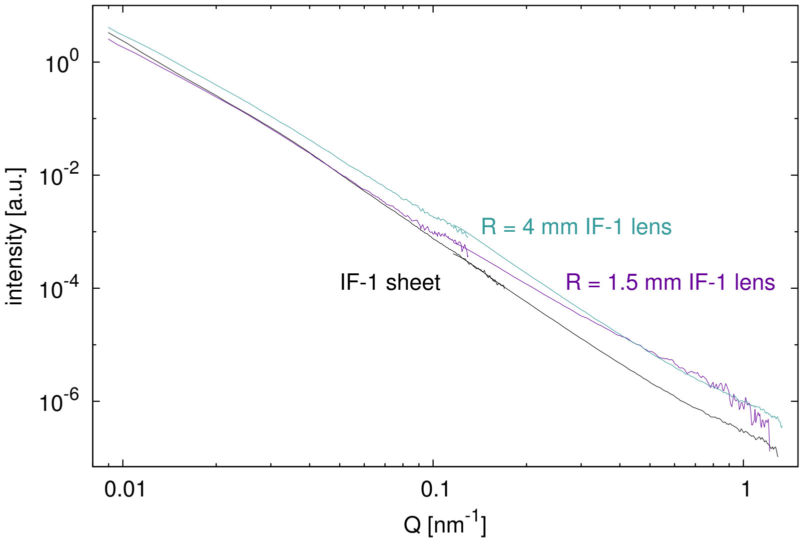

Figure C.2: Comparison of SAXS intensity from CRLs made of high-purity Be (IF-1) and from unprocessed sheets of the same material

All investigated materials were powder-sintered high-purity Be or hot-rolled foils from a Be ingot cast of refined flakes (IF-1). An overview of material grades is found on the Materion website [78]. Recently, physical vapour–deposited Be was also investigated for use as X-ray windows [37; 38]. There is one producer worldwide: NGK Insulators. Used as a window, this type of Be shows superior performance. It is possible that this material could also be used for CRL manufacturing if the thickness can be increased from the currently available maximum of 128 µm.

C.2 Wavefront propagation through Be CRLs

The XFEL beam is almost fully transversely coherent, and hence the propagation of radiation through optical components should be simulated in the framework of wave optics. The calculations shown in the following sections are based on the Fourier optics approach implemented in the Synchrotron Radiation Workshop (SRW) library [22], with further extensions for specific XFEL applications [102].

The aim is to study the *collimation then focusing* case described in (a) in Figure 5.2 on page 75. The wavefront propagation is performed at 6.742 keV. At this energy, ideal collimation at the CRL-1 position can be achieved with one Be lens of radius R = 3.3 mm. The physical aperture of a 1 mm thick lens is $2R_0$ = 3.6 mm, and the vertex thickness is 30 µm.

Ideal focusing of the collimated beam onto the sample is achieved by CRL-2. At 6.742 keV, this can be achieved with eight Be lenses of radius $R = 3.3$ mm.

C.2.1 Impact of Be imperfections

The idea of the simulation was to test the sensitivity to imperfections of the Be material. As a toy model, we chose spherical voids with random centres and a normal distribution of their radii (average radius ~ 5 µm). The volume fraction of voids for the case presented here is about 10^{-4}.

Figure C.3 shows the intensity distribution at several locations after CRL-1 obtained by propagation of the wave field. The simulation takes the SASE properties into account but does not include the effects of other optical components. The collimation ensures that the intensity distribution does not broaden, but the voids create some features in the intensity. However, with further propagation, the oscillations in intensity gradually weaken and die out. The intensity distribution incident on CRL-2 (at 931 m from the source or 696 m from CRL-1) is shown in Figure C.4 on the next page. It is compared to that immediately before CRL-1, 696 m upstream. Even if small distortions to the perfect Gaussian shape are seen, the effect is not dramatic.

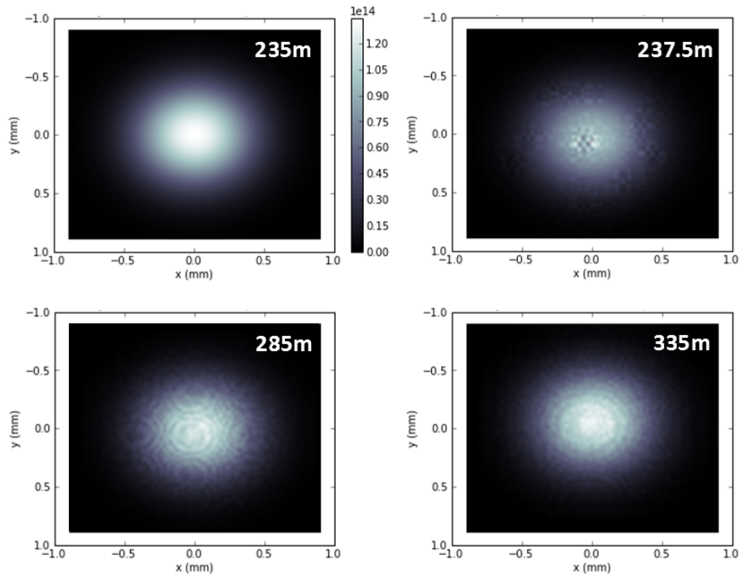

Figure C.3: Intensity in a plane perpendicular to the propagation direction at different locations: 235 m (right before CRL-1), 237.5 m (2.5 m downstream of CRL-1), 285.5 m (50 m downstream), and 335 m (100 m downstream). The effect of the voids in CRL-1 is obvious. Simulation script courtesy of L. Samoylova (European XFEL).

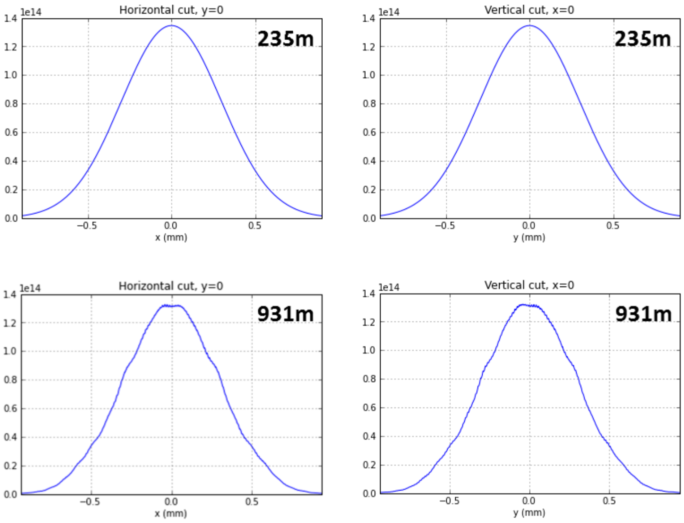

Figure C.4: Intensity distribution with voids in CRL-1. The profiles right upstream of CRL-1 (upper row) are compared to the profiles before CRL-2 (lower row). The distance between the lenses is 696 m.

The beam is propagated through CRL-2 to focus the beam at the sample position. Figure C.5 on the following page nicely illustrates that, at focus, the effect of voids in CRL-1 and CRL-2 is barely visible in the intensity distribution. In particular, no broadening is observed, and the focal size is 10.4 µm, which is close to the result (7.1 µm) of the simplified calculation based on Equation 3.1 on page 23 and Equation 3.2 on page 23. Out of focus, the situation is different but will not be discussed here.

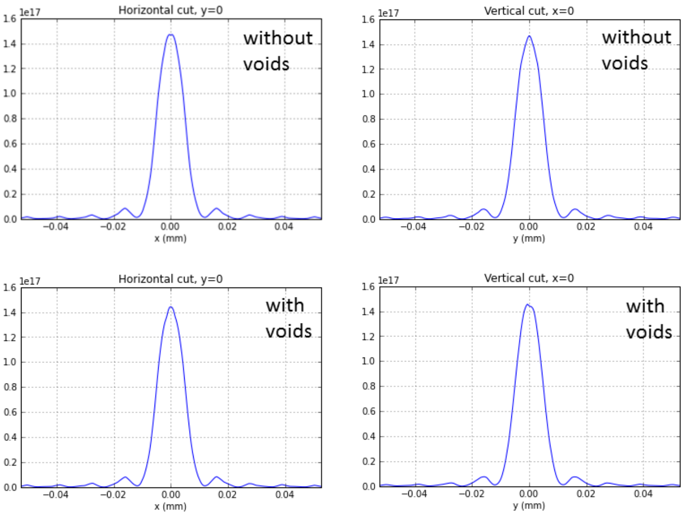

Figure C.5: Horizontal and vertical cuts of the intensity at focus. Both CRL-1 and CRL-2 are required in this *collimation then focusing* scheme. The ideal situation (no voids in CRL-1 and CRL-2) is compared to the model with random voids in all lenses, as described in the text. At focus, no big difference is seen.

Work is in progress to set up simulations of all focusing schemes at different energies, also taking the offset mirrors into account.

C.2.2 Dispersion effects

The dispersion introduced by a typical lens configuration (*collimation then focusing*) is illustrated in Figure C.6. The short delta pulse, with a duration of ~ 0.3 fs, corresponds to the bandwidth of SASE radiation for a photon energy of ~ 7 keV. The pulse propagates through the offset mirrors, the collimating CRL-1 lenses, and the focusing CRL-2 lenses. The broadening is negligible in this case but could become significant in the *intermediate focusing* scheme (see (c) in Figure 5.2 on page 75).

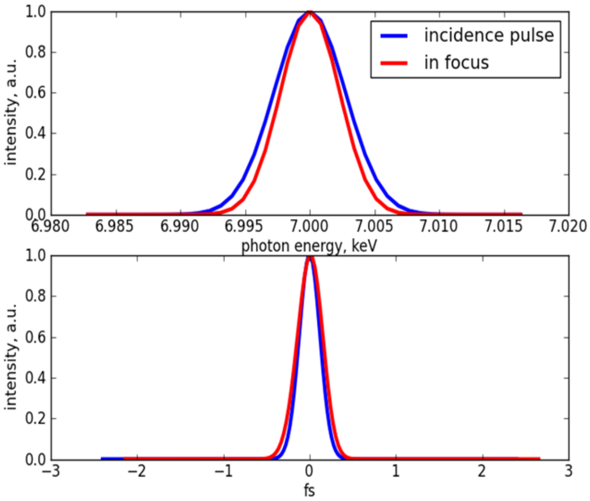

Figure C.6: Dispersion due to the CRL focusing geometry. A slight stretching of the pulse is observed due to the chromatic focusing, but nothing dramatic.

These simulations will continue to validate the CRL focusing scheme proposed for the MID instrument.

D Bibliography

[1] B. Abécassis, F. Testard, O. Spalla, et al.: “Probing in situ the Nucleation and Growth of Gold Nanoparticles by Small-Angle X-ray Scattering”, Nano Letters **7**, 1723 (2007) doi:10.1021/nl0707149

[2] J. Als-Nielsen, D. McMorrow: *Elements of modern X-ray physics* (Wiley 2001)

[3] M. Altarelli, R. Brinkmann, M. Chergui, et al. (eds.): “Technical Design Report: The European X-Ray Free-Electron Laser”, DESY Report 2006-097 (2007) doi:10.3204/DESY_06-097

[4] J. Amann, W. Berg, V. Blank, et al.: “Demonstration of self-seeding in a hard-X-ray free-electron laser”, Nature Photonics **6**, 693 (2012) doi:10.1038/nphoton.2012.180

[5] J. Arthur, et al.: “Linear Coherent Light Source (LCLS) Conceptual Design Report” (2002), p. 554

[6] Y. Asano: *Beamline shielding calculations for Euro-XFEL*, private communication, RIKEN SPring-8 Center, 2013

[7] M. Bargheer, N. Zhavoronkov, Y. Gritsai, et al.: “Coherent Atomic Motions in a Nanostructure Studied by Femtosecond X-ray Diffraction”, Science **306**, 1771 (2004) doi:10.1126/science.1104739

[8] R. Barrett, M. Faucon, J. Lopez, et al.: “X-ray microfocussing combined with microfluidics for on-chip X-ray scattering measurements”, Lab on a Chip **6**, 494 (2006) doi:10.1039/B517055A

[9] W. J. Bartels: “Characterization of thin layers on perfect crystals with a multipurpose high resolution x-ray diffractometer”, Journal of Vacuum Science Technology B: Microelectronics and Nanometer Structures **1**, 338 (1983) doi:10.1116/1.582553

[10] W. J. Bartels, J. Hornstra, D. J. W. Lobeek: “X-ray diffraction of multilayers and superlattices”, Acta Crystallographica Section A: Foundations of Crystallography **42**, 539 (1986) doi:10.1107/S0108767386098768

[11] R. Baruzzo, private communication, Cinel s.r.l., Italy, 2012

[12] E. Beaurepaire, J.-C. Merle, A. Daunois, et al.: “Ultrafast Spin Dynamics in Ferromagnetic Nickel”, Physical Review Letters **76**, 4250 (1996) doi:10.1103/PhysRevLett.76.4250

[13] J. Becker, private communications, DESY, 2013

[14] J. Becker, C. Gutt, H. Graafsma: “Simulation study of the impact of AGIPD design choices on X-ray Photon Correlation Spectroscopy utilizing the intensity autocorrelation technique”, Journal of Instrumentation **6**, P11005 (2011) doi:10.1088/1748-0221/6/11/P11005

[15] J. Becker, D. Greiffenberg, U. Trunk, et al.: “The single photon sensitivity of the Adaptive Gain Integrating Pixel Detector”, Nuclear Instruments and Methods in Physics Research Section A: Accelerators, Spectrometers, Detectors and Associated Equipment **694**, 82–90 (2012) doi:10.1016/j.nima.2012.08.008

[16] W. Becker, X. Liu, P. J. Ho, et al.: “Theories of photoelectron correlation in laser-driven multiple atomic ionization”, Reviews of Modern Physics **84**, 1011–1043 (2012) doi:10.1103/RevModPhys.84.1011

[17] M. Beye, O. Krupin, G. Hays, et al.: “X-ray pulse preserving single-shot optical cross-correlation method for improved experimental temporal resolution”, Applied Physics Letters **100**, 121108.1–121108.4 (2012) doi:10.1063/1.3695164

[18] M. R. Bionta, H. T. Lemke, J. P. Cryan, et al.: “Spectral encoding of x-ray/optical relative delay”, Optics Express **19**, 21855 (2011) doi:10.1364/OE.19.021855

[19] R. C. Burns, A. I. Chumakov, S. H. Connell, et al.: “HPHT growth and x-ray characterization of high-quality type IIa diamond”, Journal of Physics: Condensed Matter **21**, 364224 (2009) doi:10.1088/0953-8984/21/36/364224

[20] A. Charvat, E. Lugovoj, M. Faubel, et al.: “New design for a time-of-flight mass spectrometer with a liquid beam laser desorption ion source for the analysis of biomolecules”, Review of Scientific Instruments **75**, 1209 (2004) doi:10.1063/1.1710704

[21] M. W Chase: *JANAF thermochemical tables* (American Chemical Society; American Institute of Physics for the National Bureau of Standards, Washington, D.C.; New York 1986)

[22] O. Chubar, M.-E. Couprie, M. Labat, et al.: “Time-dependent FEL wavefront propagation calculations: Fourier optics approach”, Nuclear Instruments and Methods in Physics Research Section A: Accelerators, Spectrometers, Detectors and Associated Equipment **593**, 30–34 (2008) doi:10.1016/j.nima.2008.04.058

[23] Y. Chushkin, C. Caronna, A. Madsen: “A novel event correlation scheme for X-ray photon correlation spectroscopy”, Journal of Applied Crystallography **45**, 807 (2012) doi:10.1107/S0021889812023321

[24] H. Cole, N. R. Stemple: “Effect of Crystal Perfection and Polarity on Absorption Edges Seen in Bragg Diffraction”, Journal of Applied Physics **33**, 2227–2233 (1962) doi:10.1063/1.1728933

[25] P. Denes, D. Doering, H. A. Padmore, et al.: “A fast, direct x-ray detection charge-coupled device”, Review of Scientific Instruments **80**, 083302 (2009) doi:10.1063/1.3187222

[26] *Department of Single Crystal Growth, Technological Institute for Superhard and Novel Carbon Materials, Troitsk, Russia*, http://www.ntcstm.troitsk.ru/en/

[27] D. Doering, N. Andresen, D. Contarato, et al.: “A 200 Frames per Second, 1-Megapixel, Frame Store CCD camera for X-ray imaging”, Oral presentation at NSS meeting, Oct./Nov. 2012, Anaheim, CA (2012)

[28] *European XFEL - Documents - Technical Reports & Notes*, https://www.xfel.eu/documents/technical_documents/

[29] A. Fluerasu, A. Moussaïd, P. Falus, et al.: “X-ray photon correlation spectroscopy under flow”, Journal of Synchrotron Radiation **15**, 378 (2008) doi:10.1107/S0909049508006420

[30] W. Freund: *Preliminary results from Diamond Detector tests at ELETTRA*, 2013

[31] D. M. Fritz, D. A. Reis, B. Adams, et al.: “Ultrafast Bond Softening in Bismuth: Mapping a Solid’s Interatomic Potential with X-rays”, Science **315**, 633 (2007) doi:10.1126/science.1135009

[32] G. Geloni, V. Kocharyan, E. Saldin: “A novel self-seeding scheme for hard X-ray FELs”, Journal of Modern Optics **58**, 1391 (2011) doi:10.1080/09500340.2011.586473

[33] A. Giuliani, I. Yao, B. Lagarde, et al.: “A differential pumping system to deliver windowless VUV photons at atmospheric pressure”, Journal of Synchrotron Radiation **18**, 546 (2011) doi:10.1107/S0909049511016517

[34] J. M. Glownia, J. Cryan, J. Andreasson, et al.: “Time-resolved pump-probe experiments at the LCLS”, Optics Express **18**, 17620 (2010) doi:10.1364/OE.18.017620

[35] C. M. Günther, B. Pfau, R. Mitzner, et al.: “Sequential femtosecond X-ray imaging”, Nature Photonics **5**, 99 (2011) doi:10.1038/nphoton.2010.287

[36] T. Gog, D. M. Casa, I. Kuzmenko, et al.: “Windowless transition between atmospheric pressure and high vacuum via differential pumping for synchrotron radiation applications”, Journal of Synchrotron Radiation **14**, 339 (2007) doi:10.1107/S0909049507016317

[37] S. Goto, S. Takahashi, T. Kudo, et al.: “Characterization of beryllium and CVD diamond for synchrotron radiation beamline windows and x-ray beam monitor”, 67050H (2007) doi:10.1117/12.735356

[38] S. Goto, S. Takahashi, Y. Inubushi, et al.: “Characterization of beryllium foils for coherent x-ray applications of synchrotron radiation and XFEL beamlines”, Proceedings SPIE, vol. 8139, 813910 (San Diego 2011) doi:10.1117/12.894506

[39] G. Grübel, A. Madsen, A. Robert: “X-Ray Photon Correlation Spectroscopy (XPCS)”, *Soft Matter Characterization*, ed. by R. Borsali, R. Pecora (Springer Netherlands 2008), p. 953

[40] G. Grübel, G. Stephenson, C. Gutt, et al.: “XPCS at the European X-ray free electron laser facility”, Nuclear Instruments and Methods in Physics Research

Section B: Beam Interactions with Materials and Atoms **262**, 357 (2007) doi:10.1016/j.nimb.2007.05.015

[41] I. Grguraš, A. R. Maier, C. Behrens, et al.: “Ultrafast X-ray pulse characterization at free-electron lasers”, Nature Photonics **6**, 852 (2012) doi:10.1038/nphoton.2012.276

[42] J. Gulden, O. M. Yefanov, E. Weckert, et al.: “Imaging of Nanocrystals with Atomic Resolution Using High-Energy Coherent X-rays”, AIP Conference Proceedings **1365**, 42–45 (2011) doi:10.1063/1.3625300

[43] C. Gutt, P. Wochner, B. Fischer, et al.: “Single Shot Spatial and Temporal Coherence Properties of the SLAC Linac Coherent Light Source in the Hard X-Ray Regime”, Physical Review Letters **108**, 024801 (2012) doi:10.1103/PhysRevLett.108.024801

[44] M. Harmand, R. Coffee, M. R. Bionta, et al.: “Achieving few-femtosecond time-sorting at hard X-ray free-electron lasers”, Nature Photonics **7**, 215–218 (2013) doi:10.1038/nphoton.2013.11

[45] S. P. Hau-Riege, R. A. London, A. Graf, et al.: “Interaction of short x-ray pulses with low-Z x-ray optics materials at the LCLS free-electron laser”, Optics Express **18**, 23933 (2010) doi:10.1364/OE.18.023933

[46] B. Heisen: “Scientific Computing at the European XFEL”, in preparation (2013)

[47] L. Helfen, A. Myagotin, P. Mikulík, et al.: “On the implementation of computed laminography using synchrotron radiation”, Review of Scientific Instruments **82**, 063702 (2011) doi:10.1063/1.3596566

[48] B. Henke, E. Gullikson, J. Davis: “X-Ray Interactions: Photoabsorption, Scattering, Transmission, and Reflection at E = 50–30,000 eV, Z = 1–92”, Atomic Data and Nuclear Data Tables **54**, 181–342 (1993) doi:10.1006/adnd.1993.1013

[49] B. Henrich, J. Becker, R. Dinapoli, et al.: “The adaptive gain integrating pixel detector AGIPD a detector for the European XFEL”, Nuclear Instruments and Methods in Physics Research Section A: Accelerators, Spectrometers, Detectors and Associated Equipment **633, Supplement 1**, S11 (2011) doi:10.1016/j.nima.2010.06.107

[50] M. Hoshino, K. Uesugi, J. Pearson, et al.: “Development of an X-ray real-time stereo imaging technique using synchrotron radiation”, Journal of Synchrotron Radiation **18**, 569 (2011) doi:10.1107/S0909049511017547

[51] S. Hosokawa: “Inelastic X-ray scattering experiments at extreme conditions: high temperatures and high pressures”, Condensed Matter Physics **11**, 71 (2008) doi:10.5488/CMP.11.1.71

[52] H. Hosseinkhannazer, private communications, Norcada Inc., Edmonton, Canada

[53] S. O. Hruszkewycz, M. Sutton, P. H. Fuoss, et al.: “High Contrast X-ray Speckle from Atomic-Scale Order in Liquids and Glasses”, Physical Review Letters **109**, 185502 (2012) doi:10.1103/PhysRevLett.109.185502

[54] Y. Inubushi, K. Tono, T. Togashi, et al.: “Determination of the Pulse Duration of an X-Ray Free Electron Laser Using Highly Resolved Single-Shot Spectra”, Physical Review Letters **109**, 144801 (2012) doi:10.1103/PhysRevLett.109.144801

[55] Z. Islam, J. P. C. Ruff, H. Nojiri, et al.: “A portable high-field pulsed-magnet system for single-crystal x-ray scattering studies”, Review of Scientific Instruments **80**, 113902 (2009) doi:10.1063/1.3251273

[56] S. Joksch, W. Graeff, J. B. Hastings, et al.: “Performance of an x-ray optical time delay line with synchrotron radiation”, Review of Scientific Instruments **63**, 1114 (1992) doi:10.1063/1.1143110

[57] Z. Kam: “Determination of Macromolecular Structure in Solution by Spatial Correlation of Scattering Fluctuations”, Macromolecules **10**, 927 (1977) doi:10.1021/ma60059a009

[58] *Karabo wiki*, https://docs.xfel.eu/share/page/site/KaraboFramework/dashboard

[59] P. Karvinen, S. Rutishauser, A. Mozzanica, et al.: “Single-shot analysis of hard x-ray laser radiation using a noninvasive grating spectrometer”, Optics Letters **37**, 5073 (2012) doi:10.1364/OL.37.005073

[60] M. Kato, T. Tanaka, T. Kurosawa, et al.: “Pulse energy measurement at the hard x-ray laser in Japan”, Applied Physics Letters **101**, 023503.1–023503.4 (2012) doi:10.1063/1.4733354

[61] K. F. Kelton, G. W. Lee, A. K. Gangopadhyay, et al.: “First X-Ray Scattering Studies on Electrostatically Levitated Metallic Liquids: Demonstrated Influence of Local Icosahedral Order on the Nucleation Barrier”, Physical Review Letters **90**, 195504 (2003) doi:10.1103/PhysRevLett.90.195504

[62] V. G. Kohn, O. Y. Gorobtsov, I. A. Vartanyants: “Spectrometer for hard X-ray free-electron laser based on diffraction focusing”, Journal of Synchrotron Radiation **20**, 258 (2013) doi:10.1107/S0909049513000903

[63] C. v. Korff Schmising, M. Bargheer, M. Kiel, et al.: “Coupled Ultrafast Lattice and Polarization Dynamics in Ferroelectric Nanolayers”, Physical Review Letters **98**, 257601 (2007) doi:10.1103/PhysRevLett.98.257601

[64] T. Kudo, K. Tono, M. Yabashi, et al.: “A photodiode amplifier system for pulse-by-pulse intensity measurement of an x-ray free electron laser”, Review of Scientific Instruments **83**, 043108.1–043108.6 (2012) doi:10.1063/1.3701713

[65] R. P. Kurta, M. Altarelli, E. Weckert, et al.: “X-ray cross-correlation analysis applied to disordered two-dimensional systems”, Physical Review B **85**, 184204 (2012) doi:10.1103/PhysRevB.85.184204

[66] R. P. Kurta, R. Dronyak, M. Altarelli, et al.: “Solution of the phase problem for coherent scattering from a disordered system of identical particles”, New Journal of Physics **15**, 013059 (2013) doi:10.1088/1367-2630/15/1/013059

[67] E. Lassner, W.-D. Schubert: *Tungsten: Properties, Chemistry, Technology of the Element, Alloys, and Chemical Compounds* (Springer 1999)

[68] S. Lee, W. Roseker, C. Gutt, et al.: “High wavevector temporal speckle correlations at the Linac Coherent Light Source”, Optics Express **20**, 9790 (2012) doi:10.1364/OE.20.009790

[69] B. Lengeler, C. Schroer, J. Tümmler, et al.: “Imaging by parabolic refractive lenses in the hard X-ray range”, Journal of Synchrotron Radiation **6**, 1153 (1999) doi:10.1107/S0909049599009747

[70] P. J. E. M. van der Linden: *High-temperature X-ray in situ furnaces*, 2013, http://www.esrf.eu/Industry/documentation/F7_Furnace.pdf

[71] P. J. E. M. van der Linden, O. Mathon, C. Strohm, et al.: “Miniature pulsed magnet system for synchrotron x-ray measurements”, Review of Scientific Instruments **79**, 075104.1–075104.8 (2008) doi:10.1063/1.2949873

[72] P. J. E. M. van der Linden, C. Strohm, T. Roth, et al.: “The ESRF Miniature Pulsed Magnetic Field System”, AIP Conference Proceedings **1234**, 107 (2010) doi:10.1063/1.3463153

[73] L. Lomb, J. Steinbrener, S. Bari, et al.: “An anti-settling sample delivery instrument for serial femtosecond crystallography”, Journal of Applied Crystallography **45**, 674 (2012) doi:10.1107/S0021889812024557

[74] O. M. Lugovskaya, S. A. Stepanov: “Calculation of the polarizabilities of crystals for diffraction of x-ray on the continuous spectrum at wavelengths of 0.1-10 Å ”, Soviet physics. Crystallography **36**, 478–481 (1991)

[75] A. Madsen: “Conceptual Design Report: Scientific Instrument MID” (2012) doi:10.3204/XFEL.EU/TR-2011-008

[76] A. Madsen, R. L. Leheny, H. Guo, et al.: “Beyond simple exponential correlation functions and equilibrium dynamics in x-ray photon correlation spectroscopy”, New Journal of Physics **12**, 055001 (2010) doi:10.1088/1367-2630/12/5/055001

[77] C. Mammen, private communication, JJ X-Ray, 2012

[78] *Materion Brush Beryllium & Composites, “Designing and Fabricating Beryllium”*, http://materion.com/ResourceCenter/ProductData/Beryllium/BerylliumMetal/DesignGuides.aspx

[79] N. A. Mauro, K. F. Kelton: “A highly modular beamline electrostatic levitation facility, optimized for in situ high-energy x-ray scattering studies of equilibrium and supercooled liquids”, Review of Scientific Instruments **82**, 035114 (2011) doi:10.1063/1.3554437

[80] R. Mitzner, B. Siemer, M. Neeb, et al.: “Spatio-temporal coherence of free electron laser pulses in the soft x-ray regime”, Optics Express **16**, 19909 (2008) doi:10.1364/OE.16.019909

[81] R. Mitzner, M. Neeb, T. Noll, et al.: “An x-ray autocorrelator and delay line for the VUV-FEL at TTF/DESY”, Proceedings SPIE **5920**, 86 (2005) doi:10.1117/12.617304

[82] M. F. Moody, P. Vachette, A. M. Foote, et al.: “Stopped-flow x-ray scattering: the dissociation of aspartate transcarbamylase.”, Proceedings of the National Academy of Sciences of the United States of America **77**, 4040 (1980)

[83] J. Morse, private communication, ESRF and LCLS (sabbatical), 2012

[84] A. Mozzanica, A Bergamaschi, R Dinapoli, et al.: “The GOTTHARD charge integrating readout detector: design and characterization”, Journal of Instrumentation **7**, C01019 (2012) doi:10.1088/1748-0221/7/01/C01019

[85] M. Nakatsutsumi, private communications, European XFEL, 2013

[86] M. C. Newton, S. J. Leake, R. Harder, et al.: “Three-dimensional imaging of strain in a single ZnO nanorod”, Nature Materials **9**, 120 (2010) doi:10.1038/nmat2607

[87] T. Osaka, M. Yabashi, Y. Sano, et al.: “A Bragg beam splitter for hard x-ray free-electron lasers”, Optics Express **21**, 2823 (2013) doi:10.1364/OE.21.002823

[88] T. Osaka, M. Yabashi, Y. Sano, et al.: “Fabrication of Ultrathin Bragg Beam Splitter by Plasma Chemical Vaporization Machining”, Emerging Technology in Precision Engineering XIV **223-224**, 40 (2012)

[89] C. Ozkan, private communication, European XFEL, 2013

[90] P. Panine, S. Finet, T. Weiss, et al.: “Probing fast kinetics in complex fluids by combined rapid mixing and small-angle X-ray scattering”, Advances in Colloid and Interface Science **127**, 9 (2006) doi:10.1016/j.cis.2006.06.003

[91] L. Pollack, M. W. Tate, A. C. Finnefrock, et al.: “Time Resolved Collapse of a Folding Protein Observed with Small Angle X-Ray Scattering”, Physical Review Letters **86**, 4962 (2001) doi:10.1103/PhysRevLett.86.4962

[92] M. Pomorski, M. Ciobanu, C. Mer, et al.: “Position-sensitive radiation detectors made of single crystal CVD diamond”, physica status solidi (a) **206**, 2109 (2009) doi:10.1002/pssa.200982229

[93] I. Rajkovic, J. Hallmann, S. Grübel, et al.: “Development of a multipurpose vacuum chamber for serial optical and diffraction experiments with free electron laser radiation”, Review of Scientific Instruments **81**, 045105 (2010) doi:10.1063/1.3327816

[94] M. Renninger: “Diffraction patterns of thin perfect crystals and their applicability to the determination of structure factors”, Acta Crystallographica Section A: Crystal Physics, Diffraction, Theoretical and General Crystallography **31**, 42 (1975) doi:10.1107/S0567739475000071

[95] M. Sanchez del Rio, R. J. Dejus: "Status of XOP: an x-ray optics software toolkit", vol. 5536, 171 (SPIE 2004) doi:10.1117/12.560903

[96] S. Roling, L. Samoylova, B. Siemer, et al.: "Design of an x-ray split- and delay-unit for the European XFEL", Proceedings SPIE, 850407 (2012) doi:10.1117/12.965547

[97] W. Roseker, private communications, DESY, 2012

[98] W. Roseker, H. Franz, H. Schulte-Schrepping, et al.: "Development of a hard X-ray delay line for X-ray photon correlation spectroscopy and jitter-free pump–probe experiments at X-ray free-electron laser sources", Journal of Synchrotron Radiation **18**, 481 (2011) doi:10.1107/S0909049511004511

[99] W. Roseker, H. Franz, H. Schulte-Schrepping, et al.: "Performance of a picosecond x-ray delay line unit at 8.39 keV", Optics Letters **34**, 1768 (2009) doi:10.1364/OL.34.001768

[100] A. Rousse, C. Rischel, S. Fourmaux, et al.: "Non-thermal melting in semiconductors measured at femtosecond resolution", Nature **410**, 65 (2001) doi:10.1038/35065045

[101] *RXOPTICS*,
http://www.rxoptics.de

[102] L. Samoylova, A. Buzmakov, G. Geloni, et al.: "Cross-platform wave optics software for XFEL applications", Advances in Computational Methods for X-Ray Optics II, San Diego, California, September 23, 2011, Proc. of SPIE 8141, 81410A (2011) doi:10.1117/12.893044

[103] M. L. Schlossman: "Liquid–liquid interfaces: studied by X-ray and neutron scattering", Current Opinion in Colloid & Interface Science **7**, 235 (2002) doi:10.1016/S1359-0294(02)00053-5

[104] K. E. Schmidt, J. C. H. Spence, U. Weierstall, et al.: "Tomographic Femtosecond X-Ray Diffractive Imaging", Physical Review Letters **101**, 115507 (2008) doi:10.1103/PhysRevLett.101.115507

[105] E. A. Schneidmiller, M. V. Yurkov: "Harmonic lasing in x-ray free electron lasers", Physical Review Special Topics - Accelerators and Beams **15**, 080702 (2012) doi:10.1103/PhysRevSTAB.15.080702

[106] T. Seydel, A. Madsen, M. Sprung, et al.: "Setup for in situ surface investigations of the liquid/glass transition with (coherent) x rays", Review of Scientific Instruments **74**, 4033 (2003) doi:10.1063/1.1599068

[107] Y. Shvyd'ko, S. Stoupin, V. Blank, et al.: "Near-100% Bragg reflectivity of X-rays", Nature Photonics **5**, 539 (2011) doi:10.1038/nphoton.2011.197

[108] H. Sinn, private communication, European XFEL, 2013

[109] H. Sinn, J. Gaudin, L. Samoylova, et al.: "Conceptual Design Report: X-Ray Optics and Beam Transport", XFEL.EU TR-2011-002 (2011) doi:10.3204/XFEL.EU/TR-2011-002

[110] H. Sinn, M. Dommach, X. Dong, et al.: “Technical Design Report: X-Ray Optics and Beam Transport”, XFEL.EU TR-2012-006 (2012) doi:10.3204/XFEL.EU/TR-2012-006

[111] L. B. Skinner, C. J. Benmore, B. Shyam, et al.: “Structure of the floating water bridge and water in an electric field”, Proceedings of the National Academy of Sciences **109**, 16463 (2012) doi:10.1073/pnas.1210732109

[112] A. Snigirev, V. Kohn, I. Snigireva, et al.: “A compound refractive lens for focusing high-energy X-rays”, Nature **384**, 49 (1996) doi:10.1038/384049a0

[113] F. Sorgenfrei, W. F. Schlotter, T. Beeck, et al.: “The extreme ultraviolet split and femtosecond delay unit at the plane grating monochromator beamline PG2 at FLASH”, Review of Scientific Instruments **81**, 043107 (2010) doi:10.1063/1.3374166

[114] R. Steinmann, Y. Chushkin, C. Caronna, et al.: “A small-angle scattering chamber for x-ray photon correlation spectroscopy at low temperatures”, Review of Scientific Instruments **82**, 025109 (2011) doi:10.1063/1.3553012

[115] S. A. Stepanov: *χ_{oh} on the web!!!*, 2012, http://sergey.gmca.aps.anl.gov/x0h.html

[116] J. Stingl, F. Zamponi, B. Freyer, et al.: “Electron Transfer in a Virtual Quantum State of $LiBH_4$ Induced by Strong Optical Fields and Mapped by Femtosecond X-Ray Diffraction”, Physical Review Letters **109**, 147402 (2012) doi:10.1103/PhysRevLett.109.147402

[117] S. Stoupin, V. Blank, S. Terentyev, et al.: “Diamond crystal optics for self-seeding of hard X-rays in X-ray free-electron lasers”, Diamond and Related Materials **33**, 1 (2013) doi:10.1016/j.diamond.2012.12.009

[118] Y. Tamenori: “Development of a differential pumping system for soft X-ray beamlines for windowless experiments under normal atmospheric conditions”, Journal of Synchrotron Radiation **17**, 243 (2010) doi:10.1107/S0909049509052571

[119] K. Tamura, M. Inui, S. Hosokawa: “Energy-dispersive x-ray diffraction equipment for fluids at extreme conditions of high temperatures and high pressures”, Review of Scientific Instruments **70**, 144 (1999) doi:10.1063/1.1149556

[120] F. Tavella, N. Stojanovic, G. Geloni, et al.: “Few-femtosecond timing at fourth-generation X-ray light sources”, Nature Photonics **5**, 162 (2011) doi:10.1038/nphoton.2010.311

[121] R. Teworte, U. Bonse: “High-precision determination of structure factors F_h of silicon”, Physical Review B **29**, 2102–2108 (1984) doi:10.1103/PhysRevB.29.2102

[122] *The Center for X-Ray Optics, “X-Ray Interactions With Matter”*, web interface for X-ray calculations based on [48], http://henke.lbl.gov/optical_constants/

[123] P. Thibault, M. Dierolf, O. Bunk, et al.: “Probe retrieval in ptychographic coherent diffractive imaging”, Ultramicroscopy **109**, 338 (2009) doi:10.1016/j.ultramic.2008.12.011

[124] K. Tiedtke, private communication, DESY, 2013

[125] K. Tiedtke, J. Feldhaus, U. Hahn, et al.: “Gas detectors for x-ray lasers”, Journal of Applied Physics **103**, 094511 (2008) doi:10.1063/1.2913328

[126] K. Tono: *Photon Beam Diagnostics for X-rays, VUV, XFEL - Applications to SASE XFEL*, 2012, http://epaper.kek.jp/BIW2012/talks/tubp01_talk.pdf

[127] K. Tono, T. Kudo, M. Yabashi, et al.: “Single-shot beam-position monitor for x-ray free electron laser”, Review of Scientific Instruments **82**, 023108.1–023108.6 (2011) doi:10.1063/1.3549133

[128] Y. S. Touloukian: *Thermophysical properties of high temperature solid materials.* (Macmillan, New York 1967)

[129] J. Ullrich, A. Rudenko, R. Moshammer: “Free-Electron Lasers: New Avenues in Molecular Physics and Photochemistry”, Annual Review of Physical Chemistry **63**, 635 (2012) doi:10.1146/annurev-physchem-032511-143720

[130] I. A. Vartanyants, A. Singer, A. P. Mancuso, et al.: “Coherence Properties of Individual Femtosecond Pulses of an X-Ray Free-Electron Laser”, Physical Review Letters **107**, 144801 (2011) doi:10.1103/PhysRevLett.107.144801

[131] B. E. Warren: *X-Ray Diffraction* (Courier Dover Publications 1990)

[132] U. Weierstall, J. C. H. Spence, R. B. Doak: “Injector for scattering measurements on fully solvated biospecies”, Review of Scientific Instruments **83**, 035108 (2012) doi:10.1063/1.3693040

[133] P. Wochner, C. Gutt, T. Autenrieth, et al.: “X-ray cross correlation analysis uncovers hidden local symmetries in disordered matter”, Proceedings of the National Academy of Sciences **106**, 11511 (2009) doi:10.1073/pnas.0905337106

[134] C. Wood, D. Emin, P. E. Gray: “Thermal conductivity behavior of boron carbides”, Physical Review B **31**, 6811 (1985) doi:10.1103/PhysRevB.31.6811

[135] M. Yabashi: *Beamlines for Compact XFELs*, 2010, http://www.sinap.ac.cn/compactxfel10/Yabashi.pdf

[136] M. Yabashi, J. B. Hastings, M. S. Zolotorev, et al.: “Single-Shot Spectrometry for X-Ray Free-Electron Lasers”, Physical Review Letters **97**, 084802 (2006) doi:10.1103/PhysRevLett.97.084802

[137] F. Zamponi, P. Rothhardt, J. Stingl, et al.: “Ultrafast large-amplitude relocation of electronic charge in ionic crystals”, Proceedings of the National Academy of Sciences **109**, 5207 (2012) doi:10.1073/pnas.1108206109

[138] X. Zhang, K. A. Smith, D. R. Worsnop, et al.: “Numerical Characterization of Particle Beam Collimation: Part II Integrated

Aerodynamic-Lens–Nozzle System", Aerosol Science and Technology **38**, 619 (2004) doi:10.1080/02786820490479833

[139] D. Zhu, M. Cammarata, J. M. Feldkamp, et al.: "A single-shot transmissive spectrometer for hard x-ray free electron lasers", Applied Physics Letters **101**, 034103 (2012) doi:10.1063/1.4736725